

Combined Photo- and Thermionic Electron Emission from
Low Work Function Diamond Films

by

Tianyin Sun

A Dissertation Presented in Partial Fulfillment
of the Requirements for the Degree
Doctor of Philosophy

Approved November 2013 by the
Graduate Supervisory Committee:

Robert Nemanich, Chair
Fernando Ponce
Xihong Peng
John Spence
Michael Treacy

ARIZONA STATE UNIVERSITY

December 2013

ABSTRACT

In this dissertation, combined photo-induced and thermionic electron emission from low work function diamond films is studied through low energy electron spectroscopy analysis and other associated techniques. Nitrogen-doped, hydrogen-terminated diamond films prepared by the microwave plasma chemical vapor deposition method have been the most focused material. The theme of this research is represented by four interrelated issues. (1) An in-depth study describes combined photo-induced and thermionic emission from nitrogen-doped diamond films on molybdenum substrates, which were illuminated with visible light photons, and the electron emission spectra were recorded as a function of temperature. The diamond films displayed significant emissivity with a low work function of ~ 1.5 eV. The results indicate that these diamond emitters can be applied in combined solar and thermal energy conversion. (2) The nitrogen-doped diamond was further investigated to understand the physical mechanism and material-related properties that enable the combined electron emission. Through analysis of the spectroscopy, optical absorbance and photoelectron microscopy results from sample sets prepared with different configurations, it was deduced that the photo-induced electron generation involves both the ultra-nanocrystalline diamond and the interface between the diamond film and metal substrate. (3) Based on results from the first two studies, possible photon-enhanced thermionic emission was examined from nitrogen-doped diamond films deposited on silicon substrates, which could provide the basis for a novel approach for concentrated solar energy conversion. A significant increase of emission intensity was observed at elevated temperatures, which was analyzed using computer-based modeling and a combination of different emission mechanisms. (4) In addition, the electronic

structure of vanadium-oxide-terminated diamond surfaces was studied through in-situ photoemission spectroscopy. Thin layers of vanadium were deposited on oxygen-terminated diamond surfaces which led to oxide formation. After thermal annealing, a negative electron affinity was found on boron-doped diamond, while a positive electron affinity was found on nitrogen-doped diamond. A model based on the barrier at the diamond-oxide interface was employed to analyze the results. Based on results of this dissertation, applications of diamond-based energy conversion devices for combined solar- and thermal energy conversion are proposed.

DEDICATION

This dissertation is dedicated to my family.

ACKNOWLEDGMENTS

I would like to first express my gratitude towards my advisor, Dr. Robert J. Nemanich, for allowing me to work in his lab, and for his guidance and encouragement during my Ph.D. study at ASU. Finishing this up would not be possible without his continuous enthusiasm and invaluable knowledge about physics and material science. I still remember what he told me the first time we met: "Learn a little every day, and by the end you'll learn a lot." I have been and will keep on practicing this instruction.

I gratefully appreciate the assistance towards my degree from all the faculty members who have served as my committee: Dr. Fernando A. Ponce, Dr. Xihong Peng, Dr. John Spence and Dr. Michael M.J. Treacy.

This research has been financially supported through the Office of Naval Research, under Grant # N00014-10-1-0540.

I have been extraordinarily lucky to be working with an amazing group of people in the NanoScience Lab, to whom I owe my appreciation. I would to say a special thank you to Franz A.M. Koeck and Dr. Gary G. Hembree, for preparing the diamond samples, teaching me the knowledge about vacuum systems, plus helping me with equipment maintenance and paper writing. Several members: Dr. Joshua R. Smith, Joseph Shammass, Jesse Stryker and Matthew D. Brown, have made significant contributions to studies related to this thesis. I am glad to extend the acknowledgment to other current and past members of the group, with whom I have cherished the teamwork and friendship: Dr. Yang Sun, Dr. Anna Zaniewski, Dr. Fu Tang, Dr. Chiyu Zhu, Dr. Xin Liu, Manpuneet Kaur, Sandeep Gill, Brianna S. Eller, Jialing Yang, Chris England, Xingye Wang, Aaron

Papagalos, Sarah Rupprecht, Megan Householder, Yuchen Du, Troy Daniel, and Glen Redman.

It has been my pleasure to work with Aram Rezikyan who provides his expertise of TEM imaging. I have also had the honor to collaborate with some visiting students from European universities and institutes: Nils Neugebohrn, Petr Borisovich Stepanov, Wiebke Janssen and Muhammad Zamir Othman. It has been a really enjoyable experience not only to work together with them, but also to learn about various cultures.

I would also like to thank the people working for the Department of Physics and the LeRoy Eyring Center for Solid State Science, who have always been helpful and supportive: Araceli Vizcarra, Ixchell Paape, Jane Laux, Ebony Shalley, Rose Murrietta, Diana Convey and Dr. Karl Weiss.

Last, but certainly not the least, I would like thank my parents, my other family members, and friends whose names I have not listed above, for their love and support I have received throughout the years.

TABLE OF CONTENTS

| | Page |
|---|------|
| LIST OF TABLES | vi |
| LIST OF FIGURES | vii |
| CHAPTER | |
| 1 INTRODUCTION | 1 |
| 1.1 Negative electron affinity and <i>n</i> -type doping of diamond | 1 |
| 1.2 Thermionic electron emission and thermionic energy conversion | 4 |
| 1.3 Photo-induced electron emission of diamond | 9 |
| 1.4 Photon-enhanced thermionic emission | 11 |
| 1.5 Thesis approach | 15 |
| References | 17 |
| 2 INSTRUMENTS AND ANALYSIS METHOD | 24 |
| 2.1 Introduction | 24 |
| 2.2 Principle of Photoemission Electron Spectroscopy | 26 |
| 2.3 Hemispherical Electron Analyzer | 30 |
| 2.4 X-ray Photoelectron Spectroscopy | 32 |
| 2.5 Ultraviolet Photoelectron Spectroscopy | 32 |
| 2.6 Calibration of XPS and UPS | 34 |
| 2.7 Xenon Arc Lamp | 37 |
| References | 40 |

| | | |
|---|---|----|
| 3 | COMBINED VISIBLE LIGHT PHOTO-EMISSION AND LOW TEMPERATURE THERMIONIC EMISSION FROM NITROGEN DOPED DIAMOND FILMS | 41 |
| | 3.1 Abstract | 41 |
| | 3.2 Introduction | 41 |
| | 3.3 Experiment | 42 |
| | 3.4 Results | 43 |
| | 3.5 Discussion | 47 |
| | 3.6 Conclusion..... | 50 |
| | References | 51 |
| 4 | INTERFACE AND INTERLAYER BARRIERS EFFECTS ON PHOTO-INDUCED ELECTRON EMISSION FROM LOW WORK FUNCTION DIAMOND FILMS | 55 |
| | 4.1 Abstract | 55 |
| | 4.2 Introduction | 56 |
| | 4.3 Experiment | 57 |
| | 4.4 Results | 60 |
| | 4.5 Discussion | 66 |
| | 4.6 Conclusion..... | 70 |
| | References | 71 |
| 5 | PHOTO INDUCED ELECTRON EMISSION FROM NITROGEN DOPED DIAMOND FILMS ON SILICON SUBSTRATES | 73 |
| | 5.1 Abstract | 73 |

| | | |
|-------|---|-----|
| 5.2 | Introduction | 73 |
| 5.3 | Experiment | 76 |
| 5.4 | Theoretical Background..... | 78 |
| 5.5 | Results | 82 |
| 5.6 | Discussion | 87 |
| 5.7 | Conclusion..... | 89 |
| | References | 90 |
| 6 | ELECTRON AFFINITY OF DOPED DIAMOND SURFACES WITH VANADIUM- OXIDE-TERMINATION | 92 |
| 6.1 | Abstract | 93 |
| 6.2 | Introduction | 94 |
| 6.3 | Experiment | 95 |
| 6.4 | Results | 97 |
| 6.4.1 | O-termination through O-plasma treatment..... | 97 |
| 6.4.2 | Boron-doped diamond (BDD)..... | 99 |
| 6.4.3 | Nitrogen-doped diamond..... | 102 |
| 6.5 | Discussion | 103 |
| 6.6 | Conclusion..... | 107 |
| | References | 107 |
| 7 | SUMMARY & FUTURE WORK | 110 |
| 7.1 | Summary | 110 |
| 7.2 | Future work | 111 |
| 7.2.1 | Photoemission from phosphorus-doped diamond films | 111 |

| | |
|--|-----|
| 7.2.2 Diamond-based isothermal PETE converter..... | 112 |
| 7.2.3 Electronic structure of adsorbed molecules on diamond..... | 113 |
| 7.2.4 Space-charge limitation of diamond photocathodes..... | 114 |
| 7.2.5 Photoelectrochemistry with <i>n</i> -type diamond electrodes..... | 115 |
| References | 116 |
| REFERENCES..... | 118 |
| APPENDIX | |
| A SPATIAL CORRELATION OF PHOTO-INDUCED AND THERMIONIC ELECTRON EMISSION FROM LOW WORK FUNCTION DIAMOND FILMS | 123 |
| B COPYRIGHT STATEMENTS | 139 |

LIST OF TABLES

| Table | Page |
|--|------|
| 1.1 Work function and Richardson constant of some common materials for thermionic applications [27]. | 5 |
| 6.1 C 1s, O 1s, V 2p _{3/2} core levels and effective work function (Φ_w) for vanadium-oxide-terminated BDD samples. | 101 |
| 6.2 C 1s, O 1s, V 2p _{3/2} core levels and effective work function (Φ_w) for vanadium-oxide-terminated NDD samples. | 103 |

LIST OF FIGURES

| Figure | Page |
|--------|--|
| 1.1 | Band schematic of doped diamond, showing the energy levels of the different dopants, and vacuum levels with hydrogen or oxygen termination. 3 |
| 1.2 | (a) Configuration and (b) band schematic of a thermionic energy converter. Electrons flow from the hot emitter to the cold collector, and produce an output electric power. 7 |
| 1.3 | (a) Band schematic and (b) device illustration of a photon-enhanced thermionic energy converter [75]. An enhanced electron population in the emitter is created through photon illumination, and the thermionic emission current towards the collector is significantly increased. 12 |
| 1.4 | Schematic of an isothermal-PETE energy conversion device [82]. Light illumination is provided from the top and converted into enhanced emission from the side emitter. The device is maintained at the same temperature, while excess heat flow is transferred to a thermal engine. 14 |
| 2.1 | Actual view and schematic illustration of the transfer line with integrated UHV systems. 25 |
| 2.2 | Diagrams illustrating the three-step model of photoemission. Electrons are excited from filled states into empty, conduction band states. Some electrons are affected by inelastic collisions as they propagate to the surface, which adds a secondary electron background to the distribution. Electrons with sufficient energy to overcome the work function of the surface are emitted in |

| | | |
|------|---|----|
| | the third step. The distribution of excited electrons reflects features of the density of states. | 27 |
| 2.3 | The “universal curve” of electron mean free path of various metals as a function of kinetic energy [2]. | 28 |
| 2.4 | Schematic of the hemispherical electron analyzer in the UPS system. | 31 |
| 2.5 | Actual views of the discharge lamp when (a) He I and (b) He II lines are tuned for spectroscopy measurements. | 33 |
| 2.6 | Schematic of the UPS chamber, showing relative positions of the sample stage with heater, the light sources and the electron analyzer. | 34 |
| 2.7 | XPS scan of a standard Au foil, showing the 4f peaks that are used for XPS calibration. | 36 |
| 2.8 | UPS scan of a thin Au film deposited by e-beam evaporation, with the characteristic peaks of Au in the valence band. The high energy cut-off at 22.8 eV kinetic energy is referred to E_F for UPS calibration. | 37 |
| 2.9 | Output power of the xenon arc lamp system with associated filters, measured by an optical power meter. | 39 |
| 2.10 | Photoelectron spectra of a Dy film under illumination from the Xe arc lamp with different bandpass filters. Signals can be observed with illuminating wavelength up to 500 nm. | 40 |
| 3.1 | Recorded emission spectra from N-doped diamond showing intensity normalized ambient temperature photoemission. | 44 |
| 3.2 | The total emission, thermionic emission, and subtracted photoemission component from a diamond sample at 270 °C and 340nm illumination. | 45 |

| | | |
|-----|---|----|
| 3.3 | The effect of temperature on thermionic and photo- emission. At low T the emission is dominated by the photo-excited carriers; at high T it is dominated by thermionic excitation. | 46 |
| 3.4 | Combined photo- and thermionic emission spectra from P-doped diamond at 385 °C. | 47 |
| 3.5 | The quantum efficiency of visible light photoemission from a nitrogen-doped diamond film, in comparison to some conventional metal photocathodes [15]. | 48 |
| 3.6 | Band schematics of the diamond emitter (including metal substrate, UNCD interface layer, and N-doped diamond) showing (a) thermionic and (b) photoemission processes. Green dash lines represent the inter-bandgap states inside UNCD layer, introduced by sp^2 bonds. | 49 |
| 3.7 | Experimental and modeled emission spectra of the N-doped diamond film structure showing ambient temperature photoemission with 340nm illumination. | 51 |
| 3.8 | Schematic of a diamond based energy converter. The emitter (doped diamond film) is heated for thermionic emission, and illuminating photons generate photoemission. | 52 |
| 4.1 | Optical absorbance of the diamond structures, obtained through UV-Vis spectroscopy measurements. The samples are diamond films deposited on polished transparent quartz substrates, one with only the (N)UNCD layer and the other has a top N-diamond layer in addition. | 60 |

| | | |
|-----|---|----|
| 4.2 | Combined photo-induced and thermionic emission spectra from N-doped diamond films at elevated temperatures, showing the photon energy dependence. The results are shown under the sample sequence of: (a) D1; (b) D2; (c) D3; (d) D4. | 62 |
| 4.3 | The total emission, thermionic emission, and subtracted photo induced emission spectra components from the diamond samples. Samples are listed in the same sequence as Fig. 4.2. | 63 |
| 4.4 | Photo-induced emission spectra of samples D2 and D4 under illumination of the same wavelength, showing comparison between lower (no observable TE) and higher (significant TE observed) temperatures. In both cases the TE is subtracted from the 400 or 430 °C spectra. | 65 |
| 4.5 | PEEM images of (a) combined emission (“light on”), (b) thermionic emission (“light off”) and (c) subtracted photo-induced emission from the sample with polished Mo substrate / nanodiamond / N-diamond structure (configuration D4). | 66 |
| 4.6 | Band schematics of the diamond emitter. Photoelectrons are presumed to be generated in the UNCD layer or near the metal-diamond interface. Dash lines represent the inter-bandgap states, introduced by sp^2 bonds. | 70 |
| 5.1 | Band schematics of the proposed diamond-Si structure, showing electrons being excited in the absorbing substrate and contributing to the photon-enhanced emission through the low work function surface. | 76 |

| | | |
|-----|---|----|
| 5.2 | Simulation results of the two models on an ideal electron emitter, which has a band gap of 1.12 eV, electron affinity of 0.5 eV, and is under illumination of 400 nm light with a photon flux of $10^{15} \text{ cm}^{-2}\text{s}^{-1}$ | 81 |
| 5.3 | High resolution electron microscopy image of the diamond/Si interface, showing the (N)UNCD on the left and single crystal Si on the right. | 82 |
| 5.4 | UV (21.2 eV) photoemission spectra of a nitrogen doped diamond film on <i>p</i> -type Si substrate. An effective work function of ~ 1.5 eV was observed and kept relatively independent of temperature. | 83 |
| 5.5 | Photo-induced emission spectra from nitrogen-doped diamond films on Si. The Si substrates are of (a) <i>p</i> -type doping and (b) <i>n</i> -type doping. | 84 |
| 5.6 | (a) Temperature dependence of integrated photo-induced emission intensity and thermionic emission intensity, obtained from a nitrogen-doped diamond film on a <i>p</i> -type Si substrate, showing results with different excitation energies; (b) Comparison between simulated (direct photo-emission and PETE models) and experimental results (spectral intensity and photocurrent). A combined curve of 50% direct photo-emission and 50% PETE is shown with the dashed line, indicating a contribution from the two generation processes. | 86 |
| 6.1 | Band schematics of the two models: (a) The barrier at the oxide-diamond interface effectively reduces the electron emission threshold, creating a NEA surface; (b) The metal-oxide dipole at the diamond surface changes the vacuum level, which is lower than the CBM, leading to a NEA. | 94 |

| | | |
|-----|--|-----|
| 6.2 | (a) XPS scans of C 1s, (b) O 1s peaks, and (c) UPS scans of a nitrogen-doped diamond film, with H- and O-termination respectively. The results indicate a negative electron affinity on the H-terminated surface and a positive electron affinity on the O-terminated surface. In (c) the E_F relative to low energy cut-off occurs at a binding energy of 21.2 eV corresponding to the photon energy. The effective work function is the energy from this point to the back cut-off. | 98 |
| 6.3 | XPS and UPS scans of a boron-doped diamond sample with 0.1 nm V, showing the (a) V 2p _{3/2} and O 1s peaks, (b) C 1s peak, and (c) effective work function after each process. | 100 |
| 6.4 | XPS and UPS scans of a nitrogen-doped diamond sample with 0.1 nm V, showing the (a) V 2p _{3/2} and O 1s peaks, (b) C 1s peak, and (c) effective work function after each process. | 102 |
| 6.5 | UPS spectra of a BDD sample coated with 0.5 nm V deposition. | 104 |
| 6.6 | Band schematics of vanadium-oxide-termination on (a) BDD and (b) NDD substrates, assuming a 4.4 eV work function for the vanadium oxide film. On the BDD sample the vacuum level lies close to the diamond CBM, and leads to a low PEA of 0.6 eV; On the NDD sample, the vacuum level is significantly higher than the diamond CBM, leading to a PEA of 1.6 eV. | 105 |

CHAPTER 1

INTRODUCTION

1.1 Negative electron affinity and *n*-type doping of diamond

Possibly the most unusual property of diamond is its ability to attain a negative electron affinity (NEA) surface when it is hydrogen-terminated after exposure to a hydrogen plasma. In a NEA material, the position of vacuum level (E_{Vac}) is below the conduction band minimum (CBM), and electrons in the conduction band can be emitted from the surface into vacuum directly without overcoming any energy barrier. Consequently, the effective work function of a NEA material, Φ_w , is defined as the energy difference between its CBM and the Fermi level (E_F), instead of that between E_{Vac} and E_F for the more common positive electron affinity (PEA) materials. The NEA properties of diamond (100) and (111) surfaces have been studied [1, 2], which are associated with the hydrogen bonded to the surface [3, 4]. The C-H bonds at the surface create a dipole due to charge transfer between the H adatoms and the topmost layer of C atoms [5]. This surface dipole layer effectively changes the relative position of E_{Vac} , which is decrease to ~ 1.1 - 1.3 eV below the diamond CBM [5-7]. In contrast, with oxygen-termination the diamond surface exhibits an increased electron affinity of ~ 1.7 eV [7]. Desorption of hydrogen from the diamond surface has been observed at ~ 900 °C [8], while oxygen is removed at ~ 600 °C [9]. With the removal of hydrogen, the clean (100)-(2 \times 1) reconstructed surface of diamond exhibits a PEA of 0.38 eV [5]. In addition to hydrogen termination, other surface termination techniques have also been established in order to provide thermally stable NEA. For example, coating of the diamond surface

with a thin layer of metal [10-12] or metal oxide [13, 14] has been found to affect the surface electron affinity.

In addition to the ability of attaining NEA, diamond has several outstanding attributes, its high thermal conductivity and stability is well established as is its chemical inertness: diamond is stable in air at temperatures up to 600 °C and unaffected by temperatures exceeding 1200 °C in a vacuum. Yet intrinsic diamond has a negligible electric conductivity due to a wide bandgap (5.47 eV at ambient temperature), which has severely limited its electronics-related applications. In the last few decades, with the advances of chemical vapor deposition (CVD) techniques for diamond synthesis, impurity doping of diamond has shown rapid development through introducing precursors containing the dopant into the reaction chamber. Diamond can be doped *p*-type with boron, which has an acceptor level at ~ 0.37 eV above the valence band maximum (VBM) [15]. On the other hand, *n*-type doping of diamond has been established by incorporation of nitrogen or phosphorus, with a donor level of nitrogen at 1.7 eV [16] and that of phosphorus at 0.4-0.6 eV [17, 18] below the CBM. A band schematic of doped diamond with different surface terminations is illustrated in Fig. 1.1. Evidently, *n*-type doping leads to lowering of the electron emission threshold, due to the shift of E_F towards the CBM of diamond with increasing donor concentration [19]. However, strong upward band bending and a resultant large work function are typically found for single crystal nitrogen doped films, which is attributed to the presence of empty acceptor-like surface states. Such upward band bending has resulted in a work function > 3 eV [6, 20].

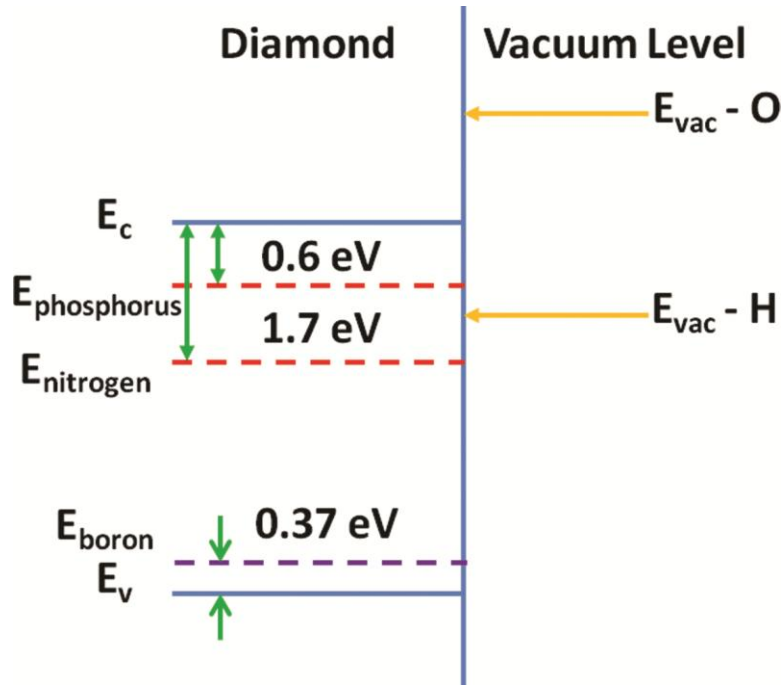


Fig. 1.1 Band schematic of doped diamond, showing the energy levels of the different dopants, and vacuum levels with hydrogen or oxygen termination.

Recently, low work function *n*-type doped diamond films have been grown by microwave plasma enhanced chemical vapor deposition (MPCVD). By introducing argon into the deposition process, the grain size of these CVD diamond films can be controlled below 10 nm [21]. These nanocrystalline diamond films do not show upward band bending upon *n*-type doping, suggesting that incorporated sp^2 bonds at the grain boundaries [22] can apparently provide sufficient electrons to compensate the acceptor-like surface states. With the impact of band bending mitigated, work function of 1.3 eV with nitrogen-doping [23] and 0.9 eV with phosphorus-doping [24] have been reported. These results indicate that nitrogen-doped diamond films display one of the lowest work functions of any non-cesiated material.

To summarize, recent developments in MPCVD synthesis of *n*-type doped, hydrogen-terminated diamond have provided an excellent template for surface science and material physics research. The low work function of these diamond films can lead to strong electron emissivity if proper excitation is provided, e.g. thermionic ionization or photoelectron generation. These processes, particularly photo-induced electron emission, are not yet thoroughly studied, and thus serve as the main motivation of this thesis.

1.2 Thermionic electron emission and thermionic energy conversion

Thermionic electron emission is the physical process that electrons in a material obtain enough kinetic energy from heat to overcome the potential barrier and escape from its surface. As described by the Richardson-Dushman model [25, 26], thermionic emission is characterized by two parameters of the material: the work function Φ_W and the Richardson's constant A_R^* . The electron emission current density, $J(T)$, is expressed as a function of emitter temperature T :

$$J(T) = A_R^* T^2 \exp\left(-\frac{\Phi_W}{k_B T}\right), \quad (1.1)$$

where A_R^* is in the form of:

$$A_R^* = \frac{4\pi m_n^* k_B^2 e^2}{h}, \quad (1.2)$$

with Boltzmann's constant k_B , electronic charge e , and Planck's constant h , and the electron effective mass m_n^* . Eq. (1.1) can be converted into the following term:

$$\ln\left(\frac{J(T)}{T^2}\right) = -\frac{\Phi_W}{k_B} \left(\frac{1}{T}\right) + \ln(A_R^*). \quad (1.3)$$

This equation is frequently utilized to characterize thermionic emitters in an experimental setup that measures J and T , and a linear fit is executed to determine Φ_W and A_R^* . For an ideal material that $m_n^* = m_n$ ($\sim 9.11 \times 10^{-31}$ kg), $A_R^* = 120 \text{ A/cm}^2\text{K}^2$. It has been observed, though, that the Richardson's constant for most materials deviates from this theoretical value, as listed in Table 1.1.

Table 1.1 Work function and Richardson constant of some common materials for thermionic applications [27].

| Material | W [eV] | A_R^* [$\text{A cm}^{-2} \text{K}^{-2}$] |
|------------------------|--------|--|
| Molybdenum | 4.15 | 55 |
| Nickel | 4.61 | 30 |
| Tantalum | 4.12 | 60 |
| Tungsten | 4.54 | 60 |
| Barium | 2.11 | 60 |
| Cesium | 1.81 | 160 |
| Ba coating on W | 1.56 | 1.5 |
| Cs coating on W | 1.36 | 3.2 |
| BaO + SrO | 0.95 | $\sim 10^{-2}$ |
| LaB ₆ | 2.70 | 29 |
| Nitrogen-doped diamond | 1.28 | 2.12 |

Vacuum thermionic electron emission has been considered for energy conversion applications. A thermionic energy converter (TEC) is composed of two plates separated by a vacuum gap, one as the electron emitter and the other as the electron collector.

Schematics and band diagram of a TEC device are illustrated in Fig. 1.2. When a temperature difference is maintained between the hot emitter and the cold collector, a thermionic emission current is formed across the gap and thus converting heat to electricity. The efficiency of a TEC is defined as the output electrical power against the energy losses. Simulations have indicated that the maximum conversion efficiency is achieved when the voltage difference between the emitter and collector pair is equal to the difference in their work function divided by the elementary charge:

$$\eta_{ThE,max} = \frac{J \cdot (\Phi_E - \Phi_C) / e}{J \cdot (\Phi_E + 2k_B T_E) / e + P_L}, \quad (1.4)$$

where P_L is the net extraneous power loss per unit emitting area, e.g. Stephan-Boltzmann radiation loss, etc. [28]. Advantages of TECs are their high efficiency [29] and low maintenance, as no mechanically moving parts are involved in the device configuration. One example is the TOPAZ program developed first by Soviet Union and then jointly with the United States for powering satellites [30], in which electricity was produced by a high-temperature thermionic converter based on a light weight nuclear reactor. However, the operation temperatures of greater than 1000 °C have precluded most earth based applications [31].

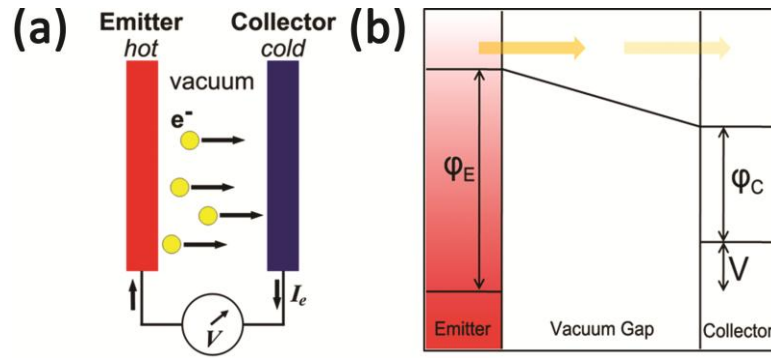


Fig. 1.2 (a) Configuration and (b) band schematic of a thermionic energy converter. Electrons flow from the hot emitter to the cold collector, and produce an output electric power.

From Eq. (1.1), if the emitter is required to operate at a lower temperature T , the most direct approach to maintain or increase the thermionic emission current is to decrease Φ_w . Rare earth metals typically exhibit a small work function. For example, Φ_w of Eu, Sm and Gd are 2.5, 2.7 and 2.9 eV respectively [32]. Yet these metals are susceptible to sublimation and oxidation, and are not suitable for applications at high temperature or in a low vacuum environment. Surface coating of the emitter with cesium oxide can effectively reduce the work function of refractory metals such as tungsten [33], but applications are limited due to its lack of stability to withstand high temperature operation. Due to the recent development of low work function materials, thermionic energy conversion has shown increased scientific and device engineering research. As thermionic electron emission and vacuum thermionic energy conversion from n -type doped diamond films and diamond-based materials have been achieved, at temperatures as low as 500 °C [23, 24, 34-37], diamond films and coatings are now promising candidates for thermionic energy conversion applications. Results have shown that the performance of a diamond-based TEC can be significantly increased by engineering the

interface between the diamond film and the metal substrate [38], and by introducing certain ionized gas species into the emitter-collector gap to exploit the molecular charge transfer process [39]. On the other hand, the efficiency of the current diamond thermionic emitters is still limited by their relatively small Richardson constant [40], and the evolution of hydrogen at temperatures above 800 °C [41].

While much progress has been made on improving the materials, studies have also been focused on modifying the TEC device design to optimize their efficiency. One of the most important challenges of TECs is to minimize the space-charge effect, i.e. the electron cloud in the vacuum gap produces an increased motive which limits the maximum emission current. To provide an accurate analysis, quasi-equilibrium models of electron transport across the gap have been successfully employed through the Langmuir theory [42], which is based on numerical solutions of the Vlasov-Poisson equations:

$$v_{ex} \frac{\partial f_e}{\partial x} - \frac{1}{m_e} \frac{d\Psi}{dx} \frac{\partial f_e}{\partial v_{ex}} = 0, \quad (1.5)$$

$$\frac{d^2\Psi}{dx^2} = -\frac{e^2 n_e}{\epsilon_0}, \quad (1.6)$$

$$n_e(x_m) = \int_0^\infty dv_{ex} \int_{-\infty}^\infty dv_{ey} \int_{-\infty}^\infty dv_{ez} f_e(x_m, v_e). \quad (1.7)$$

Based on this methodology, simulations have been developed on evaluating the space-charge limited efficiency of TECs with NEA emitters [43-45]. The effects of NEA collectors have also been examined recently [46]. Results have shown that the space-charge-limitation can be mitigated by optimizing the device configuration, especially the emitter-collector gap [47, 48]. It should be noted that practical TECs can be affected by

various factors initially ignored in ideal models, and improving the device designs as well as the material properties are still crucial issues in TEC research and development.

1.3 Photo-induced electron emission of diamond

Photons have been employed to generate electron emission from materials through the photoelectric effect. The photoemission process is usually understood in terms of a 3-step process, suggested by Spicer [49]: electrons are first excited to states above the vacuum level, then transported to the sample surface, and finally emitted into vacuum. For a metallic material with a continuous distribution of electrons below the Fermi level (E_F), the photoemission process can be described by the Fowler-DuBridge model [50-52], on the fundamental assumption that an excited electron needs not only an energy higher than the work function, but also enough perpendicular momentum to overcome the surface barrier, to be emitted into vacuum. Thus the concentration of available photoelectrons per absorbed photon is given as [50]:

$$N = \frac{2\sqrt{2}\pi(m_n^*)^{3/2}}{h^3} \cdot \frac{k_B^2 T^2}{(\chi_0 - h\nu)^{1/2}} \cdot \left[\frac{\pi^2}{6} + \frac{1}{2} \left(\frac{h\nu - \Phi_w}{k_B T} \right)^2 + \sum_{n=1}^{\infty} \frac{1}{n^2} \left(-\exp\left(\frac{\Phi_w - h\nu}{k_B T} \right) \right)^n \right], \quad (1.8)$$

where $h\nu$ is the photon energy, and χ_0 is the total height of the potential step at the boundary (a value often sufficiently large that $\chi_0 - h\nu$ is treated as relatively constant). It should be noted that, unlike thermionic electron emission as described in Eq (1.1), Eq. (1.8) displays weak temperature dependence when the photon energy is sufficiently higher than the work function.

In a semiconductor with a bandgap, the density of states (DoS) in both the conduction band and the valence band will limit the photo-generation across the gap. This

leads to the methods suggested by Spicer [53] and Powell [54], which evaluate the photo-yield with modifications on the Fowler assumption:

$$Y(h\nu) = \frac{\int_{E_G}^{h\nu} T(E)S(E, h\nu)N_c(E)N_v(E - h\nu)dE}{\int_{E_G}^{h\nu} N_c(E)N_v(E - h\nu)dE}, \quad (1.9)$$

in which N_c and N_v are the conduction band and valence band DoS respectively. $T(E)$ is the electron escape function and $S(E, h\nu)$ is the optical absorption function, both dependent on material properties.

Photoemission from different materials is commonly described in terms of the effective quantum efficiency (QE), which is defined as the ratio of the number of electrons gained over the number of illuminating photons. From the Fowler-DuBridge model, Eq. (1.8), the QE of metallic photo-cathodes is approximately a quadratic function of the difference between photon energy and the work function, and many materials have been shown to follow this relationship [55].

A number of instruments employing the photoelectron emission principles have been used to characterize the diamond-based materials, including ultra-violet photoelectron spectroscopy (UPS) which provides the electron energy distribution [2, 20, 37, 56, 57], photo-electron emission microscopy (PEEM) for characterizing the spatial emission pattern [58-61], and total photoyield spectroscopy [6, 62], etc.. However, photoelectron emission of diamond has been limited by the wide bandgap and consequent large photoemission threshold, and a photon energy above the band gap of diamond is typically required for excitation.

Nevertheless, photoelectron generation from NEA diamond has been applied in various fields, including photoelectrochemistry templates [63-66] and photo-cathodes

[67, 68]. With the recent progresses of preparing low work function *n*-type doped diamond films, a study of their photoelectron emission characteristics is important to determine their potential in such applications, particularly in the visible light regime which was not possible for previous studies. In addition, there have been reports on electron emission due to visible light illumination, from other carbon-based materials, e.g. carbon nanotube arrays [69-72] and nanopetal arrays [73]. While these studies indicate several different physical mechanisms, the results and analysis methods can provide insight for similar studies of low work function diamond films for understanding the related photoemission properties.

1.4 Photon-enhanced thermionic emission

Studies have explored combinations of different electron emission mechanisms to seek new approaches to enhance electron emission efficiency. As noted in 1.3, studies have reported using a combination of the photo- and thermal generation to achieve electron emission from carbon-based materials [69-72]. This combination is particularly effective in improving the efficiency of energy conversion applications [74], where the enhancement from a strong electric field is usually not available.

A novel emission mechanism that follows this approach is photon-enhanced thermionic emission (PETE). Experimental evidence supporting the effect has been obtained for *p*-type GaN [75]. A band schematic of a semiconductor exhibiting PETE is shown in Fig. 1.3 (a). Photons with energy above the band gap of the *p*-type semiconductor generate electrons in the conduction band. If this generation step is more significant than recombination across the bandgap, an enhanced electron population is

formed in the conduction band. The electron quasi-Fermi level in the semiconductor hence shifts towards the CBM. As a result of the altered electron energy distribution, the effective thermionic emission threshold is reduced to the electron affinity of the material, and the electron emission intensity is significantly enhanced:

$$J_{PETE} = \left(\frac{4\pi e m_n^* k_B}{h^3} \right) T^2 \exp\left(\frac{-(\Phi_W - (E_{F,n} - E_F))}{k_B T} \right) = A_R^* T^2 \exp\left(-\frac{\chi}{k_B T} \right). \quad (1.10)$$

Fig. 1.3 (b) shows schematics of a concentrated solar cell that employs the PETE process. The proposed cell is composed of two parallel plates separated by a vacuum gap, one serving as the electron emitter and the other the collector. Concentrated solar light illuminates the back of the emitter plate to induce PETE, and the enhanced electron emission is directed towards the collector, with a specific temperature difference across the gap to optimize the device performance. Through optimizing the parameters of the device design [76], the maximum efficiency of the PETE-emitter is expected to be greater than traditional thermionic devices or solar cells.

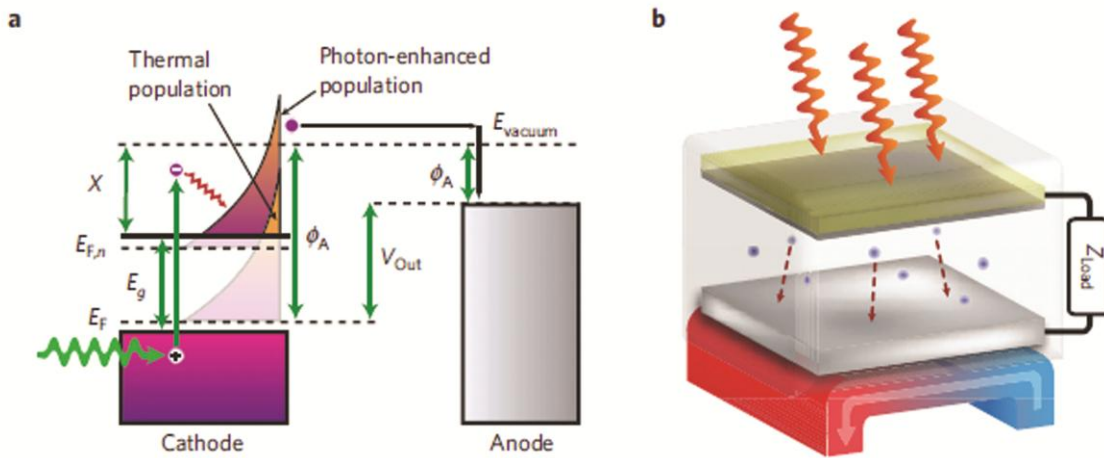


Fig. 1.3 (a) Band schematic and (b) device illustration of a photon-enhanced thermionic energy converter [75]. An enhanced electron population in the emitter is created through

photon illumination, and the thermionic emission current towards the collector is significantly increased.

One of the most significant differences between the PETE-based solar energy converter and conventional concentrated solar cells is the dependence on device temperature, which is directly related to the heat generated from concentrating lenses in the system. As described above, a PETE energy converter requires a moderate-to-high temperature to efficiently utilize both photo- and thermionic excitation. On the other hand, solar cells based on solid state junctions have significantly reduced efficiency at elevated temperatures [77]. Therefore the PETE energy converters may not need active cooling which is necessary for most other concentrated solar cells. Additionally, the unused heat absorbed in the collector plate can be further reclaimed through a thermal engine, thus creating a PETE/thermal tandem system in which a conversion efficiency beyond 50% is indicated [75].

Several theoretical studies have analyzed the performance of PETE-based devices. Other than the simplified zero-dimensional model based on generation-recombination quasi-equilibrium, 1-D models that include the drift, diffusion and recombination of photon-enhanced electrons across the devices have shown effects of electron transport mechanisms on the overall energy conversion efficiency [78-80]. The principles of PETE can be similarly applied in solid-state solar cells by engineering heterojunctions that preferentially extract electrons or holes [81]. Additionally, methods for mitigating the space-charge limitation are also under consideration [82].

One unusual approach of applying PETE in solar energy conversion is to adapt it for an isothermal device configuration, i.e. the emitter and collector plates are operated at

the same temperature [83]. In an isothermal PETE device the reverse current emitted from the collector is not negligible, and thus there is an optimized operation regime where the maximum solar-to-electricity conversion efficiency can be achieved. By engineering the geometrical design of an isothermal device, the net emission could be further enhanced by engineering the ratio between the emission area and the illumination area, as illustrated in Fig. 1.4. Unlike thermionic energy conversion devices, the vacuum gap is not required to maintain the temperature difference. Thus, the gap spacing can be adjusted to minimize space charge effects, which also simplifies device manufacturing as another advantage.

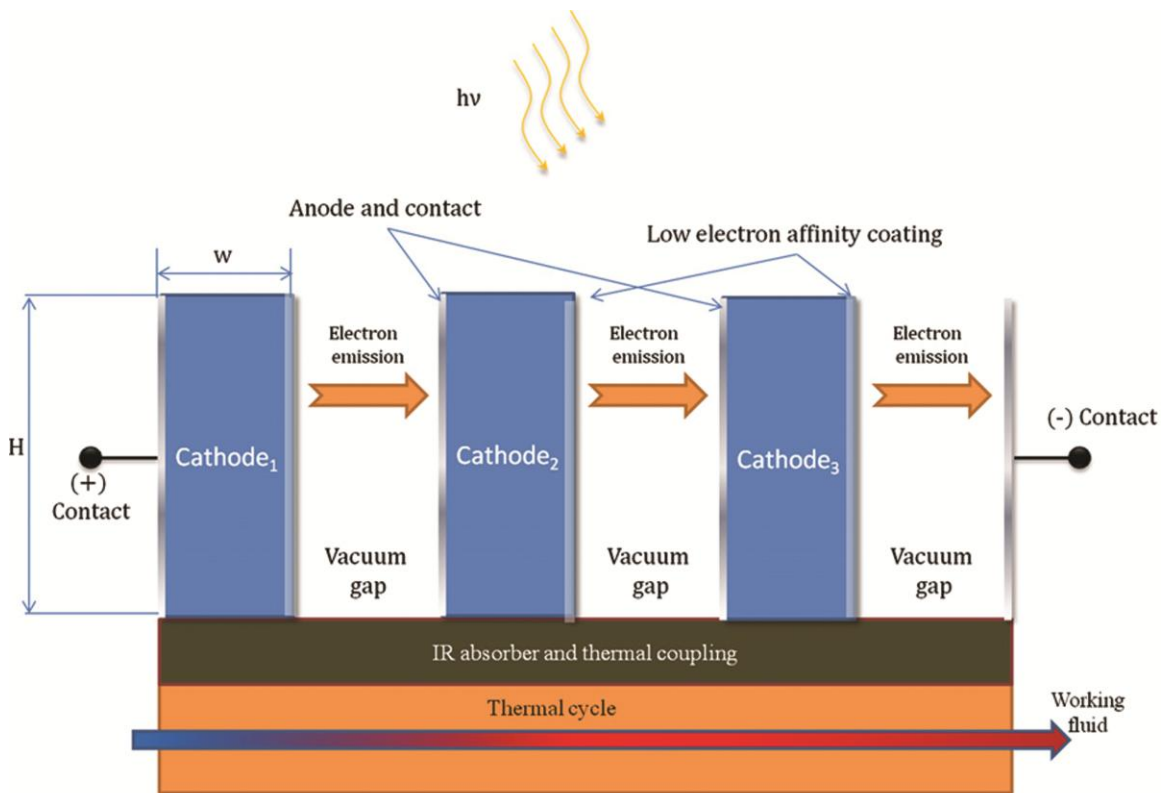


Fig. 1.4 Schematic of an isothermal-PETE energy conversion device [83]. Light illumination is provided from the top and converted into enhanced emission from the side

emitter. The device is maintained at the same temperature, while excess heat flow is transferred to a thermal engine.

It should be noted that phosphorus-doped diamond films have been considered for the collector of a PETE conversion device [75]. Considering its wide bandgap, diamond itself is not a preferred candidate for a PETE emitter; yet if combined with other suitable photon-absorbing materials into a bi-layer structure with an optimized interface [84], it is possible that the low work function of the *n*-type diamond films can be utilized to assist the PETE process.

Overall, the PETE mechanism is an innovative approach for efficient energy conversion, and is especially preferred for applications in concentrated solar cells. To date, experimental demonstrations of the PETE process are still limited, yet theoretical studies based on solid-state and vacuum physics have shown its promising future. Should a practical device development strategy be established, it has the potential to be a market-disruptive approach that could help meet today's ever-growing need for energy harvesting.

1.5 Thesis approach

This thesis is focused on combined photo-induced and thermionic electron emission from low work function diamond. Through spectroscopic measurements of the diamond samples under photon illumination at various temperatures, the physical mechanisms and material properties involved in the emission processes are investigated, with an aim of providing a novel approach for efficient solar and thermal energy conversion.

Chapter 2 introduces essential information about the instruments and analysis method, including the two photoemission electron spectroscopy systems (XPS and UPS) used for sample characterization and the xenon arc lamp system employed as the photon source.

Visible light photo-induced electron emission from nitrogen-doped diamond films deposited on molybdenum substrates is investigated in chapter 3. A low effective work function was observed, which limited both thermionic and photoemission processes. A simplified phonon-scattering model was proposed to analyze the energy distribution of the photoelectron spectrum. Additionally, similar results of photo-induced electron emission from phosphorus-doped diamond films are also introduced.

Chapter 4 is a study of combined photo-induced and thermionic electron emission from nitrogen-doped diamond films on metal substrates, with sample sets prepared with different interface and interlayer conditions and characterized in order to understand the effect of film structure on the emission characteristics. The quality of the metal-diamond interface was found to substantially impact the threshold of the sub-bandgap photo-induced emission, as photoelectron generation appeared to involve both the ultra-nanocrystalline diamond and the diamond/metal interface.

A configuration is proposed and investigated in chapter 5, which combines a nitrogen-doped, hydrogen-terminated diamond film and a silicon substrate into an electron emitter based on the photon-enhanced thermionic (PETE) emission mechanism. In the proposed model, the illuminating photons provide an enhanced electron population in the absorbing substrate, which results in electron emission through the low work function surface. The temperature dependences of photo-induced electron emission from

these nitrogen-doped diamond films were examined, while modeling results based on different physical mechanisms indicated evidence of the PETE effect in a complex generation process.

In chapter 6, a study is presented of the electron affinity of vanadium-oxide-terminated diamond samples, in order to examine and compare the properties of both boron and nitrogen doped diamond. With vanadium-oxide-termination and thermal annealing, a negative electron affinity was found on boron-doped diamond, while a positive electron affinity was found on nitrogen-doped diamond. A model based on the barrier at the diamond-oxide interface was suggested to describe the difference between samples with different doping types.

Chapter 7 summarizes the most crucial results in this thesis, while future studies based on the current work are also proposed.

References

- [1] F.J. Himpsel, J.A. Knapp, J.A. VanVechten, D.E. Eastman, "Quantum Photoyield of Diamond (111) - A Stable Negative-Affinity Emitter", *Phys. Rev. B* 20 (1994): 624.
- [2] J. van der Weide, Z. Zhang, P.K. Baumann, M.G. Wensell, J. Bernholc, R.J. Nemanich, "Negative-Electron-Affinity Effects on Diamond (100) surface", *Phys. Rev. B* 60 (1994): 8.
- [3] B.B. Pate, M.H. Hecht, C. Binns, I. Lindau, W.E. Spicer, "Photoemission and Photon-Stimulated Ion Desorption Studies of Diamond(111): Hydrogen", *J. Vac. Sci. Technol.* 21 (1982): 364.
- [4] B.B. Pate, "The Diamond Surface: Atomic and Electronic Structure", *Surf. Sci.* 165 (1986): 83.
- [5] J.B. Cui, J. Ristein, L. Ley, "Electron Affinity of the Bare and Hydrogen Covered Single Crystal Diamond (111) Surface", *Phys. Rev. Lett.* 81 (1998): 429-432.

- [6] D. Takeuchi, H. Kato, G.S. Ri, T. Yamada, P.R. Vinod, D. Hwang, C.E. Nebel, H. Okushi, S. Yamasaki, "Direct Observation Of Negative Electron Affinity In Hydrogen-Terminated Diamond Surfaces", *Appl. Phys. Lett.* 86 (2005): 152103.
- [7] F. Maier, J. Ristein, L. Ley, "Electron Affinity Of Plasma-Hydrogenated And Chemically Oxidized Diamond (100) Surfaces", *Phys. Rev. B* 64 (2001): 165411.
- [8] T. Haensel, J. Uhlig, R.J. Koch, S. I.-U. Ahmed, J.A. Garrido, D. Steinmüller-Nethl, M. Stutzmann, J.A. Schaefer, "Influence of Hydrogen on Nanocrystalline Diamond Surfaces Investigated with HREELS and XPS", *Phys. Status Solidi A* 206 (2009): 2022-2027.
- [9] R.E. Thomas, R.A. Rudder, R. J. Markunas, "Thermal Desorption From Hydrogenated And Oxygenated Diamond (100) Surfaces", *J. Vac. Sci. Technol. A* 10 (1992): 2451.
- [10] J. van der Weide, R. J. Nemanich, "Schottky Barrier Height And Negative Electron Affinity Of Titanium On (111) Diamond", *J. Vac. Sci. Technol. B* 10 (1992): 1940.
- [11] P.K. Baumann, S.P. Bozeman, B.L. Ward, R.J. Nemanich, "Characterization of Metal-Diamond Interfaces: Electron Affinity and Schottky Barrier Height". *Diam. Relat. Mater.* 6 (1997): 398-402.
- [12] P.K. Baumann, R.J. Nemanich, "Electron Affinity and Schottky Barrier Height of Metal-Diamond (100), (111), and (110) Interfaces", *J. Appl. Phys.* 83 (1998): 2072.
- [13] K.P. Loh, X.N. Xie, S.W. Yang, J.S. Pan, P. Wu, "A Spectroscopic Study of the Negative Electron Affinity of Cesium Oxide-Coated Diamond (111) and Theoretical Calculation of the Surface Density-of-States on Oxygenated Diamond (111)", *Diam. Relat. Mater.* 11 (2002): 1379-1384.
- [14] K.M. O'Donnell, T.L. Martin, N.A. Fox, D. Cherns, "Ab Initio Investigation of Lithium on the Diamond C(100) Surface", *Phys. Rev. B* 82 (2010): 115303.
- [15] K. Thonke, "The Boron Acceptor in Diamond". *Semicond. Sci. Technol.* 18 (2003): S20-S26.
- [16] R.G. Farrer, "On the Substitutional Nitrogen Donor in Diamond", *Solid State Commun.* 7 (1969): 685-688.
- [17] S. Koizumi, M. Kamo, Y. Sato, H. Ozaki, T. Inuzuka, "Growth and Characterization of Phosphorous Doped {111} Homoepitaxial Diamond Thin Films", *Appl. Phys. Lett.* 71 (1997): 1065.
- [18] K. Haenen, K. Meykens, M. Nesladek, G. Knuyt, L.M. Stals, T. Teraji, S. Koizumi, E. Gheeraert, "Phonon-Assisted Electronic Transitions in Phosphorus-Doped N-Type Chemical Vapor Deposition Diamond Films", *Diam. Relat. Mater.* 10 (2001): 439-443.

- [19] A.T. Collins, "The Fermi Level in Diamond", *J. Phys.: Condens. Matter.* 14 (2002): 3743.
- [20] L. Diederich, O. Kuttel, P. Aebi, L. Schlapbach, "Electron Affinity and Work Function of Differently Oriented and Doped Diamond Surfaces Determined by Photoelectron Spectroscopy", *Surf. Sci.* 418 (1998): 219-239.
- [21] O.A. Williams, "Nanocrystalline Diamond", *Diam. Relat. Mater.* 20 (2011): 621-640
- [22] S. Bhattacharyya, "Mechanism of High N-Type Conduction in Nitrogen-Doped Nanocrystalline Diamond", *Phys. Rev. B* 70 (2004): 125412.
- [23] F.A.M. Koeck, R.J. Nemanich, "Low Temperature Onset for Thermionic Emitters Based on Nitrogen Incorporated UNCD Films", *Diam. Relat. Mater.* 18 (2009): 232-234.
- [24] F.A.M. Koeck, R.J. Nemanich, A. Lazea, K. Haenen, "Thermionic Electron Emission from Low Work-Function Phosphorus Doped Diamond Films", *Diam. Relat. Mater.* 18: (2009): 789-791.
- [25] O.W. Richardson, "Electron Emission from Metals as a Function of Temperature", *Phys. Rev.* 23 (1924): 153.
- [26] S. Dushman, "Thermionic Emission", *Rev. Mod. Phys.* 2 (1930): 381.
- [27] V.S. Fomenko, *Handbook of Thermionic Properties: Electronic Work Functions and Richardson Constants of Elements and Compounds* (New York: Springer, 1966).
- [28] N.S. Rasor, "Figure of Merit for Thermionic Energy Conversion", *J. Appl. Phys.* 31 (1960): 163.
- [29] H.F. Webster, "Calculation of the Performance of a High Vacuum Thermionic Energy Converter", *J. Appl. Phys.* 30 (1959): 488.
- [30] I.P. Bogush, G.M. Gryaznov, E.E. Zhabotinskii, A.N. Makarov, V.I. Serbin, Y.L. Trukhanov, "Thermionic Space Nuclear-Power Systems Within the TOPAZ Program - Construction Principles and Operating Regimes", *Sov. At. Energy* 70 (1991): 263-266.
- [31] Committee on Thermionic Research and Technology, Aeronautics and Space Engineering Board, National Research Council. *Thermionics Quo Vadis? An Assessment of the DTRA's Advanced Thermionics Research and Development Program* (Washington, D.C.: National Academies Press, 2001).
- [32] W.M. Haynes, *CRC Handbook of Chemistry and Physics, 94th edition* (Boca Raton: CRC Press, 2013-2014).
- [33] J.L. Coggins, R.E. Stickney, " Adsorption Studies Based on Thermionic Emission Measurements: I. Cesium on Single-Crystal Tungsten", *Surf. Sci.* 11 (1968): 355-369.

- [34] M. Suzuki, T. Ono, N. Sakuma, T. Sakai, "Low-Temperature Thermionic Emission from Nitrogen-Doped Nanocrystalline Diamond Films on N-Type Si Grown by MPCVD", *Diam. Relat. Mater.* 18 (2009): 1274-1277.
- [35] Y.M. Wong, W.P. Kang, J.L. Davidson, S. Raina, J.H. Huang, "Carbon Nanostructures as Thermal Field Emitters for Waste Heat Recovery", *Diam. Relat. Mater.* 18 (2009): 563-566.
- [36] K. Uppireddi, T.L. Westover, T.S. Fisher, B.R. Weiner, G. Morell, "Thermionic Emission Energy Distribution from Nanocrystalline Diamond Films for Direct Thermal-Electrical Energy Conversion Applications", *J. Appl. Phys.* 106 (2009): 043716.
- [37] M. Kataoka, C. Zhu, F.A.M. Koeck, R.J. Nemanich, "Thermionic Electron Emission from Nitrogen-Doped Homoepitaxial Diamond", *Diam. Relat. Mater.* 19 (2010): 110-113.
- [38] F.A. M. Koeck, R.J. Nemanich, "Substrate-Diamond Interface Considerations for Enhanced Thermionic Electron Emission from Nitrogen Doped Diamond Films", *J. Appl. Phys.* 112 (2012): 113707.
- [39] F.A.M. Koeck, R.J. Nemanich, Y. Balasubramaniam, K. Haenen, J. Sharp, "Enhanced Thermionic Energy Conversion and Thermionic Emission from Doped Diamond Films Through Methane Exposure", *Diam. Relat. Mater.* 20 (2011) 1229-1233.
- [40] T.D. Musho, W.F. Paxton, J.L. Davidson, D.G. Walker, "Quantum Simulation of Thermionic Emission from Diamond Films", *J. Vac. Sci. Technol. B* 31 (2013): 021401.
- [41] W.F. Paxton, M. Howell, W.P. Kang, J.L. Davidson, "Influence of Hydrogen on The Thermionic Electron Emission from Nitrogen-Incorporated Polycrystalline Diamond Films", *J. Vac. Sci. Technol. B* 30 (2012): 021202.
- [42] G. Hatsopoulos, E. Gyftopoulos, *Thermionic Energy Conversion* (Cambridge: MIT Press, 1973).
- [43] J.R. Smith, G.L. Bilbro, R.J. Nemanich, "Using Negative Electron Affinity Diamond Emitters to Mitigate Space Charge in Vacuum Thermionic Energy Conversion Devices", *Diam. Relat. Mater.* 15 (2006): 2082-2085.
- [44] J.R. Smith, G.L. Bilbro, R.J. Nemanich, "Considerations for a High-Performance Thermionic Energy Conversion Device Based on a Negative Electron Affinity Emitter", *Phys. Rev. B* 76 (2007): 245327.
- [45] J.R. Smith, G.L. Bilbro, R.J. Nemanich, "Theory of Space Charge Limited Regime of Thermionic Energy Converter with Negative Electron Affinity Emitter", *J. Vac. Sci. Technol. B* 27 (2009): 1132-1141.

- [46] J.R. Smith, "Increasing the Efficiency of a Thermionic Engine Using a Negative Electron Affinity Collector", *J. Appl. Phys.* 114 (2013): 164514.
- [47] J.-H. Lee, I. Bargatin, N.A. Melosh, R.T. Howe, "Optimal Emitter-Collector Gap for Thermionic Energy Converters", *Appl. Phys. Lett.* 100 (2012): 173904.
- [48] K.A. Littau, K. Sahasrabudde, D. Barfield, H. Yuan, Z.-X. Shen, R.T. Howe, N.A. Melosh, "Microbead-Separated Thermionic Energy Converter with Enhanced Emission Current", *Phys. Chem. Chem. Phys.* 15 (2013): 14442.
- [49] W.E. Spicer, "Photoemissive, Photoconductive, and Optical Absorption Studies of Alkali-Antimony Compounds", *Phys. Rev.* 112 (1958): 114-122.
- [50] R.H. Fowler, "The Analysis of Photoelectric Sensitivity Curves for Clean Metals at Various Temperatures", *Phys. Rev.* 38 (1931): 45.
- [51] L.A. DuBridge, "Theory of the Energy Distribution of Photoelectrons", *Phys. Rev.* 43 (1933): 727-741.
- [52] K.L. Jensen, P.G. O'Shea, D.W. Feldman, N.A. Moody, "Theoretical Model of the Intrinsic Emittance of a Photocathode", *Appl. Phys. Lett.* 89 (2006): 224103.
- [53] N.B. Kindig, W.E. Spicer, "Band Structure of Cadmium Sulfide - Photoemission Studies", *Phys. Rev.* 138 (1965): A561-576.
- [54] R.J. Powell, "Interface Barrier Energy Determination from Voltage Dependence of Photoinjected Currents", *J. Appl. Phys.* 41 (1970): 2424-2432.
- [55] V.G. Tkachenko, A.I. Kondrashev, I.N. Maksimchuk, "Advanced Metal Alloy Systems for Massive High-Current Photocathodes", *Appl. Phys. B* 98 (2010): 839-849.
- [56] C. Bandis, B.B. Pate, "Photoelectric Emission from the Negative Electron Affinity (100) Diamond Surface - Exciton Effects", *Surf. Sci.* 350 (1996): 315-321.
- [57] J.B. Cui, J. Ristein, L. Ley, "Low-Threshold Electron Emission from Diamond", *Phys. Rev. B.* 60 (1999): 16135-16142.
- [58] R.J. Nemanich, S.L. English, J.D. Hartman, A.T. Sowers, B.L. Ward, H. Ade, R.F. Davis, "Imaging Electron Emission from Diamond and III-V Nitride Surfaces with Photo-Electron Emission Microscopy", *Appl. Surf. Sci.* 146 (1999): 287-294.
- [59] F.A.M. Koeck, J.M. Garguilo, R.J. Nemanich, S. Gupta, B.R. Weiner, G. Morell, "Spatial Distribution of Electron Emission Sites for Sulfur Doped and Intrinsic Nanocrystalline Diamond Films", *Diam. Relat. Mater.* 12 (2003): 474-480.
- [60] S. Kono, T. Saito, S.H. Kang, W.Y. Jung, B.Y. Kim, H. Kawata, T. Goto, Y. Kakefuda, H.W. Yeom, "Band Diagram for Chemical Vapor Deposition Diamond

Surface Conductive Layer: Presence of Downward Band Bending Due to Shallow Acceptors", *Surf. Sci.* 604 (2010): 1148-1165.

[61] J.B. Cui, J. Ristein, M. Stammler, K. Janischowsky, G. Kleber, L. Ley, "Hydrogen Termination and Electron Emission from CVD Diamond Surfaces: A Combined Secondary Electron Emission, Photoelectron Emission Microscopy, Photoelectron Yield, and Field Emission Study", *Diam. Relat. Mater.* 9 (2000): 1143-1147.

[62] D. Takeuchi, C.E. Nebel, S. Yamasaki, "Photoelectron Emission from Diamond", *Phys. Stat. Sol. (a)* 203 (2006): 3100-3106.

[63] A.Y. Sakharava, Y.V. Pleska, F. Di Quarto, S. Piazza, C. Sunseri, I.G. Teremetskaya, V.P. Varnin, "Synthetic Diamond Electrodes: Photoelectrochemical Investigation of Undoped and Boron-Doped Polycrystalline Thin Films", *J. Electrochem. Soc.* 142 (1995): 2704.

[64] B.M. Nichols, J.E. Butler, J.N. Russell, Jr., R.J. Hamers, "Photochemical Functionalization of Hydrogen-Terminated Diamond Surfaces: A Structural and Mechanistic Study", *J. Phys. Chem. B* 109 (2005): 20938-20947.

[65] D. Zhu, L. Zhang, R.E. Ruther, R.J. Hamers, "Photo-Illuminated Diamond as a Solid-State Source of Solvated Electrons in Water for Nitrogen Reduction", *Nat. Mater.* 12 (2013): 836-841.

[66] A.B. Couto, L.C.D. Santos, J.T. Matsushima, M.R. Baldan, N.G. Ferreira, "Hydrogen and Oxygen Plasma Enhancement in the Cu Electrodeposition and Consolidation Processes on BDD Electrode Applied to Nitrate Reduction", *Appl. Surf. Sci.* 257 (2011): 10141-10146.

[67] J.D. Rameau, J. Smedley, E.M. Muller, T.E. Kidd, P.D. Johnson, "Properties of Hydrogen Terminated Diamond as a Photocathode", *Phys. Rev. Lett.* 106 (2011): 137602

[68] M. Niigaki, S. Uchiyama, H. Kan. Polycrystal Diamond Thin Film and Photocathode And Electron Tube Using the Same. US patent 7045957, filed Aug 20, 2002, and issued May 16, 2006.

[69] T.L. Westover, A.D. Franklin, B.A. Cola, T.S. Fisher, R.G. Reifenberger, "Photo- and Thermionic Emission from Potassium-Intercalated Carbon Nanotube Arrays", *J. Vac. Sci. Technol. B* 28 (2010): 423-434.

[70] P. Yaghoobi, M.V. Moghaddam, A. Nojeh, "'Heat Trap': Light-Induced Localized Heating and Thermionic Electron Emission from Carbon Nanotube Arrays", *Solid State Commun.* 151 (2011): 1105-1108.

[71] M.V. Moghaddam, P. Yaghoobi, A. Nojeh, "Polarization-Dependent Light-Induced Thermionic Electron Emission from Carbon Nanotube Arrays Using a Wide Range of Wavelengths", *Appl. Phys. Lett.* 101 (2012): 253110.

- [72] P. Yaghoobi, M.V. Moghaddam, A. Nojeh, "Solar Electron Source and Thermionic Solar Cell", *AIP Adv.* 2 (2012): 042139.
- [73] P.T. McCarthy, S.J. Vander Laan, D.B. Janes, T.S. Fisher, "Photonicallly Excited Electron Emission from Modified Graphitic Nanopetal Arrays", *J. Appl. Phys.* 113 (2013): 193710.
- [74] G.P. Smestad, "Conversion of Heat and Light Simultaneously Using a Vacuum Photodiode and the Thermionic and Photoelectric Effects", *Sol. Energ. Mat..Sol. C.* 82 (2004): 227-240.
- [75] J.W. Schwede, I. Bargatin, D.C. Riley, B.E. Hardin, S.J. Rosenthal, Y. Sun, F. Schmitt, P. Pianetta, R.T. Howe, Z.X. Shen, N.A. Melosh: "Photon-Enhanced Thermionic Emission for Solar Concentrator Systems", *Nat. Mater.* 9 (2010): 762-767.
- [76] S. Su, H. Zhang, X. Chen, J. Kang, J. Chen, "Parametric Optimum Design of a Photon-Enhanced Thermionic Solar Cell", *Sol. Energ. Mat. Sol. C.* 117 (2013): 219-224.
- [77] A. Asgari, K. Khalili, "Temperature Dependence of Ingan/Gan Multiple Quantum Well Based High Efficiency Solar Cell", *Sol. Energ. Mat. Sol. C.* 95 (2011): 3124-3129.
- [78] A. Varpula, M. Prunnila, "Diffusion-Emission Theory of Photon Enhanced Thermionic Emission Solar Energy Harvesters", *J. Appl. Phys.* 112 (2012): 044506.
- [79] G. Segev, Y. Rosenwaks, A. Kribus, "Loss Mechanisms and Back Surface Field Effect in Photon Enhanced Thermionic Emission Converters", *J. Appl. Phys.* 114 (2013): 044505.
- [80] K. Sahasrabuddhe, J.W. Schwede, I. Bargatin, J. Jean, R.T. Howe, Z.-X. Shen, N.A. Melosh, "A Model for Emission Yield from Planar Photocathodes Based on Photon-Enhanced Thermionic Emission or Negative-Electron-Affinity Photoemission", *J. Appl. Phys.* 112 (2012): 094907.
- [81] Y. Yang, W. Yang, W. Tang, C. Sun, "High-Temperature Solar Cell for Concentrated Solar-Power Hybrid Systems", *Appl. Phys. Lett.* 103 (2013): 083902.
- [82] T. Ito, M.A. Cappelli, "Optically Pumped Cesium Plasma Neutralization of Space Charge in Photon-Enhanced Thermionic Energy Converters", *Appl. Phys. Lett.* 101 (2012): 213901.
- [83] G. Segev, A. Kribus, Y. Rosenwaks, "High Performance Isothermal Photo-Thermionic Solar Converters", *Sol. Energ. Mat. Sol. C.* 113 (2013): 114-123.
- [84] J.W. Schwede, T. Sarmiento, V.K. Narasimhan, S.J. Rosenthal, D.C. Riley, F. Schmitt, I. Bargatin, K. Sahasrabuddhe, R.T. Howe, J.S. Harris, N.A. Melosh, Z.-X. Shen, "Photon-Enhanced Thermionic Emission from Heterostructures with Low Interface Recombination", *Nat. Commun.* 4 (2013): 1576.

CHAPTER 2

INSTRUMENTS AND ANALYSIS METHOD

2.1 Introduction

Experiments in this thesis have mainly been accomplished *in situ* with an integrated ultra-high vacuum (UHV) system, with the addition of other *ex-situ* facilities and equipment. This integrated UHV system is a linear UHV transfer line chamber that connects different processing and characterization chambers, which is shown in Fig. 2.1. The UHV transfer line is operated at a base pressure of $\sim 5 \times 10^{-10}$ Torr which is maintained with five cryogenic pumps. The samples are loaded into the transfer line through a loadlock, and then transported to each chamber for processing and analysis. The following systems are employed throughout this research: reactive molecular electron beam deposition system (MBD) for metal oxide deposition; remote hydrogen plasma (H-plasma) system for hydrogen termination; remote oxygen plasma enhanced atomic layer deposition system (PEALD) which serves as a remote oxygen plasma chamber for cleaning and oxygen termination of the diamond surfaces; electron beam evaporation (E-beam) system for metal deposition; X-ray photoelectron spectroscopy (XPS) for core level analysis; and finally ultraviolet photoelectron spectroscopy (UPS), which is the most frequently used instrument in this research, for both valence band analysis and collection of the low energy photo- and thermionic emission electron spectra.

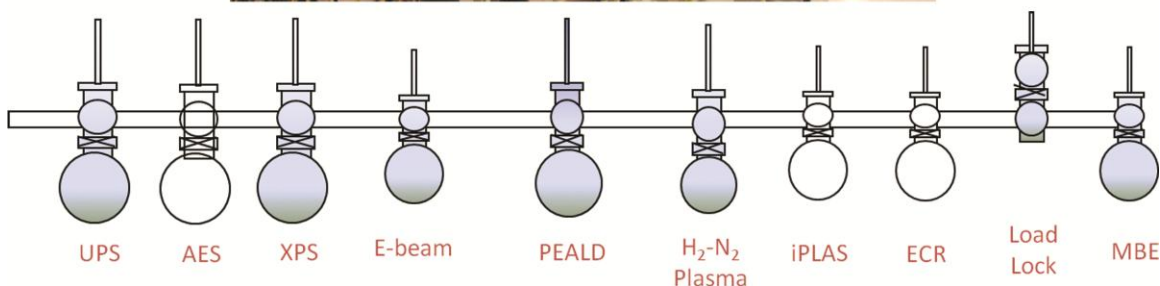
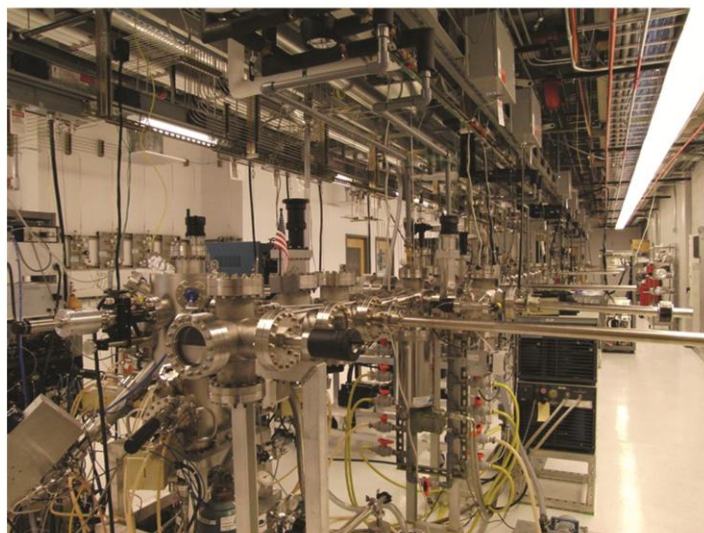


Fig. 2.1 Actual view and schematic illustration of the transfer line with integrated UHV systems.

Other facilities and equipment employed during this research include: two microwave plasma enhanced chemical vapor deposition (MPCVD) systems for deposition of nitrogen- and phosphorus-doped diamond films; a chemical room for cleaning the diamond samples with sulfuric acid, de-ionized water and ultra-high purity (UHP) nitrogen gas; a prototype Elmitec LEEM III instrument for photoemission electron and thermionic emission electron microscopy (PEEM / TheEM) imaging; a JEOL ARM200F aberration corrected scanning transmission electron microscope (STEM) for examination of the diamond-substrate interface; and a Perkin-Elmer Lambda 18 UV-Vis spectrometer for optical absorbance measurements.

2.2 Principle of Photoemission Electron Spectroscopy

Two main photoemission electron spectroscopy systems, X-ray photoelectron spectroscopy (XPS) and ultraviolet photoelectron spectroscopy (UPS), have been employed in this research. A photoelectron spectroscopy system is composed of: a photon source, an electron analyzer with associated lens stack, an electron detector/multiplier and a sample manipulator, all of which are assembled into an UHV chamber. The photoelectron emission mechanism has been described by Spicer [1] to be a three-step process. Photon illumination is provided by the specific X-ray or UV light source and delivered to the sample surface. Upon striking the surface the photons excite electrons inside the sample by using the photon energy to excite an electron into an elevated energy state. The electrons then transport to the sample surface, and are emitted into vacuum if their energy is sufficient enough to overcome the surface energy barrier. The emitted electrons are collected and dispersed by an electron spectrometer, which records the intensity of electrons as a function of their kinetic energy. The photoemission process is illustrated in Fig. 2.2. Most of the electrons excited deep inside the sample are not emitted due to losses from scattering and recombination, and only those electrons excited near the sample surface will have the ability to escape and contribute to the emission spectrum. The mean distance is defined as the sampling depth. Fig. 2.3 shows the relationship between the average electron escape depth and its kinetic energy. Some scattered electrons still have enough energy to overcome the surface barrier, and they can be also emitted as secondary electron that forms a background signal in the spectrum, with increasing intensity towards the low energy threshold. Because the scattering

changes their energy and momentum, these electrons cannot be directly related to the valence band electronic states.

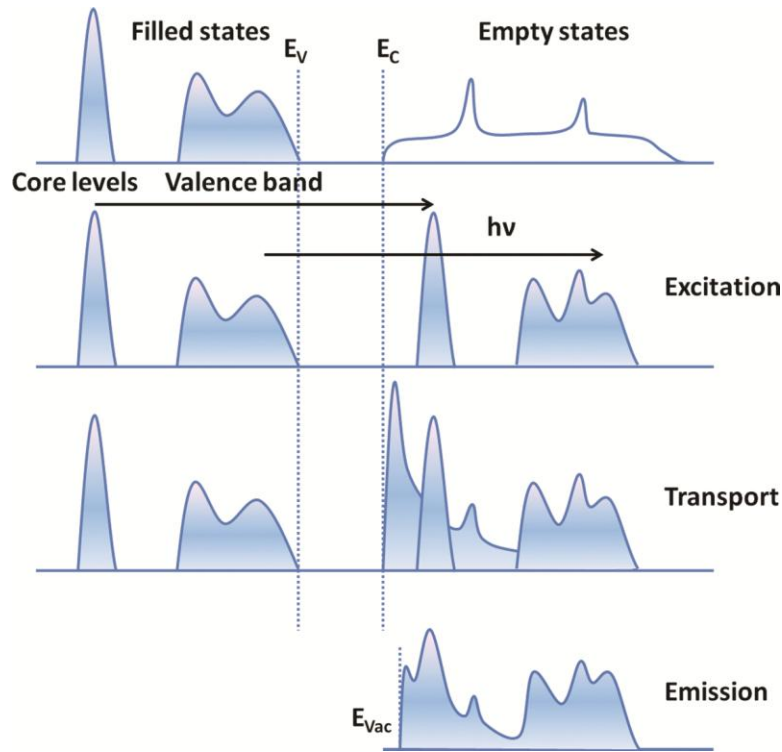


Fig. 2.2 Diagrams illustrating the three-step model of photoemission. Electrons are excited from filled states into empty, conduction band states. Some electrons are affected by inelastic collisions as they propagate to the surface, which adds a secondary electron background to the distribution. Electrons with sufficient energy to overcome the work function of the surface are emitted in the third step. The distribution of excited electrons reflects features of the density of states.

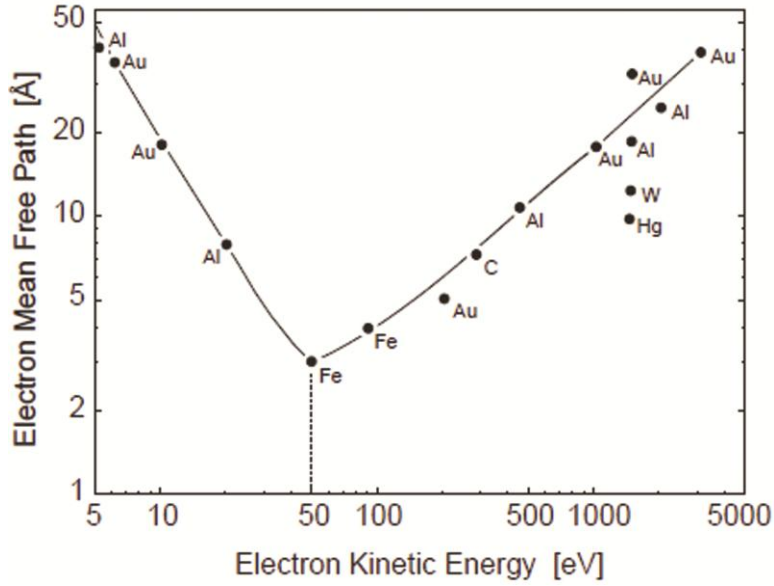


Fig. 2.3 The “universal curve” of electron mean free path of various metals as a function of kinetic energy [2].

For the emitted electrons that are unscattered in the emission process, their kinetic energy can be related to the energy level in the solid material. Quantitatively, the relationship between the binding energy of an electron in the solid and its emitted kinetic energy is given as:

$$BE = h\nu - KE - \Phi_w, \quad (2.1)$$

where BE represents the electron binding energy, $h\nu$ is the photon energy, KE is the kinetic energy after excitation, and Φ_w is the work function of the sample. Eq. 2.1 is well known as the photoelectric effect. The detected kinetic energy, however, is typically referred to the vacuum level of the spectrometer, and the above equation is rewritten as:

$$BE = h\nu - KE - \Phi_A + q \cdot V, \quad (2.2)$$

where Φ_A is the work function of the spectrometer, q is the elementary charge and V is the bias that may be applied between the sample and the electron analyzer. This bias

accelerates the electrons, providing them sufficient energy to overcome Φ_A , and consequently maximize the collection of low energy electrons. This is particularly important for the UPS system which is used to detect thermionic emission and visible light photoemission. Following Eq. 2.2, the measured kinetic energy of one electron can be converted back to its binding energy in the sample before excitation. This binding energy is referred to the Fermi level (E_F), which is typically defined as the zero point of binding energy.

Additionally, angle-resolved photoelectron spectroscopy (ARPES) can be employed to provide information on both the energy and momentum of an electron, by measuring the electron spectrum as a function of emission angle. In ARPES analysis, the photon momentum is often negligible compared with electron momentum, leading to conservation of the electron momentum in the plane of the sample:

$$k_{\parallel} = \sqrt{\frac{2m}{\hbar^2} \cdot KE} \sin \theta = \sqrt{\frac{2m}{\hbar^2} [h\nu - BE - \Phi_w]} \sin \theta, \quad (2.3)$$

where θ is the angle of the outgoing electron from the surface normal. The normal component may not be conserved. By assuming a free-electron model, it is given as:

$$k_{\perp} = \sqrt{\frac{2m}{\hbar^2} [h\nu - \Phi_w - BE + V_0] - k_{\parallel}^2}, \quad (2.4)$$

where V_0 is the so called "inner potential" that can be determined from the periodicity and symmetry of the measured dispersion $E(k)$. The results can be used to describe the band structure in the k -space. The UPS system is preferred for ARPES measurements, due to the much smaller wave vector of UV photons than X-ray photons.

2.3 Hemispherical Electron Analyzer for UV Photoemission and Low Energy Emission Spectroscopy

The specific kinetic energy of the photo-emitted electrons is filtered with a hemispherical electron analyzer, shown in Fig. 2.4. In our system the analyzer is mounted on a two-motion goniometer, allowing it to be turned 360° in the horizontal plane, and 10° above and 90° below the plane, with the sample position at the pivot point. For single crystal samples, this configuration allows angle-resolved photoelectron spectroscopy (ARPES) analysis where the emission angle is used to determine the k -vector or crystal momentum of the original electron state. During experiments in this research, however, a fixed position of the analyzer is maintained in front of the sample stage, so that electron emission is collected along the normal direction to the sample surface.

The analyzer consists of two concentric hemispherical plates, between which a bias voltage is applied. Electrons emitted from the sample are focused through a lens stack and enter the space between the two plates through a 1 mm slit. In order to measure electrons with a large range of kinetic energy, the electron energy is changed by an accelerating field in the lens stack into a desired narrow range, the center of which is the mean analyzing energy, or pass energy, E_0 . As electrons pass between the plates they are deflected by the electric field into curved trajectories. Electrons outside of the selected energy range will be deflected into one of the two plates. Additionally only electrons with appropriate energy emitted within a 2° entrance angle will be deflected a full 180° in the spectrometer. These electrons then exit the analyzer through another 1 mm slit, and enter a Channeltron single channel electron multiplier, where they are converted into charge pulses for further analysis.

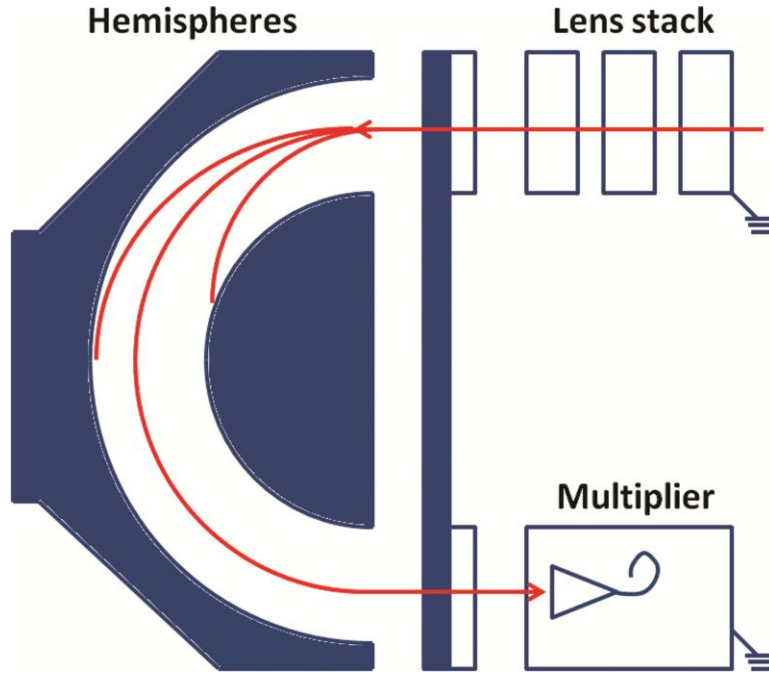


Fig. 2.4 Schematic of the hemispherical electron analyzer in the UPS system.

During UPS measurements in this research, a constant bias was applied between the plates, allowing only electrons within a certain narrow range of kinetic energies to pass. Thus the retarding voltage is changed for electrons with different kinetic energies, and this mode is named "FAT" (fixed analyzer transmission). This ensures a constant energy resolution, ΔE , of the hemispherical analyzer on the UPS system, which is given by [3]:

$$\frac{\Delta E}{E_0} = \frac{d}{2R_0} + \frac{\alpha^2}{4}, \quad (2.5)$$

Where E_0 is the energy of the electrons that pass through the analyzer, d the slit width (1 mm), R_0 the radius of the analyzer (50 mm), and α the acceptance angle (~ 0.02 radians). From an approximate calculation of Eq. (2.5), the energy resolution of this analyzer is $\sim 1\%$ of the pass energy. Lowering the pass energy will therefore increase the energy resolution of the analyzer, but decrease the yield.

2.4 X-ray Photoelectron Spectroscopy

One of the major differences between XPS and UPS is the photon energy of the different light sources, and consequently the different binding energy regimes of the excited electrons. In this research, the XPS system employ a VG XR3E2 dual anode source installed with Mg and Al sources. A hot filament emits thermionic electrons, which are then accelerated and strike onto the specific metal anode to generate X-ray photons. The main photon energies from these two sources are Mg $K\alpha_1$ (1253.6 eV) and Al $K\alpha_1$ (1486.6 eV). These high energy X-ray photons can generate electrons from core levels of the atoms in the sample, with a sampling depth of 5-10 nm into the surface. A VG microtech Clam II analyzer operated at a resolution of 1.0 eV collects the emitted electrons. The spectrometer records the number of electrons by their kinetic energies, typically in the range of 0 ~ 1 keV.

2.5 Ultraviolet Photoelectron Spectroscopy

Different from the XPS system, UPS typically employs ultraviolet light generated by a gas plasma discharge as the photon source. Noble gases like helium and argon frequently serve as this discharge gas. The UPS system in this research employs research grade purity (99.9999%) helium and UHP purity (99.9995%) argon for a discharge lamp. The gas delivery system includes the corresponding gas bottles and regulators, a Varian precision leak valve that delivers the gas into the lamp, and two turbo-pumps connected to the lamp in a differential pumping configuration to maintain the lamp pressure. Two of the strongest lines can be excited in the He discharge, including He I with a photon energy of 21.22 eV and He II with a photon energy of 40.82 eV. For the Ar discharge,

spectra are acquired using Ar I that has a photon energy of 11.83 eV. The ratio between the intensities of these two lines can be tuned by changing the gas pressure in the discharge lamp. When the discharge lamp is operated for the He I line, the discharge lamp shows an orange color from the quartz tube; if the He discharge lamp is operated for the He II line, the lamp has a dim lilac (light purple) color. The different colors of the discharge lamp with He I and He II are shown in Fig. 2.5 (a) and (b) respectively. Measuring the electron spectrum with He II excitation generally requires higher pass energy and lower resolution due to its weak intensity.

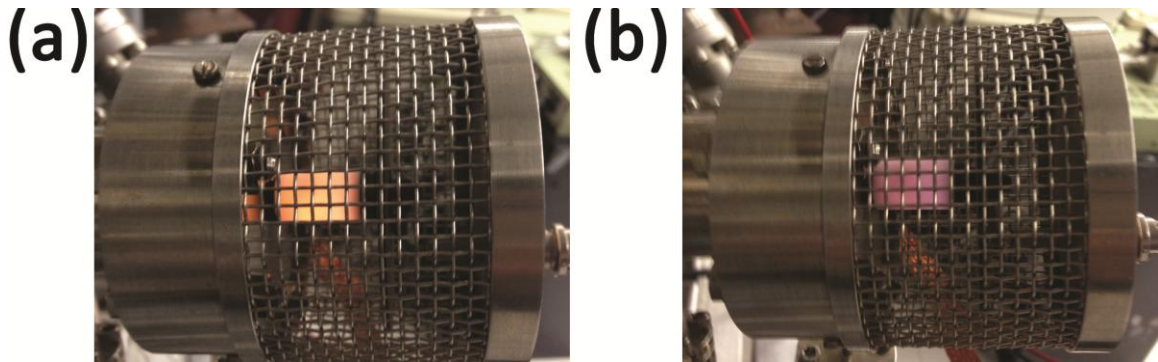


Fig. 2.5 Actual views of the discharge lamp when (a) He I and (b) He II lines are tuned for spectroscopy measurements.

Due to its lower photon energy, UV light photons (He I and II) excite the electrons in the valence band of the sample, and the corresponding sampling depth is typically less than 1 nm from the surface. In the system used in this research, the UV photoelectron spectra are recorded by a VSW HA50 hemispherical electron analyzer controlled by a VSW HAC300 lens controller. The analyzer can be operated at a resolution between ~ 20 to 500 meV by selecting the specific pass energy, while the 15 eV pass energy is most frequently used for a balance between spectral intensity and

signal-to-noise ratio. The spectrometer records the number of electrons according to their kinetic energies in a range between 0 and 50 eV.

Fig. 2.6 shows a schematic of the UPS chamber. The sample stage contains a tungsten irradiative heater coil beneath the sample holder. The temperature of the sample is controlled by a thermocouple positioned at the center of the coil, and calibrated by a Mikron M90Q infrared pyrometer.

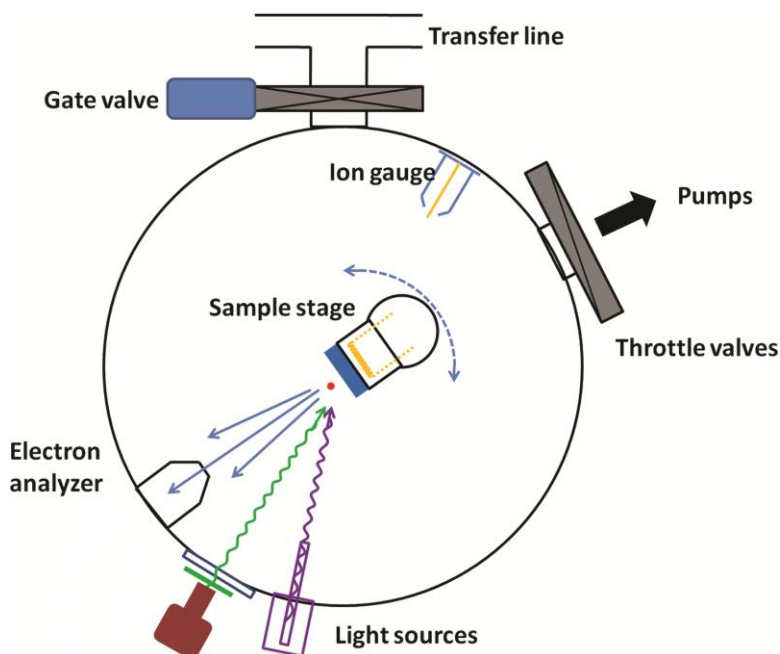


Fig. 2.6 Schematic of the UPS chamber, showing relative positions of the sample stage with heater, the light sources and the electron analyzer.

2.6 Calibration of XPS and UPS

The XPS and UPS spectra are commonly presented as plots of the electron intensity (counts per second) vs. binding energy. To convert the electron kinetic energy into the binding energy by employing Eq. 2.2, it is necessary to calibrate the electron analyzer. For calibration purposes, obtaining the spectrum from a standard sample is

required, which is usually a clean metal surface without oxidation. This is due to the fact that an insulating oxide layer can result in a shift of the whole spectra to higher binding energy. The standard sample can be prepared either by *in-situ* deposition and characterization without air exposure, or by employing noble metal samples, such as Au, Pt or Ag, due to their inherent resistance to oxidation.

There are two common ways to determine the work function of the analyzer. One is to measure the core level peak position of a certain element, and refer such position to a known value. The other way is to determine relative position of E_F in the spectrum, and define this value as the zero in the binding energy scale. The first method is typically employed for XPS calibration. This is due to the relatively weak signal of the XPS spectrum near E_F . For UPS calibration the second method is preferred, as some metals (e.g. nickel) exhibit a significant cut-off edge at E_F in the UV photoelectron spectra, which could be used to determine the binding energy reference.

An XPS calibration scan of a standard Au foil is shown in Fig. 2.7. The XPS was calibrated to align the Au $4f_{7/2}$ peak to 84.0 eV [4] by measuring a standard gold foil. While the analyzer operates at a resolution of 1.0 eV, the peak positions can be further resolved by curve fittings at a resolution of 0.1 eV.

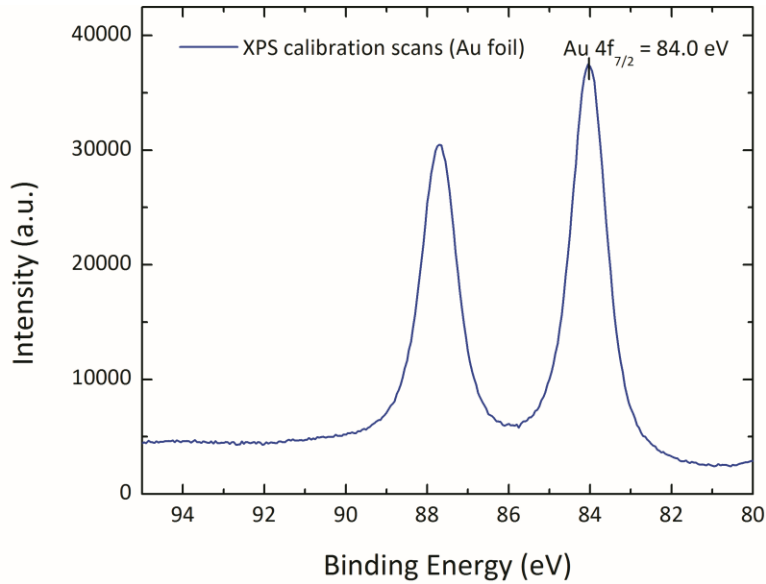


Fig. 2.7 XPS scan of a standard Au foil, showing the 4f peaks that are used for XPS calibration.

Fig. 2.8 shows a UPS calibration scan of an Au film, which is deposited by e-beam evaporation. The He I line (21.2 eV) is employed with a 6V bias applied between to the sample and the analyzer. The front cut-off of the UPS spectrum indicates E_F of a metal sample or the valence band maximum (VBM) of a semiconductor sample. The back cut-off of the UPS spectrum is equivalent to the minimum energy required to overcome the surface barrier, which is typically the work function of the sample. The x-axis of Fig. 2.8 represents the electron kinetic energy. The front cut-off is found at 22.8 eV, meaning that the excited electrons at E_F have a kinetic energy of 22.8 eV relative to the vacuum level in the analyzer. According to Eq. 2.2, by substituting $h\nu = 21.2$ eV, $KE = 22.8$ eV, $qV = 6$ eV, and by definition $BE = 0.0$ eV for the metal, the work function of the analyzer, Φ_A , is calibrated to be 4.4 eV. Additionally, the back cut-off is at 6.1 eV, which corresponds to a binding energy of 16.7 eV, and hence the work function Φ_W of this Au film is 4.5 eV by applying Eq. 2.1 with $KE = 0$ eV. According to Ref. [5], single

crystal Au has a work function of $\sim 5.3\text{-}5.5$ eV. The difference may be resulted from different sample preparation methods.

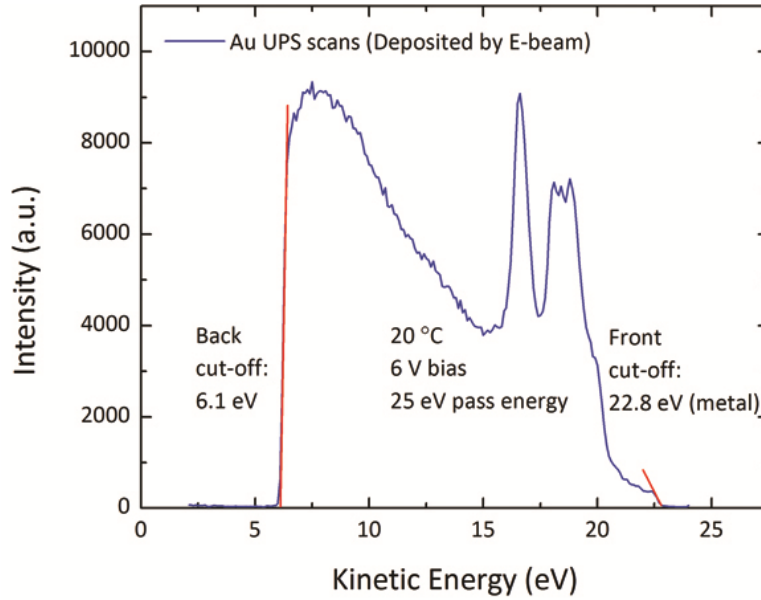


Fig. 2.8 UPS scan of a thin Au film deposited by e-beam evaporation, with the characteristic peaks of Au in the valence band. The high energy cut-off at 22.8 eV kinetic energy is referred to E_F for UPS calibration.

2.7 Xenon Arc Lamp

As the UPS system is preferred for measurement of electrons with relatively low kinetic energy (0-50 eV), it is also suitable for measurements of the thermionic electron spectrum and visible light induced photoelectron spectrum from low work function materials. In this research, this feature is frequently employed to study the diamond-based electron emitters. The thermionic electron spectrum can be straightforwardly attained by heating the sample to specific temperatures and collecting the emitted electrons. For photo-induced electron emission with sub-bandgap photons, a different light source than

the UV discharge lamp is required. In this research, an illumination system has been constructed, based on an Oriel 6257 100W ozone free xenon arc lamp.

A xenon arc lamp is a gas discharge lamp, which generates photons through ionized xenon gas at a high pressure. The light from the xenon lamp is generated by an electrically induced plasma discharge, which is formed through ionization of the Xe gas in the small gap between the anode and cathode. The xenon arc lamp employed in this research has an effective arc size of $0.4 \times 0.8 \text{ mm}^2$, operates with the anode at the top and the cathode at the bottom. Controlled by an Oriel 68806 power supply unit, this lamp is operated at a voltage of 14 V and a current of 6.7 A, and has an approximate flux of 1800 Lumens. Most of the strongest persistent lines of the Xe I spectrum are in the infrared range (823, 828, 882 nm, etc.) [6]. As a result, the xenon arc lamp creates a relatively flat spectrum over the visible to UV light regime, which can be employed to simulate the sunlight. Due to the fact that ultraviolet radiation below 242 nm produces toxic ozone, this lamp has a UV blocking coating on the envelope, hence UV components below 300 nm has significantly reduced intensity. Because of the small size of the discharge, the lamp is positioned at the center of an air-cooled Oriel 60010 arc lamp housing frame, with a rear reflector and an adjustable condensing lens assembly to maximize the output intensity.

To select the desired wavelength from the continuous xenon lamp spectrum, a series of band pass filters are employed in this research. These filters have a diameter of 25.4 mm, and the transmitted light has a full width at half max (FWHM) of $10 \pm 2 \text{ nm}$ and a minimum peak transmission of 20-30%. The filters can be attached onto the focusing lens of the lamp housing using a filter holder. Fig. 2.9 shows the optical power of the

focused light from the filtered Xe arc lamp, recorded with a Newport 1916-C optical power meter.

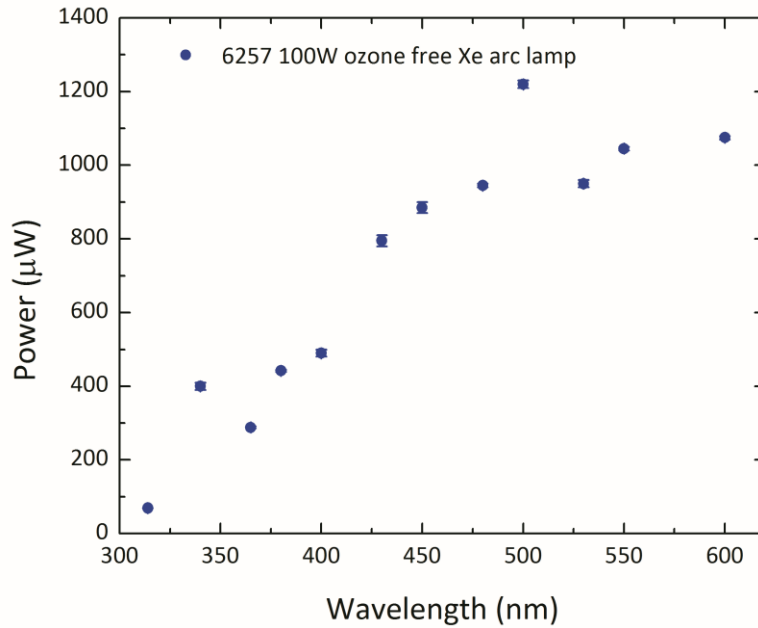


Fig. 2.9 Output power of the xenon arc lamp system with associated filters, measured by an optical power meter.

In order to examine the effectiveness of the Xe lamp system as a light source for visible light photoemission, a thin film of dysprosium was deposited using e-beam evaporation onto a molybdenum substrate for photoelectron spectroscopy demonstration. The results shown in Fig. 2.10 display strong emissivity from the Dy sample at ambient temperature. According to the spectra generated with photons of different wavelengths, this Dy film shows a constant work function of ~ 2.0 eV. Additionally, the maximum kinetic energy in each spectrum approximately equals the corresponding photon energy, indicating that the highest energy electrons are generated near E_F , as expected from photoemission theory of metals.

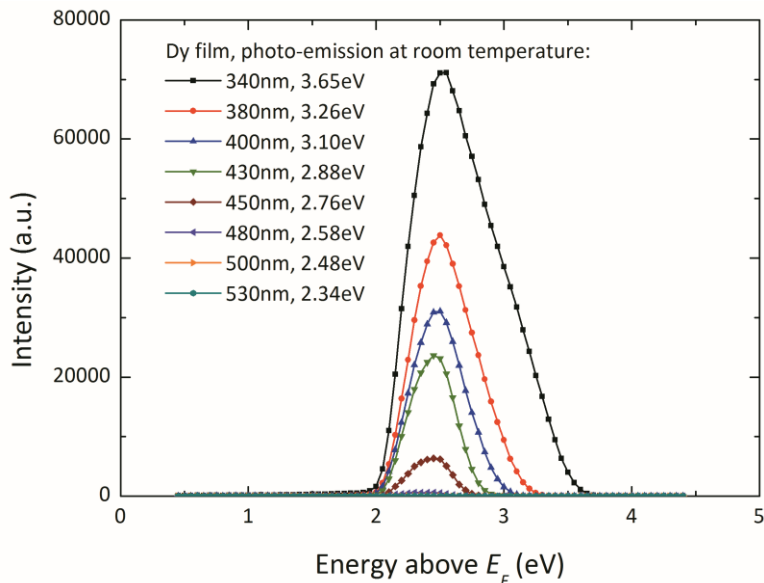


Fig. 2.10 Photoelectron spectra of a Dy film under illumination from the Xe arc lamp with different bandpass filters. Signals can be observed with illuminating wavelength up to 500 nm.

References

- [1] W.E. Spicer, "Photoemissive, Photoconductive, and Optical Absorption Studies of Alkali-Antimony Compounds", *Phys. Rev.* 112 (1958): 114-122.
- [2] S. Hüfner, S. Schmidt, F. Reinert, "Photoelectron Spectroscopy - an Overview", *Nucl. Instrum. Meth. A* 547 (2005): 8-23.
- [3] D. Briggs, *Handbook of X-ray and ultraviolet photoelectron spectroscopy* (Heyden, 1977).
- [4] J.F. Moulder, W.F. Stickle, P.E. Sobol, K.D. Bomben, *Handbook of X-ray photoelectron spectroscopy* (Waltham: Perkin-Elmer Corporation, 1992).
- [5] W.M. Haynes, *CRC Handbook of Chemistry and Physics, 94th edition* (Boca Raton: CRC Press, 2013-2014).
- [6] C. J. Humphreys, E. Paul, Jr., "Interferometric Wavelength Determinations in the First Spectrum of ^{136}Xe ", *J. Opt. Soc. Am.* 60 (1970): 1302.

CHAPTER 3

COMBINED VISIBLE LIGHT PHOTO-EMISSION AND LOW TEMPERATURE THERMIONIC EMISSION FROM NITROGEN DOPED DIAMOND FILMS

3.1 Abstract

This study reports a photoemission threshold of ~ 1.5 eV from nitrogen-doped nanocrystalline diamond, which ranks among the lowest photo-threshold of any non-cesiated material. Diamond films on molybdenum substrates have been illuminated with light from 340 to 550 nm, and the electron emission spectrum has been recorded from ambient to ~ 320 °C. The results display combined thermionic and photo-electron emission limited by the same low work function and indicate that the two emission processes are spatially separated. These results indicate the potential for a solar energy conversion structure that takes advantage of both photoemission and thermionic emission.

(In collaboration with Franz A.M. Koeck, Chiyu Zhu, and Robert J. Nemanich)

3.2 Introduction

Recently, nitrogen doped diamond films have shown low temperature thermionic emission and vacuum thermionic energy conversion at temperatures as low as 500 °C [1, 2], and these structures have been proposed for improving energy efficiency through reclamation of waste heat [3]. In this report we present results on visible light photoemission from *n*-type doped diamond films with one of the lowest photo threshold of any non-cesiated material. These emitters could enable a solar energy conversion structure that takes advantage of both photoemission and thermionic emission.

Due to the high electric and thermal conductivity, stability of diamond, and the negative electron affinity (NEA) of H-terminated diamond [4], it has been considered for electron emitter applications based on thermionic emission [1-3, 5, 6], field emission [7] and secondary electron emission [8]. On the other hand photoelectron emission has typically been limited by the large band gap and consequent large photo-threshold of diamond [9-12].

While *n*-type doping is essential to obtaining a low work function for diamond materials with a 5.45 eV band gap, upward band bending observed on single crystal surfaces has resulted in a work function > 3 eV [10, 13]. Yet, in previous studies, it has been shown that hydrogen terminated, *n*-type doped diamond films exhibit a low effective work function (defined here as the difference between the conduction band minimum (CBM) and the Fermi level, E_F), where a value of 1.3 eV has been achieved with nitrogen doping [1], and 0.9 eV with phosphorus doping [14]. The impact of band bending is presumably mitigated by the presence of the sp^2 bonded grain boundaries that can provide sufficient electrons to compensate empty surface states. In addition, the substrate and grain boundaries can provide carriers to sustain the emission current. Such values correspond to photon energies within the visible light regime. Thus the possibility of visible light photo-emission enabled with diamond film emitters is the focus of this report.

3.3 Experiment

This study employs nanocrystalline diamond (NCD) films grown by plasma enhanced chemical vapor deposition (PECVD), where a NEA surface is obtained by

cooling the sample in a hydrogen plasma. Through laser reflection interferometry (LRI) observation, the thickness of the diamond film is estimated to be between 500 nm to 1 μm . The electron emission spectrum during heating and illumination was obtained in our UV photoemission system using a 100W Xe arc lamp fitted with band pass filters. Electron spectra are recorded by a VSW-HA50 hemispherical analyzer operating at a resolution of 0.15 eV. For the studied wavelengths the photon illumination has a power density ranging from 0.4 to 1.2 mW/cm^2 , and the heating effect from the lamp is observed to be negligible. Heating of the sample is provided by a tungsten coil beneath the sample carrier, while temperature calibration is conducted through a Mikron M90Q infrared pyrometer. A 15V bias was applied between the analyzer and sample to maximize the collection of the low energy electrons, this electric field is orders of magnitude smaller than that typically required for field emission [7]. Bare molybdenum substrates served as control surfaces for the emission measurements. Under the same experimental conditions, neither thermionic nor photo-emission is observable from the bare molybdenum substrate, demonstrating that the electron emission involves the diamond film.

3.4 Results

Ambient temperature photoemission spectra from the diamond sample are shown in Fig. 3.1. The low energy cut-off at 1.5 eV is evidence of the effective work function, Φ_w . The normalized intensity of the electron peaks changes significantly with the specific photon energy, while the maximum emission energy relative to E_F corresponds approximately to the photon energy. The results indicate that the photo-electrons are

excited from states near E_F . The fact that the emission peaks do not match the excitation energy indicates that scattering processes influence the emission.

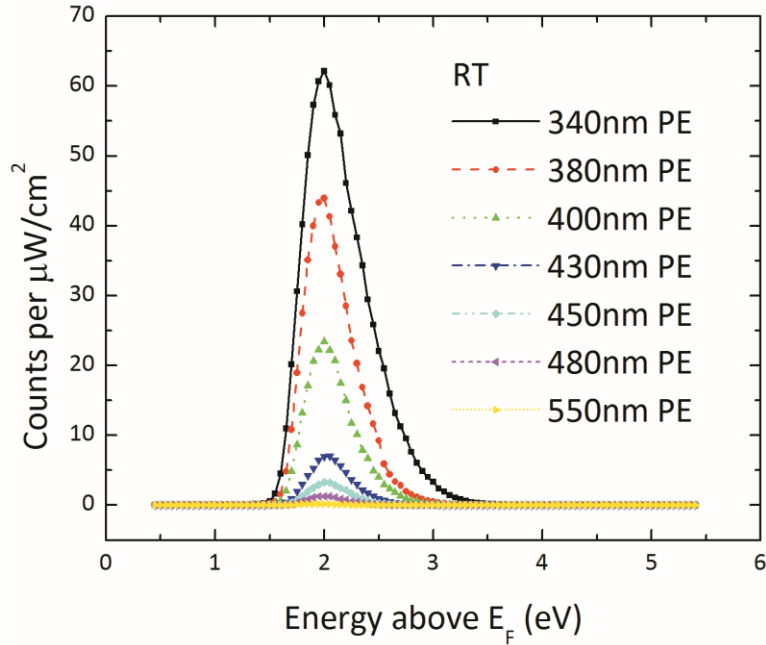


Fig. 3.1 Recorded emission spectra from N-doped diamond showing intensity normalized ambient temperature photo-emission.

The combined effects of thermionic emission and photon illumination were detected by measuring the electron emission spectra while the heated sample is illuminated. We assume that the thermionic emission is not affected by the illuminating photons. Thus, the PE component of each spectrum at a given temperature is obtained by subtracting the thermionic emission from the combined emission, as shown in Fig. 3.2. The thermionic and photo-emission spectra share the same low energy cut-off, Φ_w . The relationship between photo-emission and temperature then becomes of interest. The effect of temperature on both thermionic and photo-emission is shown in Fig. 3.3. Initially the thermionic emission is negligible but increases above ~ 220 °C. The PE initially increases slightly as the temperature is increased, but decreases at the

temperature where the thermionic emission becomes significant, possibly due to increased absorption by thermally excited free carriers in the diamond film. Such behavior indicates that although thermal ionization and photon excitation are spatially separate processes, there is a more complex interaction between them that needs to be considered.

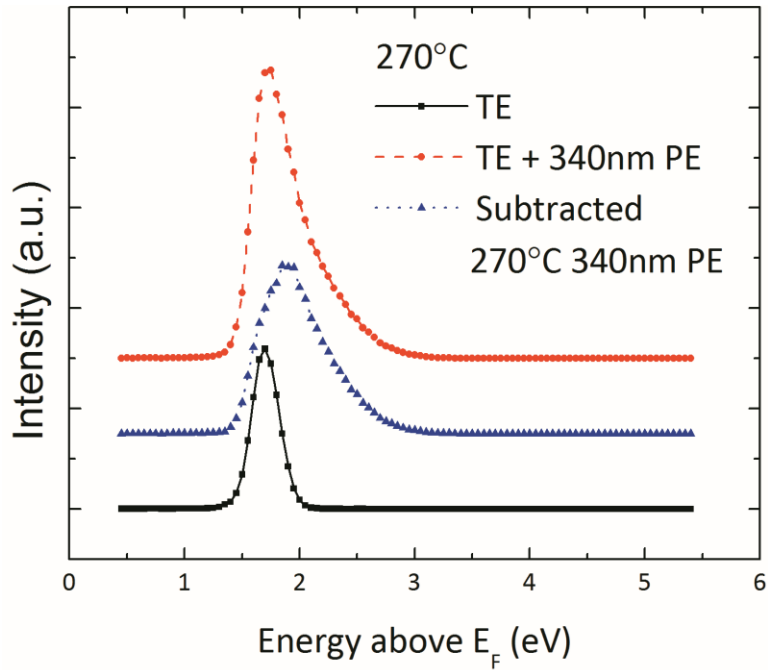


Fig. 3.2 The total emission, thermionic emission, and subtracted photo-emission component from a diamond sample at 270 °C and 340nm illumination.

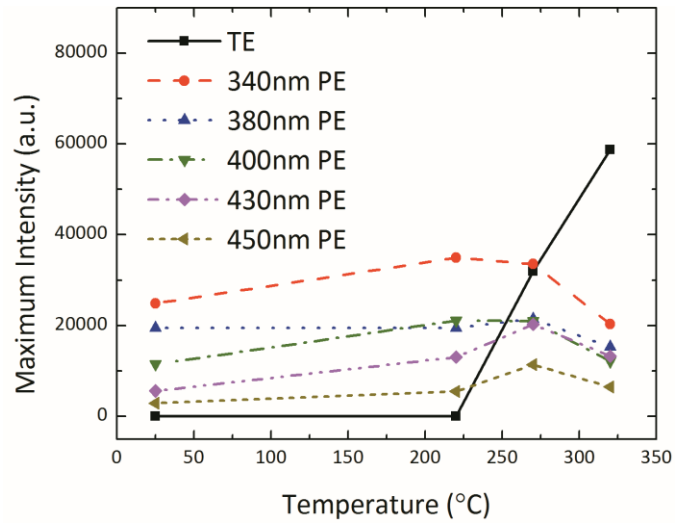


Fig. 3.3 The effect of temperature on thermionic and photo- emission. At low T the emission is dominated by the photo-excited carriers; at high T it is dominated by thermionic excitation.

In addition, preliminary results of photo- and thermionic emission spectra, collected from a phosphorus-doped diamond film, were also obtained, which are shown in Fig. 3.4. This sample exhibited strong emissivity similar to the nitrogen-doped diamond. The common low energy cut-off Φ_w was ~ 1.8 eV. Presumably, P-doped diamond will have a smaller effective work function as phosphorus is a shallower donor (0.6 eV) than nitrogen (1.7 eV). The observed work function can be resulted from a relatively small donor concentration, or upward band bending at the diamond surface.

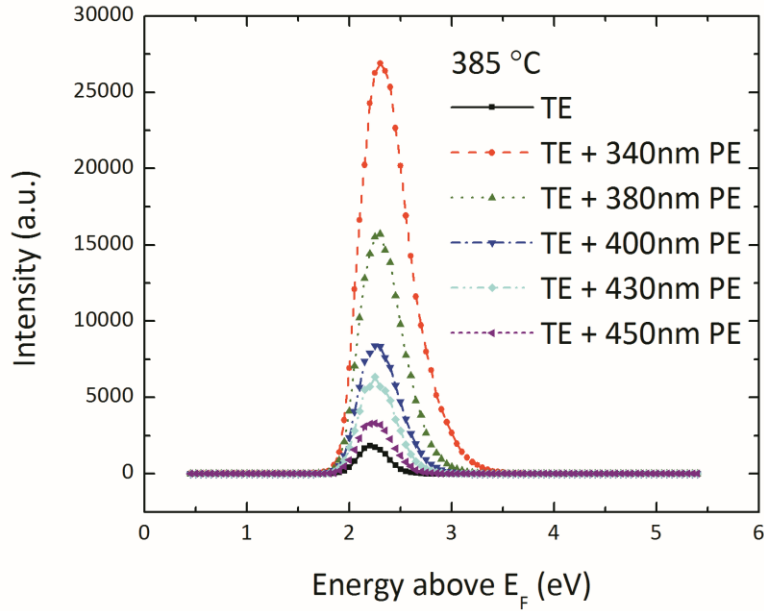


Fig. 3.4 Combined photo- and thermionic emission spectra from a P-doped diamond film at 385 °C.

The photocurrent generated by the visible light photoemission was measured by employing a Keithley 237 source measuring unit. The effective quantum efficiency (QE), which is defined as the ratio of the number of emitted electrons over the number of illuminating photons, can be determined with the photocurrent and the illuminating power density. The results collected from a nitrogen-doped diamond film are shown in Fig. 3.5, showing an approximately quadratic relationship between the QE and the photon energy. The low work function of the nitrogen-doped, hydrogen terminated diamond films appears to enable a higher QE than that of some metallic materials and a wider energy regime for photoelectron generation.

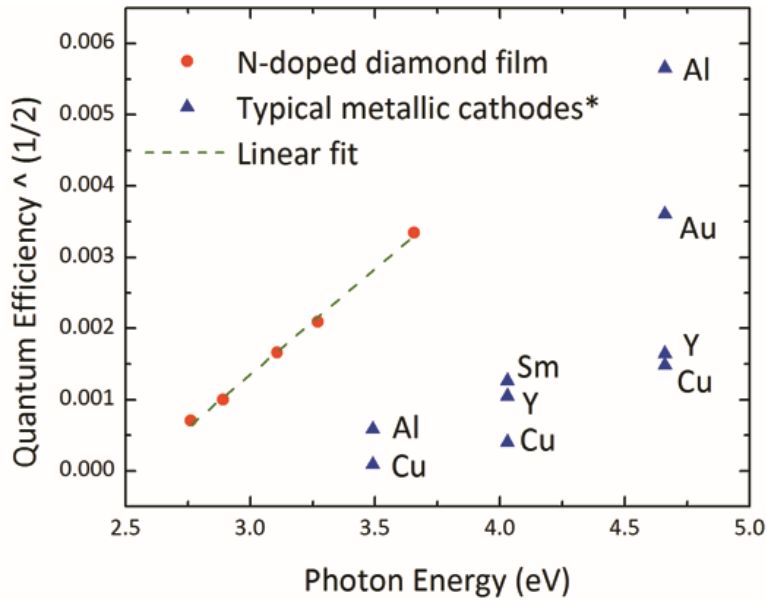


Fig. 3.5 The quantum efficiency of visible light photoemission from a nitrogen-doped diamond film, in comparison to some conventional metal photocathodes [15].

3.5 Discussion

The photo- and thermionic emission may be understood in terms of the 3-step process suggested by Spicer [16]: electrons are excited to states above the vacuum level, transported to the sample surface, and then emitted into vacuum. As shown in the band schematic in Fig. 3.6 (a), electrons in the conduction band originate from thermally ionized N-donors and form an equilibrium distribution; thus the thermionic emission originates from the surface of the diamond film. With illumination, the photons are transmitted through the diamond film and adsorbed in the metal substrate. The process is shown schematically in Fig. 3.6 (b). In this transport process the electrons “thermalize” into a non-equilibrium distribution through scattering. This process is similar to the results reported by Schwede et al. on doped GaN [17]. Therefore PE and TE are

individually interface or surface limited processes. Based on the observed spectra, the Schottky barrier at the metal-semiconductor interface does not provide an additional barrier that is greater than the surface work function of the diamond film.

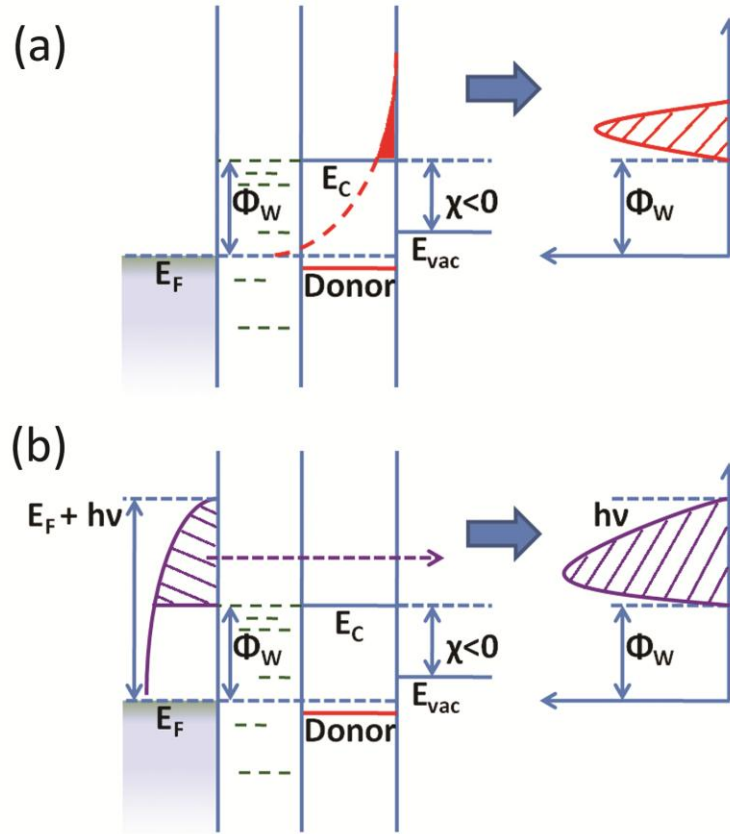


Fig. 3.6 Band schematics of the diamond emitter (including metal substrate, UNCD interface layer, and N-doped diamond) showing (a) thermionic and (b) photo-emission processes. Green dash lines represent the inter-bandgap states inside UNCD layer, introduced by sp^2 bonds.

Following the theoretical framework of free electron materials [18], a simplified and optimized model for analyzing the photoemission spectra assumes that the photon flux increases the energy of the electrons with equal probability. This effectively increases the Fermi-Dirac distribution of the metal substrate by the photon energy. The

electrons in the diamond conduction band are modeled as the product of the photon-enhanced distribution and the parabolic density of states of the diamond conduction band.

The electron emission distribution (EED) can be derived for photo-emission [19]:

$$I_{PE}(E)dE = A \frac{E - E_F - \Phi_W}{1 + \exp[E - E_F - h\nu/k_B T]} \times H(E - E_F - \Phi_W) dE, \quad (3.1)$$

where the constant A includes the effective mass and the collecting efficiency, and H is the Heaviside step function. The resulting spectrum is the convolution of the EED and a Gaussian spreading function characteristic of the analyzer with a resolution σ :

$$G_l = \frac{1}{\sigma\sqrt{2\pi}} \exp\left[-\frac{1}{2}\left(\frac{E - E'}{\sigma}\right)^2\right]. \quad (3.2)$$

The numerically calculated results are shown in Fig. 3.7, normalized to the actual spectra. A work function of 1.8 eV is used instead of the low energy cuts off, due to smearing from the convolution. Disagreement of modeled and experimental spectra is believed to be evidence of a strong “thermalizing” effect [19]. To include this effect, we assume all electrons are scattered by optical phonons (1332.5 cm^{-1} or 165 meV) with equal probability, hence the EED is then shifted to lower energy. For each scattered electron, its kinetic energy is reduced by the phonon energy, and the number of scattering events is assumed to follow a Poisson distribution with an expectation p :

$$\Delta I_{\text{mod, PE}}(E; E' \rightarrow E) dE = B(E') \cdot \frac{\exp(-p)}{\left[E' - E/E_{\text{phonon}} \right]!} \cdot p^{\lfloor E' - E/E_{\text{phonon}} \rfloor} \cdot I_{PE}(E') dE'. \quad (3.3)$$

Equation (3) shows the contribution to the modified EED at energy E from an equal or higher energy E' , and an integral of all these contributions represents the final EED. In the calculation, electron relaxation below the CBM is forbidden (modified through a probability-normalization coefficient B). At ambient temperature this model

provides a best correspondence with experimental data when p is equal to 8. Further improvement of the model would require consideration of the interaction between the photo- and thermionic emission and include the photon absorption as a function of sample temperature.

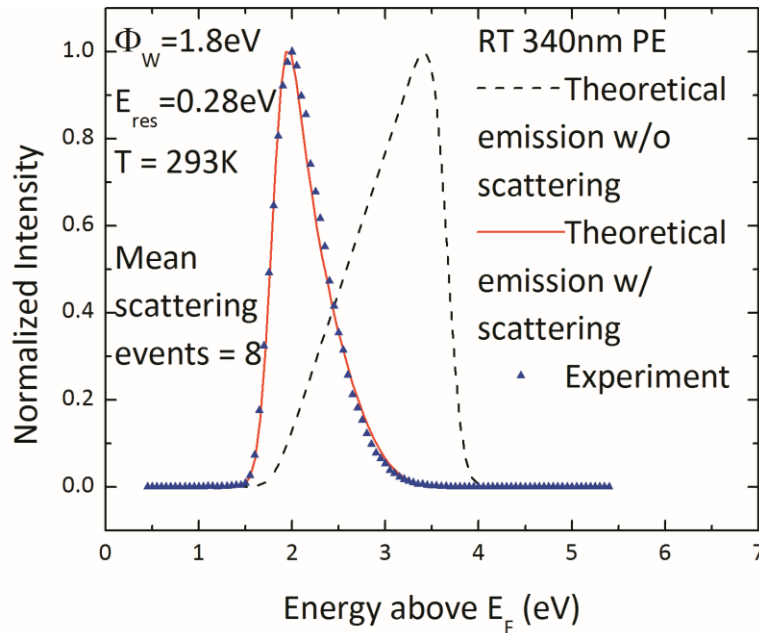


Fig. 3.7 Experimental and modeled emission spectra of the N-doped diamond film structure showing ambient temperature photo-emission with 340nm illumination.

3.6 Conclusion

To conclude, a mechanism is clearly established for electron emission from nitrogen-doped, hydrogen-terminated NCD emitters: the combined photo-emission and thermionic emission. As photo and thermal excitation are combined in this emissive process without the need of field enhancement, the NCD emitters are potentially candidates for applications in thermal and solar energy conversion. A schematic of such an energy converter is shown in Fig. 3.8. The quantum efficiency of the diamond photo-

emission still needs to be examined and will certainly be dependent on the properties of the substrate material. The efficiency of these integrated energy conversion devices may be further enhanced by including heavily phosphorus-doping [14] and molecular transport mechanisms [20].

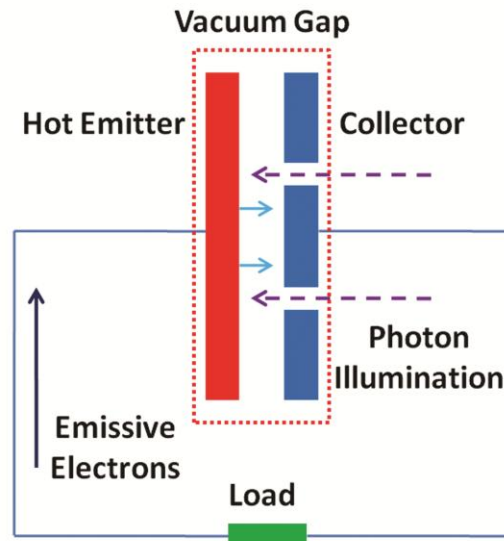


Fig. 3.8 Schematic of a diamond based energy converter. The emitter (doped diamond film) is heated for thermionic emission, and illuminating photons generate photo-emission.

References

- [1] F.A.M. Koeck, R.J. Nemanich, "Low Temperature Onset for Thermionic Emitters Based on Nitrogen Incorporated UNCD Films", *Diam. Relat. Mater.* 18 (2009): 232-234.
- [2] M. Kataoka, C. Zhu, F.A.M. Koeck, R.J. Nemanich, "Thermionic electron emission from nitrogen-doped homoepitaxial diamond", *Diam. Relat. Mater.* 19 (2010): 110-113.
- [3] Y.M. Wong, W.P. Kang, J.L. Davidson, S. Raina, J.H. Huang, "Carbon Nanostructures as Thermal Field Emitters for Waste Heat Recovery", *Diam. Relat. Mater.* 18 (2009): 563-566.

- [4] J. Van der Weide, Z. Zhang, P.K. Baumann, M.G. Wensell, J. Bernholc, R.J. Nemanich, "Negative-Electron-Affinity Effects on the Diamond (100) Surface", *Phys. Rev. B.* 50 (1994): 5803-5806.
- [5] M. Suzuki, T. Ono, N. Sakuma, T. Sakai. "Low-Temperature Thermionic Emission from Nitrogen-Doped Nanocrystalline Diamond Films on N-Type Si Grown by MPCVD", *Diam. Relat. Mater.* 18 (2009): 1274-1277.
- [6] K. Uppireddi, T.L. Westover, T.S. Fisher, B.R. Weiner, G. Morell, "Thermionic Emission Energy Distribution from Nanocrystalline Diamond Films for Direct Thermal-Electrical Energy Conversion Applications", *J. Appl. Phys.* 106 (2009): 043716.
- [7] O. Groning, L.O. Nilsson, P. Groning, L. Schlapbach, "Properties and Characterization of Chemical Vapor Deposition Diamond Field Emitters", *Solid State Electron.* 45 (2001): 929-944.
- [8] J.E. Yater, A. Shih, "Secondary Electron Emission Characteristics of Single-Crystal and Polycrystalline Diamond", *J. Appl. Phys.* 87 (2000): 8103-8112.
- [9] C. Bandis, B.B. Pate, "Photoelectric Emission from the Negative Electron Affinity (100) Diamond Surface - Exciton Effects", *Surf. Sci.* 350 (1996): 315-321.
- [10] L. Diederich, O. Kuettel, P. Aebi, L. Schlapbach, "Electron Affinity and Work Function of Differently Oriented and Doped Diamond Surfaces Determined by Photoelectron Spectroscopy", *Surf. Sci.* 418 (1998): 219-239.
- [11] J.B. Cui, J. Ristein, L. Ley, "Low-Threshold Electron Emission from Diamond", *Phys. Rev. B.* 60 (1999): 16135-16142.
- [12] D. Takeuchi, C.E. Nebel, S. Yamasaki, "Photoelectron Emission from Diamond", *Phys. Stat. Sol. (a)* 203 (2006): 3100-3106.
- [13] D. Takeuchi, H. Kato, G.S. Ri, T. Yamada, P.R. Vinod, D. Hwang, C.E. Nebel, H. Okushi, S. Yamasaki, "Direct Observation of Negative Electron Affinity in Hydrogen-Terminated Diamond Surfaces", *Appl. Phys. Lett.* 86 (2005): 152103.
- [14] F.A.M. Koeck, R.J. Nemanich, A. Lazea, K. Haenen, "Thermionic Electron Emission from Low Work-Function Phosphorus Doped Diamond Films", *Diam. Relat. Mater.* 18 (2009): 789-791.
- [15] V.G. Tkachenko, A.I. Kondrashev, I.N. Maksimchuk, "Advanced metal alloy systems for massive high-current photocathodes", *Appl. Phys. B* 98 (2010): 839-849.
- [16] W.E. Spicer, "Photoemissive, Photoconductive, and Optical Absorption Studies of Alkali-Antimony Compounds", *Phys. Rev.* 112 (1958): 114-122.

- [17] J.W. Schwede, I. Bargatin, D.C. Riley, B.E. Hardin, S.J. Rosenthal, Y. Sun, F. Schmitt, P. Pianetta, R.T. Howe, Z.X. Shen, N.A. Melosh, "Photon-Enhanced Thermionic Emission for Solar Concentrator Systems", *Nat. Mater.* 9 (2010): 762-767.
- [18] J.W. Gadzuk, E.W. Plummer, "Field Emission Energy Distribution (FEED)", *Rev. Mod. Phys.* 45 (1973): 487-548.
- [19] T.L. Westover, A.D. Franklin, B.A. Cola, T.S. Fisher, R.G. Reifenberger, "Photo- and Thermionic Emission from Potassium-Intercalated Carbon Nanotube Arrays", *J. Vac. Sci. Technol. B* 28 (2010): 423-434.
- [20] P. Wurz, R. Schletti, M.R. Aellig, "Hydrogen and Oxygen Negative Ion Production by Surface Ionization Using Diamond Surfaces", *Surf. Sci.* 373 (1997): 56-66.

CHAPTER 4

INTERFACE AND INTERLAYER BARRIERS EFFECTS ON PHOTO-INDUCED ELECTRON EMISSION FROM LOW WORK FUNCTION DIAMOND FILMS

4.1 Abstract

Nitrogen-doped diamond has been under investigation for its low effective work function, which is due to the negative electron affinity (NEA) produced after surface hydrogen termination. Diamond films grown by chemical vapor deposition (CVD) have been reported to exhibit visible light induced electron emission and low temperature thermionic emission. The physical mechanism and material-related properties that enable this combination of electron emission are the focus of this research. In this work the electron emission spectra of nitrogen-doped, hydrogen-terminated diamond films are measured, at elevated temperatures, with wavelength selected illumination from 340 nm to 450 nm. Through analysis of the spectroscopy results, we argue that for nitrogen-doped diamond films on metallic substrates, photo-induced electron generation at optical wavelengths involves both the ultra-nanocrystalline diamond and the interface between the diamond film and metal substrate. Moreover, the results suggest that the quality of the metal-diamond interface can substantially impact the threshold of the sub-bandgap photo-induced emission.

(In collaboration with Franz A.M. Koeck, Petr Stepanov, Gary G. Hembree, and Robert J. Nemanich)

4.2 Introduction

Diamond is unusual for its property of obtaining a negative electron affinity (NEA) surface after hydrogen passivation [1-3]. With an NEA and *n*-type doping, a low effective work function can be achieved, which enables thermionic electron emission from the diamond surface at relatively low temperatures. Current state-of-the-art techniques for preparing nitrogen-doped diamond thermionic electron emitters involve introducing sufficient sp^2 bonds at the grain boundaries to reduce the upward band bending, and an effective work function of 1.3 eV has been reported [4]. Low energy photons have also produced electron emission from N-doped diamond films. This visible light photo-induced emission of N-doped diamond was found to share the same low threshold energy as the thermionic emission [5]. Combining these emission mechanisms may enable applications in thermionic energy conversion [6, 7], and use as a photocathode [8].

A recent study suggested that photon-enhanced thermionic emission (PETE) [9] could be an advantage for combining photo-induced and thermionic emission processes in a novel device structure. Application in a concentrated solar cell was suggested. The proposed cell is composed of two parallel plates serving as the electron emitter and collector, and a vacuum gap separates the two plates. Solar light illuminates the emitter to induce PETE. In this structure, the electron affinity of the semiconductor emitter provides significant contribution to its PETE efficiency. Based on this effect it was proposed that, by coating a semiconductor with a low work function diamond film, high efficiency solar energy conversion could be achieved due to the reduced emission threshold. Efficient transport of electrons through the interface between the substrate and the diamond film

thus becomes a key objective in engineering the related materials. Understanding the effect of film structure on the photo-induced emission from the diamond emitters will be crucial in further development of such multilayer structures. In this work we report a spectroscopic study of photo-induced and thermionic electron emission from N-doped diamond films on metal substrates with different interface and interlayer conditions.

4.3 Experiment

In this research, microwave plasma enhanced chemical vapor deposition (MPCVD) was employed to prepare nitrogen-doped diamond emitters on 25 mm diameter molybdenum substrates. Four variations were prepared for comparison of different interface structures. They include: 1) a combination of mirror polished Mo substrate / nitrogen-incorporated ultra nanocrystalline diamond ((N)UNCD) inter-layer / N-doped diamond (N-diamond) surface layer; 2) bead-blasted Mo substrate / (N)UNCD / N-diamond; 3) bead-blasted Mo substrate / (N)UNCD; and 4) polished Mo substrate / nanodiamond / N-diamond. The four variations are designated by “D1”, “D2”, “D3” and “D4”. Details of the deposition process are described elsewhere [4]. Films of the same structure as D1 were used previously in photo-induced emission studies of N-doped diamond electron emitters [5, 10]. Bead-blasted Mo substrates have been typically employed in prior thermionic emission measurements of N-doped diamond [11]. The nanodiamond layer was deposited under the same parameters as the (N)UNCD, except argon gas was not introduced during the growth process. After growth, the samples were cooled in a hydrogen plasma. This process provides hydrogen termination that leads to an NEA surface, and consequently a low effective work function of the film.

In order to study the optical absorption in the diamond layers, a set of samples were prepared for UV-Vis spectroscopy measurements. This included a sample with (N)UNCD + N-diamond layers and a sample with only the (N)UNCD layer. Both were grown on polished quartz substrates, following the same growth conditions as sample D1. Due to the transparency of the samples, it was difficult to measure the layer thickness through laser reflection interferometry (LRI). The thickness of the (N)UNCD layer was empirically estimated to be ~ 500 nm, and that of the N-doped diamond layer was between 300 and 400 nm. The absorbance data was obtained using a Perkin-Elmer Lambda 18 UV-Vis spectrometer.

For spectroscopic electron emission measurements, the diamond samples were transferred into a UHV chamber for measurements of the photo-induced and thermionic electron emission characteristics. A toroidal tungsten coil beneath the sample holder was used for heating the sample, and the sample temperature was measured with a thermocouple positioned at the center behind the substrate holder. The thermocouple temperature was calibrated with a Mikron M90Q infrared pyrometer. An Oriel 100 W ozone-free Xe arc lamp, fitted with band pass filters ranging from 340 to 450 nm, provided photon illumination at an angle of $\sim 35^\circ$ to the normal direction. The filters had a FWHM of ~ 10 nm. A VSW-HA50 hemispherical electron analyzer positioned normal to the surface was employed to acquire the photo-induced and thermionic emission spectra. The analyzer was operated at resolutions of ~ 0.15 or 0.25 eV to achieve appropriate signal intensity. A negative 15 V bias was applied to the sample surface to maximize the collection of the low energy electrons. Prior to spectroscopic emission measurements, the samples were heated to 450°C for 15 minutes and then cooled in

vacuum. Previous results indicate that water and hydrocarbon contamination is removed from the sample during the degassing process [12]. After this process the samples were heated to and maintained at the specific temperatures, and the photo-induced and thermionic emission spectra were then collected. Spectra obtained at elevated temperatures include contributions from photo induced emission and thermionic emission. The thermionic emission data was subtracted from the combined spectrum in order to obtain the photo-induced emission component. This step has been previously described in more detail [5].

Photoelectron emission and thermionic emission electron microscopy (PEEM / ThEEM) measurements were performed with a prototype Elmitec LEEM III instrument. Samples were loaded onto a holder with integral heating and then inserted into the ultra-high vacuum microscope through a dry-pumped airlock. During the heating experiments the pressure in the main chamber was maintained below 5×10^{-9} Torr. The voltage between the sample surface and anode was kept at a level of 10 kV, and the sample-anode distance was about 2 mm throughout the measurements. An Energetiq Laser Driven Light Source (LDLS), combined with selected optical band pass filters, was used for photo-excitation. The spectrum of the lamp is that of a xenon discharge source, with a nearly constant output from 170 nm to 800 nm. Due to field emission from the high points on the sample, PEEM / ThEEM imaging of the N-doped diamond emitters was only possible from the samples on polished substrates [10]. The images were recorded with the UV 'light-on' (total emission) and 'light-off' (thermionic emission). To obtain an image of the photo-induced emission from a heated sample, the thermionic component

was subtracted from the total emission using the image acquisition and processing program (Actos WinView).

4.4 Results

In order to compare the effects of different layers, optical absorbance measurements were taken from an efficient emitter diamond sample and one without the top N-diamond layer, both on similarly polished quartz substrates. The data is shown in Fig. 4.1, which spans between 200 and 900 nm. Comparison between the two curves suggests that a significant portion of the light was absorbed in the (N)UNCD layer, and the absorption was stronger in the UV regime. The optical absorbance increased significantly and saturated the detector when the wavelength was below 300 nm, which was likely due to absorption from diamond band gap transitions.

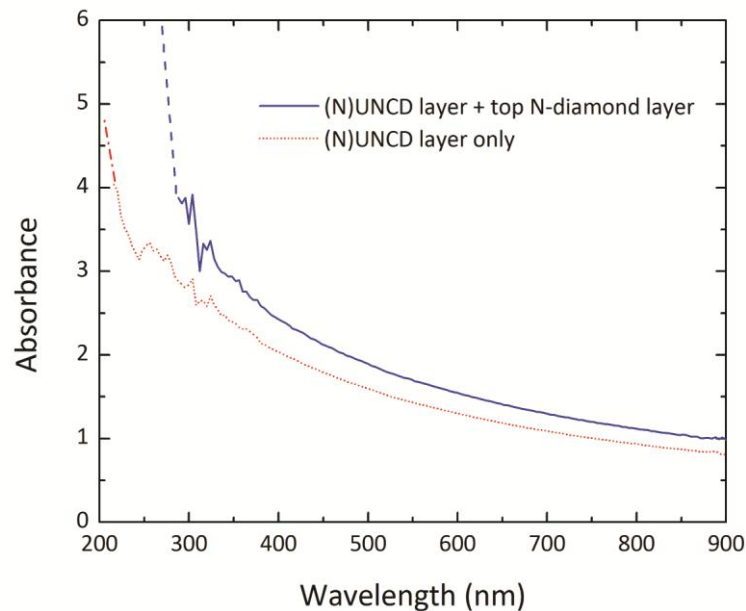


Fig. 4.1 Optical absorbance of the diamond structures, obtained through UV-Vis spectroscopy measurements. The samples are diamond films deposited on polished

transparent quartz substrates, one with only the (N)UNCD layer and the other has a top N-diamond layer in addition.

The electron emission spectra measured from the various samples are shown in Fig. 4.2 in the same sequence as listed in the sample preparation section. The spectra are shown for thermionic emission (“light-off”) at an elevated temperature (denoted as “TE”) and combined emission (“light-on”) at different illumination wavelengths (denoted as “TE + PE” with the corresponding wavelength). The x-axis represents the kinetic energy of the emitted electrons relative to the Fermi level. As noted previously, assuming thermionic and photo-induced emission are independent processes, the photo-induced electron spectra were obtained by subtracting the thermionic component from the combined emission data. Fig. 4.3 shows the thermionic and combined emission spectra and the resultant photo-induced emission components for 340nm (3.65 eV) illumination. The threshold energies for thermionic electron emission (“TE”) and photo-induced electron emission (“PE”) are of particular interest. The effective work function Φ_w for these NEA materials is defined as the energy difference between the conduction band edge of diamond and the Fermi level. Prior studies have demonstrated that the cut-off energy of the thermionic emission spectrum equals Φ_w at the diamond surface, both of which were measured by ultraviolet photoelectron spectroscopy [13]. Here the data shows that, sample D1 exhibits the same low energy cut-off for both emission processes. When either the substrate or the interlayer was changed, larger thresholds for PE were observed. With a bead-blasted Mo substrate, sample D2 presented a PE threshold of ~ 2.2 eV. In Fig. 4.3 (b), this value can be determined clearly by the wavelength dependence of the photo-induced emission spectra. Here the two peaks indicate TE (at low kinetic

energy) and PE (at higher kinetic energy). However, when only (N)UNCD was grown on the bead-blasted Mo substrate (sample D3), TE and PE again shared the same threshold, but at a higher energy of ~ 2.7 eV.

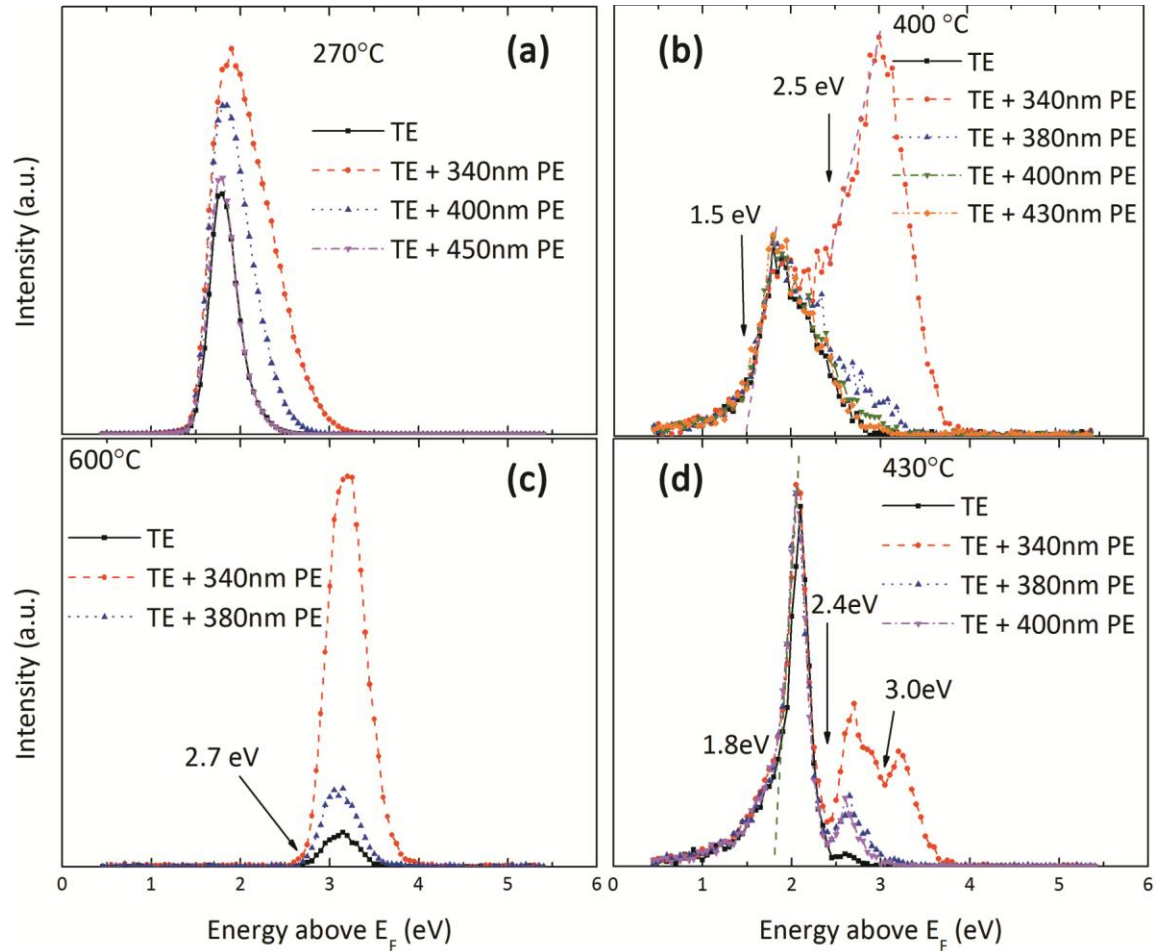


Fig. 4.2 Combined photo-induced and thermionic emission spectra from N-doped diamond films at elevated temperatures, showing the photon energy dependence. The results are shown under the sample sequence of: (a) D1; (b) D2; (c) D3; (d) D4.

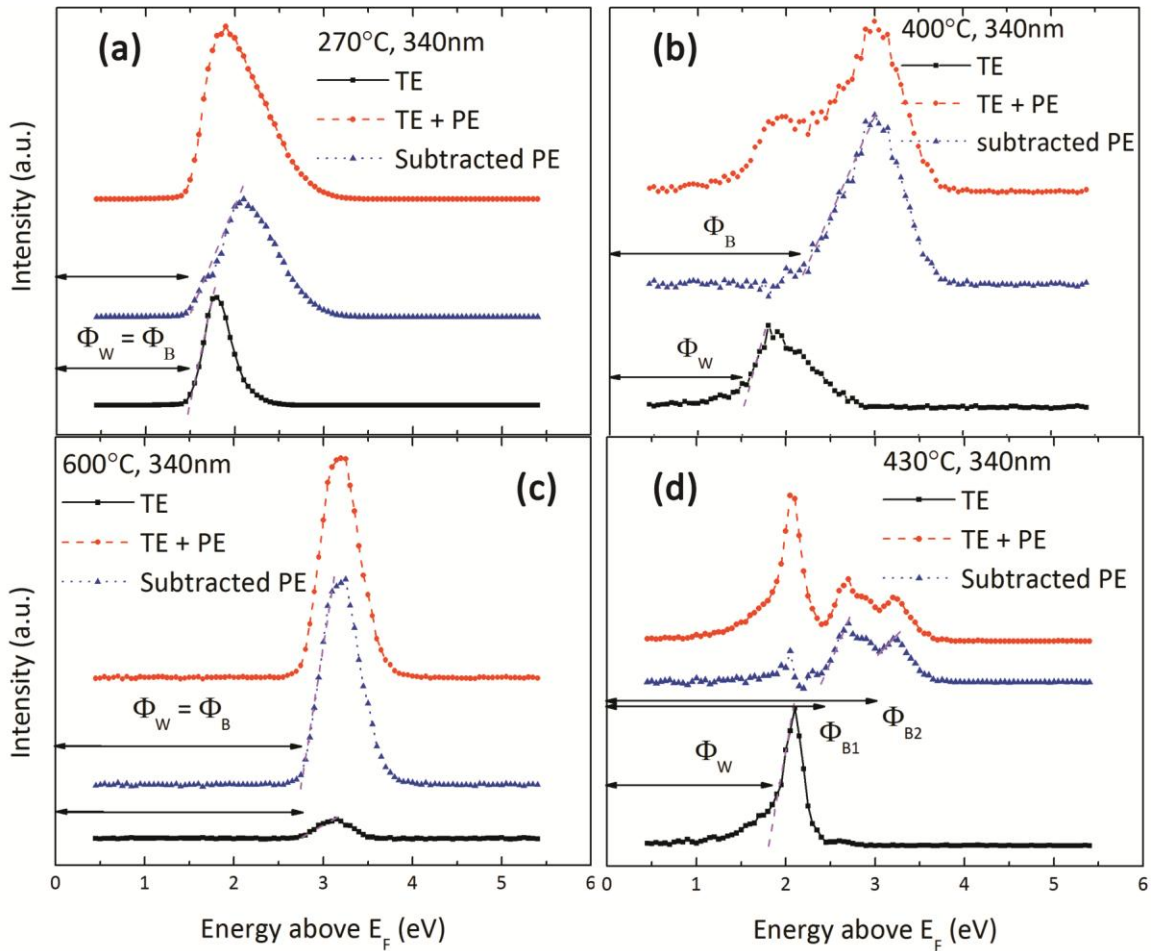


Fig. 4.3 The total emission, thermionic emission, and subtracted photo induced emission spectra components from the diamond samples. Samples are listed in the same sequence as Fig. 4.2.

As shown in Fig. 4.2 (d) and 4.3 (d), a more complex spectrum was observed on sample D4 with the polished Mo / nanodiamond / N-diamond structure. Besides the effective work function of ~ 1.8 eV, which determines the thermionic emission threshold, a cut-off at approximately 2.4 eV and another near 3.0 eV are evident in the photo-induced emission spectra. The cut-off at 3.0 eV can be a separate barrier or a part of the complex structure above 2.4 eV. As the photo-induced emission component of the spectra shows significant wavelength dependence, this 3.0 eV structure was only observed when

the excitation photons have an energy sufficiently high to support a detectable flux of electrons above this energy barrier (in this figure 340 nm light was used, equivalent to ~ 3.65 eV photons). Nevertheless, all samples tested, excluding D1, appear to show an energy barrier between 2.2 to 2.7 eV, which could be a result of the same mechanism; it is possible that the same barrier also exists in D1 but is hidden due to the dominating electron emission over a lower threshold (the surface work function).

To further confirm these photo-induced emission thresholds, the PE components of D2 and D4 are shown in Fig. 4.4. The narrow peak near the TE cut-off in Fig. 4.4 (b) is presumed to be a subtraction artifact caused by a peak shift between the two original spectra (Fig. 4.2 (d)). Comparison between photo-induced emission spectra obtained at lower and higher temperatures is presented in the figure. At the lower temperature thermionic emission is negligible, while at the higher temperature the thermionic emission intensity is comparable with the photo-induced emission, and the TE is subtracted. The low energy cut-off appears to shift slightly to lower energy when temperature increases, which could be a result of increased scattering as electrons transit the diamond film [5]. While the results indicate that temperature may weakly affect the photo-induced emission intensity, the photo-induced emission thresholds were approximately constant.

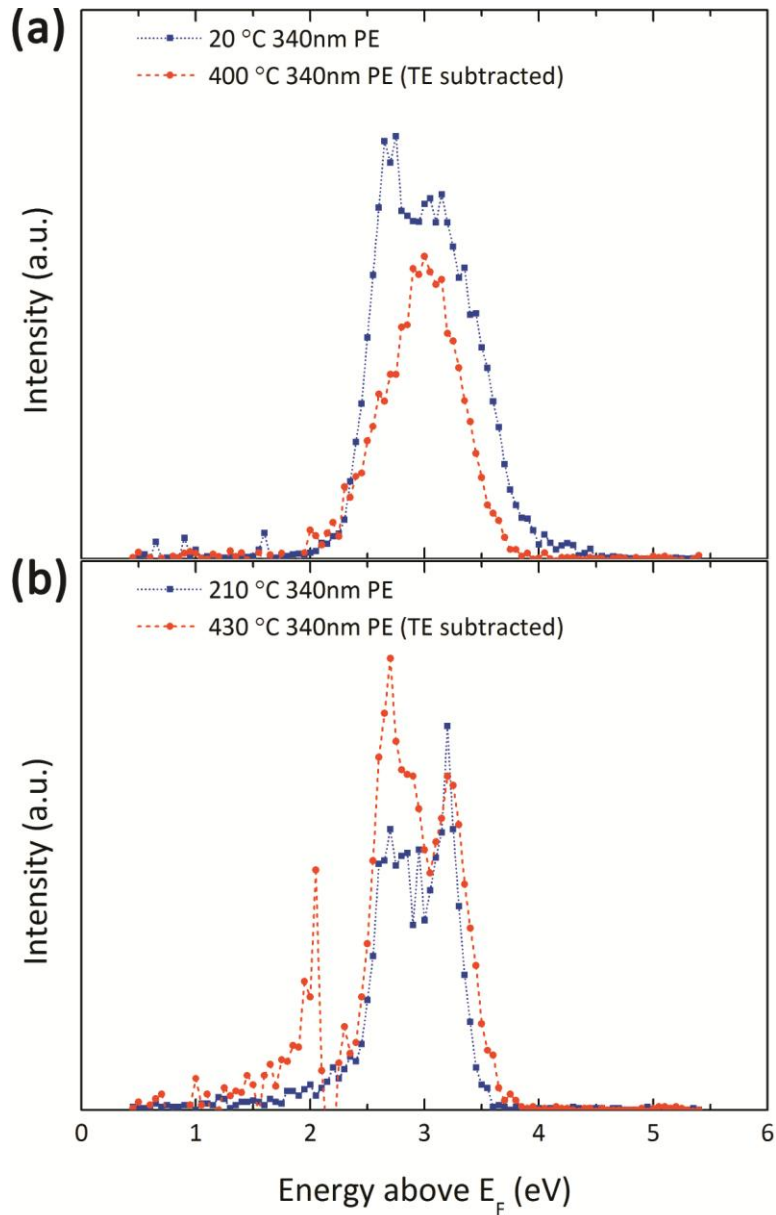


Fig. 4.4 Photo-induced emission spectra of samples (a) D2 and (b) D4 under illumination of the same wavelength, showing comparison between lower (no observable TE) and higher (significant TE observed) temperatures. In both cases the TE is subtracted from the 400 or 430 °C spectra.

PEEM / ThEEM images shown in Fig. 4.5 were obtained from sample D4 (polished Mo / nanodiamond / N-diamond). These images, which are similar to emission

images from other samples of type D1 [10], display a relatively uniform spatial distribution of intensity from both TE and PE processes. Variations in the images are partially due to the 16 °incident angle of the photons, and the polish scratches in the Mo substrate. The photon energy used for the PEEM image was 3.95 eV (314 nm).

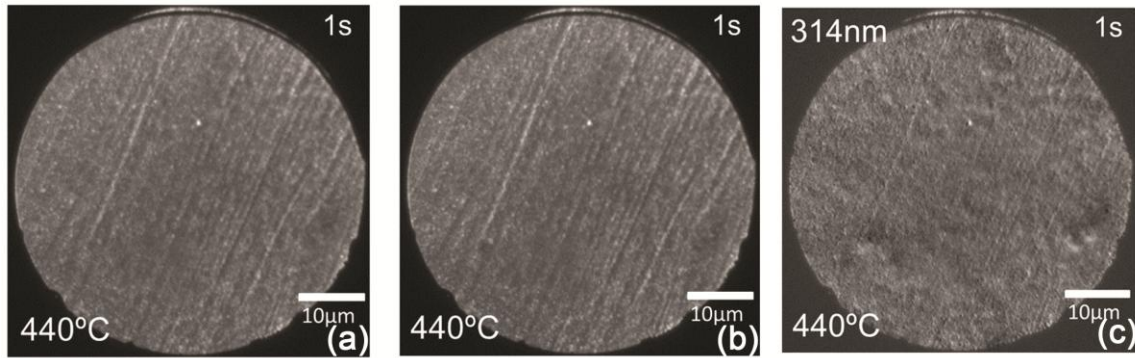


Fig. 4.5 PEEM images of (a) combined emission (“light on”), (b) thermionic emission (“light off”) and (c) subtracted photo-induced emission from the sample with polished Mo substrate / nanodiamond / N-diamond structure (configuration D4).

4.5 Discussion

The spectroscopic results show several intriguing features of the low energy photo induced emission. From all samples tested, the emitted electrons present a low energy cut-off that can be observed from the thermionic emission. Yet, unlike the thermionic emission spectra, the photo-induced emission spectra extend to a maximum kinetic energy that approximately corresponds to the respective photon energy. Assuming Spicer’s three-step model for photoelectron emission [14], photo excited electrons are generated which transit to the sample surface and may be emitted into vacuum. The observed electron energy distribution indicates that the photo-excited electrons are

generated at states near the Fermi level. Due to the wide band gap of diamond (~ 5.5 eV at ambient temperature), it was proposed that the sub-bandgap photons were transmitted through the diamond film and excited electrons at or near the metal-diamond interface [5].

The UV-Vis results of the optical absorbance in the diamond films show that the (N)UNCD exhibits significant optical absorption. The results of photothermal deflection spectroscopy studies [15] also showed that the optical absorption of nitrogen-incorporated nanocrystalline diamond is not negligible. This suggests that photo-excited electrons will be also generated in the diamond film. Nitrogen doping and the consequent shift of E_F may lead to filling of the in-gap states, and the photo-electrons are likely generated from these populated states.

UV-Vis reflectance data also showed that, optical absorption in the top N-diamond layer increases with photon energy, but is generally weaker than in the (N)UNCD layer. By comparing the emission spectra of the second and third sample configurations, it is shown that a higher thermionic emission threshold was observed without the top layer (Fig. 4.2 and 4.3 (c)), and detecting the TE signal required higher temperatures. It appears that the main effect of the top N-doped diamond layer is to provide a low work function surface for the thermionic emission.

The difference observed in the electron emission spectra indicates that the interface and interlayer of the diamond emitters have a substantial effect on the emission characteristics. The origin of the observed energy barriers is not evident, and several possible mechanisms are discussed here. The first hypothesis would relate these thresholds to spatially separated regions on the surface. For instance, carbon patches were

suggested to provide sub-bandgap photo-emission from B-doped single crystal diamond [16]. This suggestion leads to the need for microscopic studies on these samples. While the PEEM images show patches of lower intensity that may be due to surface roughness or variations in work function across the sample, the relatively uniform emission observed from the PEEM / ThEEM images suggests that either the spectral structures are not likely formed by separated domains, or the size of these domains are below the resolution limit for the PEEM images which is ~ 125 nm for these images. An alternative hypothesis is that the additional spectral features result from variations in the electronic structure. Different local bonding configurations of the substrate and interlayer may lead to changes in the band structure and density of states. This includes several possibilities:

A. Changes of the initial states in the photo-generation process, which could alter the distribution of available electrons from the ideal metal parabolic band model.

B. The transport of electrons through the (N)UNCD layer may depend on specific states in the complex nanocrystalline material.

C. The diamond/metal interface may produce a Schottky barrier higher than the surface work function and provide a second barrier.

It is likely that the observed photo-induced emission characteristics are due to a combination of these effects. Nevertheless, it appears that the (N)UNCD layer can significantly contribute to this process. The electronic states of the sp^2 bonds abundant in this layer [17, 18] may result in distinct conductive states corresponding to the additional generation and transmission paths, and possibly affect the interface barriers. As sp^2 bonds of nanocrystalline diamond exist mostly at the grain boundaries, spatial measurements of this process are below the spatial resolution of PEEM due to the small grain size (< 10

nm), and may require other techniques in further research. While the results here also indicate the possible effects of substrate morphology on the photo induced emission process, the mechanism relating it to the electronic structure of the samples is beyond the scope of this work.

The emission mechanisms involving these effects are shown in the band diagram of Fig. 4.6. In this model, the observed photo-induced electron emission involves photo-excited electrons from both the diamond-metal interface and the populated states in the (N)UNCD layer. The electrons transport through the conduction channels in the film and are emitted from the surface layer into vacuum. The photo-induced emission threshold is increased if an extra energy barrier is created, due to changes in initial states, the conduction channels, or interface effects.

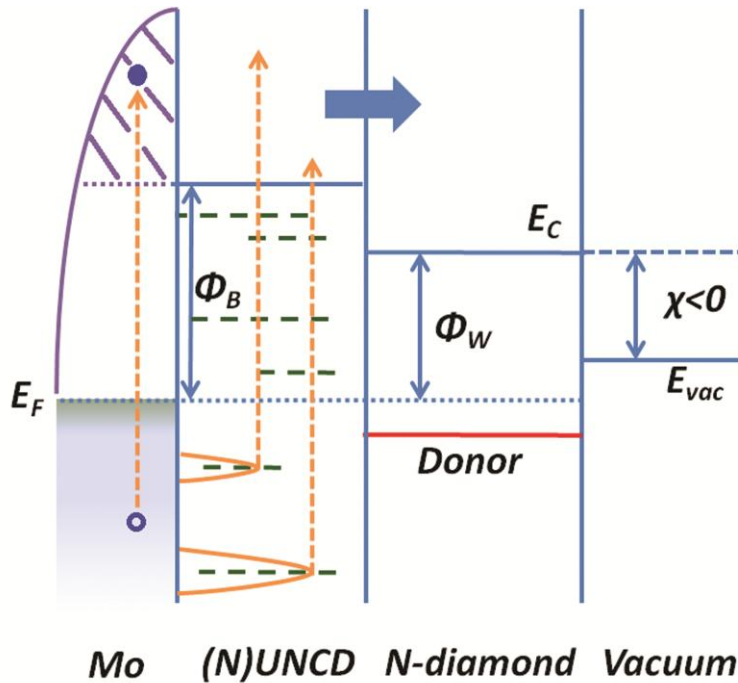


Fig. 4.6 Band schematics of the diamond emitter. Photo-electrons are presumed to be generated in the UNCD layer or near the metal-diamond interface. Dash lines represent the inter-bandgap states, introduced by sp^2 bonds.

4.6 Conclusion

Combined photo-induced and thermionic electron emission of nitrogen-doped, hydrogen-terminated diamond samples was examined with different interface and interlayer conditions between the metal substrate and the top N-doped diamond film. Multiple photo-induced emission thresholds were observed with sub-bandgap photons. PEEM imaging show that these thresholds were either due to variation of the electronic structure of the different sample sets, or from separated emissive domains, the size of which was below the image resolution. This indicates the effects of the interface and interlayer on the photo-induced electron generation, transition and emission. The

relationship between interface bonding and morphology and the electronic structure of the film is yet uncertain. While the underlying physics requires further exploration, the results discussed above indicate its importance in affecting the emission characteristics. Thus, the phenomena reported in this study call for detailed studies in order to optimize the design of diamond based photo induced electron emitters.

References

- [1] F.J. Himpsel, J.A. Knapp, J.A. VanVechten, D.E. Eastman, "Quantum Photoyield of Diamond (111) - A Stable Negative-Affinity Emitter", *Phys. Rev. B* 20 (1994): 624.
- [2] B.B. Pate, "The Diamond Surface: Atomic and Electronic Structure", *Surf. Sci.* 165 (1986): 83.
- [3] J. van der Weide, Z. Zhang, P.K. Baumann, M.G. Wensell, J. Bernholc, R.J. Nemanich, "Negative-Electron-Affinity Effects on Diamond (100) Surface", *Phys. Rev. B* 60 (1994): 8.
- [4] F.A.M. Koeck, R.J. Nemanich, "Low Temperature Onset for Thermionic Emitters Based on Nitrogen Incorporated UNCD Films", *Diam. Relat. Mater.* 18 (2009): 232-234.
- [5] T. Sun, F.A.M. Koeck, C. Zhu, R.J. Nemanich, "Combined Visible Light Photo-Emission and Low Temperature Thermionic Emission from Nitrogen Doped Diamond Films", *Appl. Phys. Lett.* 99 (2011): 202101.
- [6] K. Uppireddi, T.L. Westover, T.S. Fisher, B.R. Weiner, G. Morell, "Thermionic Emission Energy Distribution from Nanocrystalline Diamond Films for Direct Thermal-Electrical Energy Conversion Applications", *J. Appl. Phys.* 106 (2009): 043716.
- [7] F.A.M. Koeck, R.J. Nemanich, "Emission Characterization from Nitrogen-Doped Diamond with Respect to Energy Conversion", *Diam. Relat. Mater.* 15 (2006): 217-220.
- [8] J.D. Rameau, J. Smedley, E.M. Muller, T.E. Kidd, P.D. Johnson, "Properties of hydrogen terminated diamond as a photocathode", *Phys. Rev. Lett.* 106 (2011): 137602.
- [9] J.W. Schwede, I. Bargatin, D.C. Riley, B.E. Hardin, S.J. Rosenthal, Y. Sun, F. Schmitt, P. Pianetta, R.T. Howe, Z.X. Shen, N.A. Melosh, "Photon-enhanced thermionic emission for solar concentrator systems", *Nat. Mater.* 9 (2010): 762-767.

- [10] N. Neugebohrn, T. Sun, F.A.M. Koeck, G.G. Hembree, R.J. Nemanich, T. Schmidt, J. Falta, "Spatial Correlation of Photo-Induced and Thermionic Electron Emission from Low Work Function Diamond Films", *Diam. Relat. Mater.* 40 (2013): 12-16.
- [11] F.A.M. Koeck, R.J. Nemanich, Y. Balasubramaniam, K. Haenen, J. Sharp, "Enhanced Thermionic Energy Conversion and Thermionic Emission from Doped Diamond Films Through Methane Exposure", *Diam. Relat. Mater.* 20 (2011): 1229-1233.
- [12] T. Haensel, J. Uhlig, R.J. Koch, S.I.U. Ahmed, J.A. Garrido, D. Steinmüller-Nethl, M. Stutzmann, J.A. Schaefer, "Influence of Hydrogen on Nanocrystalline Diamond Surfaces Investigated with HREELS and XPS", *Phys. Status. Solidi. A* 206 (2009): 2022-2027.
- [13] M. Kataoka, C. Zhu, F.A.M. Koeck, R.J. Nemanich: "Thermionic electron emission from nitrogen-doped homoepitaxial diamond", *Diam. Relat. Mater.* 19, (2010) 110-113.
- [14] W. E. Spicer, "Photoemissive, Photoconductive, and Optical Absorption Studies of Alkali-Antimony Compounds", *Phys. Rev.* 112 (1958): 114.
- [15] P. Achatz, J.A. Garrido, M. Stutzmann, O.A. Williams, D.M. Gruen, A. Kromka, D. Steinmüller, "Optical Properties of Nanocrystalline Diamond Thin Films", *Appl. Phys. Lett.* 88 (2006): 101908.
- [16] J.B. Cui, J. Ristein, L. Ley, "Low-Threshold Electron Emission from Diamond", *Phys. Rev. B* 60, (1999): 16135.
- [17] S. Bhattacharyya, "Mechanism of High N-Type Conduction in Nitrogen-Doped Nanocrystalline Diamond", *Phys. Rev. B* 70 (2004): 125412.
- [18] K. Subramanian, W.P. Kang, J.L. Davidson, R.S. Takalkar, B.K. Choi, M. Howell, D.V. Kerns, "Enhanced Electron Field Emission from Micropatterned Pyramidal Diamond Tips Incorporating CH₄/H₂/N₂ Plasma-Deposited Nanodiamond", *Diam. Relat. Mater.* 15, (2006): 1126-1131.

CHAPTER 5

PHOTO INDUCED ELECTRON EMISSION FROM NITROGEN DOPED DIAMOND FILMS ON SILICON SUBSTRATES

5.1 Abstract

This work presents a spectroscopic study of the photo-induced electron emission from nitrogen doped diamond films prepared on doped silicon substrates. It has been proposed that photon-enhanced thermionic emission (PETE) can substantially contribute to the emission intensity. The films have been illuminated by employing a Xe arc lamp and band pass filters, and the spectra of the emitted electrons have been recorded as a function of temperature from ambient to ~ 600 °C. In contrast to results for films on metal substrates, a significant increase of emission intensity was observed at elevated temperatures. Modeling approaches are presented to establish the significance of the different emission mechanisms. The results suggest a possible contribution from photon-enhanced thermionic emission (PETE) besides direct photo-electron emission, and indicate possible application in combined solar/thermal energy conversion devices.

(In collaboration with Franz A.M. Koeck, Aram Rezikyan, Mike M.J. Treacy, and Robert J. Nemanich)

5.2 Introduction

Diamond films have shown the property of obtaining a negative electron affinity (NEA) after hydrogen passivation [1-3]. The electron affinity is defined as the energy required to remove an electron from the conduction band minimum (CBM) of a semiconductor into vacuum away from the surface. For NEA diamond films, conduction

band electrons can be readily emitted without the need of overcoming an energy barrier. For nanocrystalline diamond, *n*-type doping has been achieved by incorporation of nitrogen or phosphorus, with a donor level of nitrogen at 1.7 eV and that of phosphorus at 0.6 eV below the CBM [4, 5]. The strong upward band bending often observed in *n*-type doped diamond can be mitigated by introducing sp^2 bonds at the grain boundaries. As a result, NEA and *n*-type doping lead to lowering of the electron emission threshold, i.e. the work function. Effective work functions of 1.3 eV with nitrogen-doping and 0.9 eV with phosphorus-doping have been reported [6, 7]. These low work function surfaces enable low temperature thermionic emission from doped diamond films. For films on metallic substrates, photo-induced electron emission has also been established with visible light excitation [8, 9].

Photons have also been employed to generate electron emission from other novel materials through various physical mechanisms [10, 11]. Notably, a new emission mechanism that combines photo- and thermionic excitation, namely photon-enhanced thermionic emission (PETE), has been shown on *p*-type GaN [12]. In a semiconductor which exhibits PETE, the photons with energy above the band gap will generate electrons in the conduction band and form an enhanced carrier population. This leads to a shift of the quasi-Fermi level in the semiconductor towards the CBM and consequently reduces the effective energy barrier of thermionic emission. As a result, the electron emission intensity may be significantly enhanced with photon illumination. Several theoretical studies have described possible application of PETE in concentrated solar-thermionic energy conversion devices [13-16].

Based on these results, in this work we propose a configuration that combines a nitrogen doped, hydrogen terminated diamond film and a doped semiconductor (Si) substrate. Due to the large band gap of diamond (~ 5.5 eV at room temperature), it is presumed that the illuminating photons will be absorbed in the substrate, which results in enhanced electron emission through the low work function diamond surface. Schematics of the emission mechanism are illustrated in Fig. 5.1: photo-excited electrons are generated in the substrate, transported through the interface towards the diamond surface and contribute to the emission. Alternatively, electrons can be generated directly from valence band states in the Si substrate and injected into the diamond layer without contributing to the enhanced population. This research presents an investigation on the photo-induced electron emission from nitrogen-doped diamond films deposited on Si substrates, and particularly its temperature dependence, to examine the emission mechanisms.

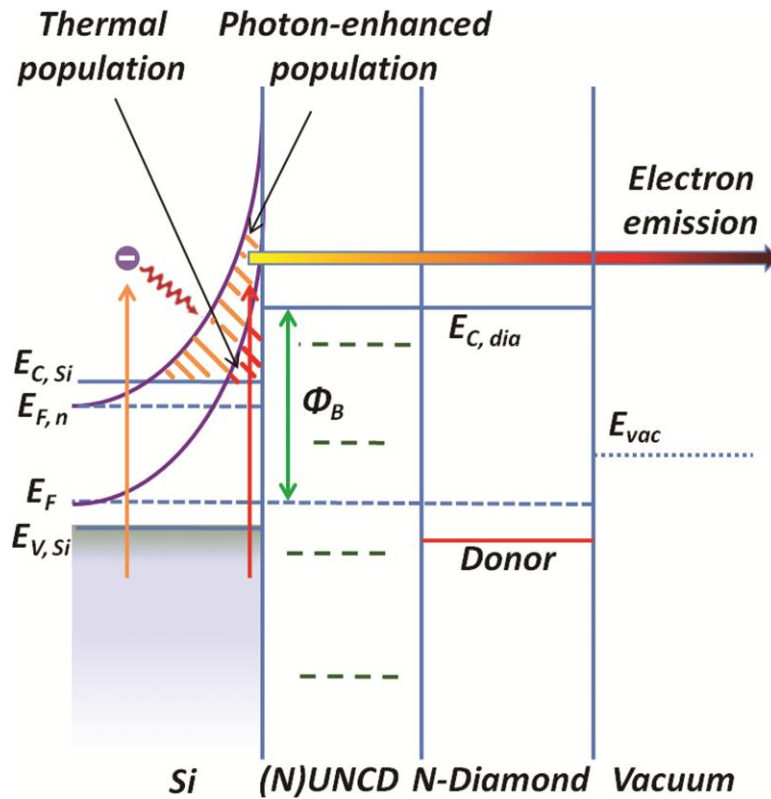


Fig. 5.1 Band schematics of the proposed diamond-Si structure, showing electrons being excited in the absorbing substrate and contributing to the photon-enhanced emission through the low work function surface.

5.3 Experiment

In this work, nitrogen-doped diamond films were prepared on doped single crystal Si substrates by microwave plasma enhanced chemical vapor deposition (MPCVD). Prior to growth, the substrate surface was first abraded with a polishing pad, and then sonicated in a nano-diamond slurry for 40 min. Both the abrasion and sonication processes were followed by an acetone rinse and dry with nitrogen gas. This nucleation step was followed by the deposition of a nitrogen-incorporated ultra-nano crystalline diamond ((N)UNCD) layer and then a N-doped diamond layer. The UNCD layer was deposited

using 10 sccm argon, 100 sccm nitrogen and 20 sccm methane. The N-doped diamond layer deposition employed hydrogen at 400 sccm, methane at 2 sccm, and nitrogen at 100 sccm. After deposition, the samples were exposed to a hydrogen plasma to obtain H-terminated surfaces.

Electron microscopy images of the diamond samples were acquired with a JEOL ARM200F aberration corrected scanning transmission electron microscope (STEM) to examine the diamond/Si interface. The specimen preparation employs a focused ion beam (FIB) lift-out technique in a FEI Nova 200 NanoLab machine with an Omniprobe tip.

For the photo-induced emission experiments, the combined photo-induced and thermionic electron emission spectra are recorded as a function of temperature, using a VSW HA50 hemispherical electron analyzer operating at 0.1 eV resolution. The electron emission spectra were referenced to the Fermi level (E_F) of the metallic sample holders which was calibrated with a gold foil. A tungsten coil beneath the sample provided radiative heating, for a temperature range of 20 to 600 °C. The sample temperature was monitored with a thermocouple located at the center of the coil, and the sample surface was calibrated with a Mikron M90Q infrared pyrometer throughout the experiments. The vacuum pressure was kept between 10^{-9} to 10^{-8} Torr. The photon sources included 21.2 eV UV light from a He I discharge lamp and a focused Oriel 100W Xe arc lamp with associated band pass filters to provide 340 nm to 450 nm photons. These filters have a FWHM of 10 nm. The photon flux was determined by measuring the radiation power density of the filtered light with a Newport 1916-C optical power meter. During measurements at the same temperature set point, the monitored temperature showed a variance of less than ± 2 °C, and the light illumination had no observable effect on

changing the measured sample temperature. A Keithley 237 source measuring unit was employed to record the photo-current between the analyzer and the diamond sample when photon illumination was provided.

5.4 Theoretical Background

The model of PETE is based on a balance between photo-excitation and recombination in a single layer of material that absorbs photons and emits electrons through the same surface. It is assumed that all photons with energy above the band gap of Si (1.12 eV at ambient temperature) are absorbed and converted into conduction band electrons which follow a thermally stabilized Maxwell-Boltzmann distribution, and only the cross-gap recombination through black-body type radiation is considered here by simplification. From the work by Schwede et al. [12], these assumptions lead to the following equations:

$$K_{PETE} = \sqrt{\frac{k_B T}{2\pi m_n^*}} \exp[-\chi / k_B T], \quad (5.1)$$

$$K_{BB} = \frac{2\pi}{h^3 c^2 n_{eq} p_{eq}} \int_{E_G}^{\infty} \frac{(h\nu)^2 d(h\nu)}{\exp(h\nu / k_B T) - 1}, \quad (5.2)$$

$$0 = (\Gamma_P - K_{PETE} n_{eq}) - (K_{PETE} + K_{BB}(n_{eq} + p_{eq})) dn - K_{BB} dn^2, \quad (5.3)$$

$$J = A^* T^2 \exp[-(\Phi - (E_{F,n} - E_F)) / k_B T] = e(n_{eq} + dn) \sqrt{\frac{k_B T}{2\pi m_n^*}} \exp[-\chi / k_B T], \quad (5.4)$$

where Γ_P represents the photon flux, K_{PETE} and K_{BB} the PETE and black-body radiation coefficients respectively, n_{eq} and p_{eq} the equilibrium carrier concentrations, and χ the barrier height with respect to the CBM. Consequently, the PETE current intensity J can

be found by substituting the enhanced population dn from Eq. (5.3) into Eq. (5.4). Auger recombination can be significant with the presence of a large electron population, and will need to be included for a more complete analysis.

It should be noted that the PETE model describes a stronger emission enhancement with elevated temperature from p -type substrates, than from n -type substrates. This is due to the fact that PETE relies on a significant increased electron concentration in the conduction band, and a consequent shift of the electron quasi-Fermi level towards the CBM, to effectively enhance the electron emission. For an n -type material, as electrons are the major carriers and the Fermi level is already close to the CBM, this enhancement from photon illumination will be considerably smaller compared to a p -type material under the same conditions.

Direct photo-electron generation in a semiconductor, on the other hand, focuses on a non-equilibrium process, where the photo-electrons transport across the interface barrier before thermal relaxation. This calls for a separate analysis. This emission mechanism can be simulated by employing an internal photo-emission model [17, 18], which describes the quantum yield as a function of the energy of illuminating photons:

$$Y(h\nu) = \frac{\int_0^{h\nu-E_G} T(E)S(E, h\nu)N_c(E)N_v(E-h\nu)dE}{\int_0^{h\nu-E_G} N_c(E)N_v(E-h\nu)dE}, \quad (5.5)$$

where N_c and N_v are the conduction band and valence band density of states (DoS) in the absorbing substrate, respectively. The energy zero is referred to the CBM. The emitted electron function, $T(E)$, with kinetic energy E overcoming energy barrier χ is given by Fowler's assumption [18, 19] as:

$$T(E) = \frac{1}{2} \left[1 - \sqrt{\frac{\chi}{E}} \right], E \geq \chi; T(E) = 0, E < \chi. \quad (5.6)$$

The absorption function $S(E, h\nu)$ is given in the form of:

$$S(E, h\nu) = \frac{\alpha(h\nu)L(E)}{1 + \alpha(h\nu)L(E)}, \quad (5.7)$$

which involves $\alpha(h\nu)$, the optical absorption coefficient of the absorbing substrate, and $L(E)$, the electron inelastic mean free path (IMFP). As Si has an indirect band gap of 1.12 eV, its optical properties in the UV and visible wavelength regimes show a significant temperature dependence. For instance, the absorption coefficient (α) of 400 nm light in Si has been measured experimentally, and an empirical equation in Ref. [20] is employed here in the form of:

$$\alpha = \exp(3.268 \times 10^{-3} T + 10.466), \quad (5.8)$$

where α is in the unit of cm^{-1} and T is in K. The IMFP of low kinetic energy electrons is usually difficult to determine, and thus in this model it is assumed to be a constant ~ 100 nm. Assuming parabolic DoS for Si and diamond, and substituting Eq. (5.6) and (5.7) into Eq. (5.5), the direct photo-generation efficiency from the specific diamond sample under 400 nm light is obtained through numerical calculation.

As an example, Fig. 5.2 shows results of individually applying the two models to an ideal single-layer electron emitter base on *p*-type Si. The structure includes a constant emission threshold of 0.5 eV above its CBM (i.e. $\chi = 0.5$ eV), and is illuminated under 400 nm photons with a flux of $10^{15} \text{ cm}^{-2}\text{s}^{-1}$. To simplify the calculation of the emission current, the ideal Richardson constant of $120 \text{ A/cm}^2\text{K}^2$ is employed. The results of the PETE model contain the net current density, and the components contributed by both the

"pure" thermionic emission and the PETE mechanism. Comparison between the two models shows apparently different features: the direct photoemission is relatively constant within the tested temperature regime, while the PETE induced charge distribution is affected by temperature, and consequently the PETE model results in a more significant temperature dependence. At higher temperatures (>400K), the PETE model starts to show a much stronger electron emission than direct photoemission.

To apply the two single-layer models introduced above to a diamond-Si bi-layer structure, it is assumed that the emission threshold is determined by the interface conduction band barrier, and replaces χ in the above equations with the values of this barrier as experimentally measured in the photo-induced emission spectra. Additionally, recombination due to the diamond-Si interface is also ignored, assuming ideal electron transport properties.

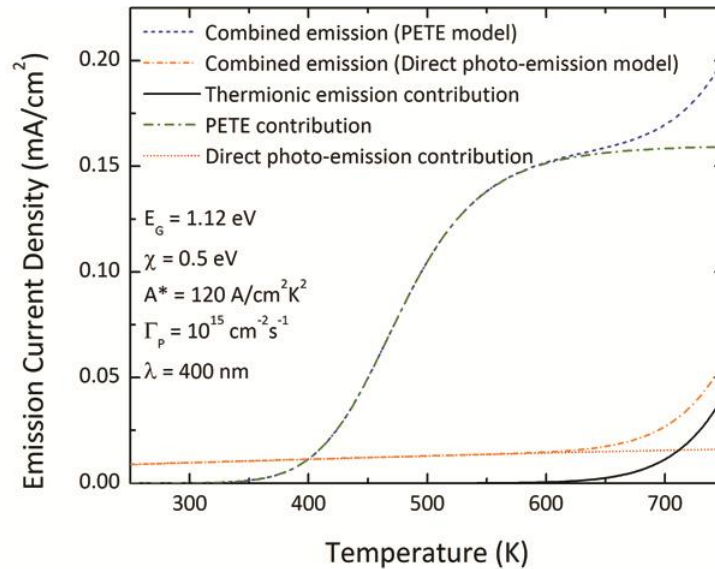


Fig. 5.2 Simulation results of the two models on an ideal electron emitter, which has a band gap of 1.12 eV, electron affinity of 0.5 eV, and is under illumination of 400 nm light with a photon flux of $10^{15} \text{ cm}^{-2}\text{s}^{-1}$.

5.5 Results

Electron microscopy images (Fig. 5.3) indicate a continuous interface between Si and the (N)UNCD. Electron energy loss spectroscopy (EELS) scans suggest no observable formation of SiC at the interface. A grain size of less than 10 nm is shown in the (N)UNCD layer.

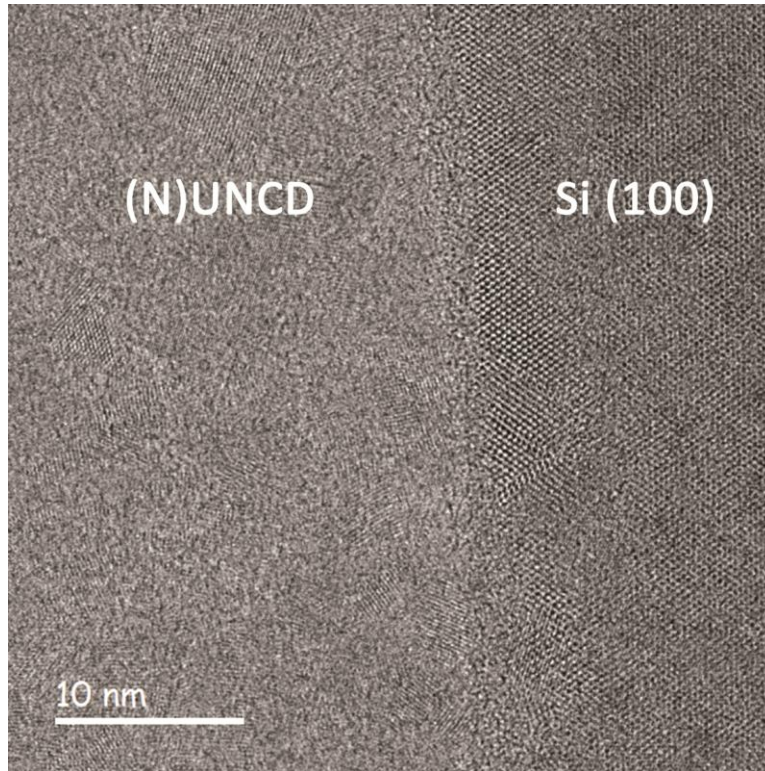


Fig. 5.3 High resolution electron microscopy image of the diamond/Si interface, showing the (N)UNCD on the left and single crystal Si on the right.

Fig. 5.4 shows UV photoemission spectra (21.2 eV excitation energy) as a function of temperature, collected from a nitrogen doped diamond film on *p*-type Si substrate. As the photon energy is larger than the bandgap of diamond, the electrons are excited from valence band states close to the surface of diamond. The electrons in the conduction band lead to the photoemission spectra. Thus, the low energy cut-off of the

spectra represents the effective work function Φ_w of the N-diamond surface layer. A low value (1.5 to 1.6 eV) was observed, which remains approximately constant within the studied temperature regime.

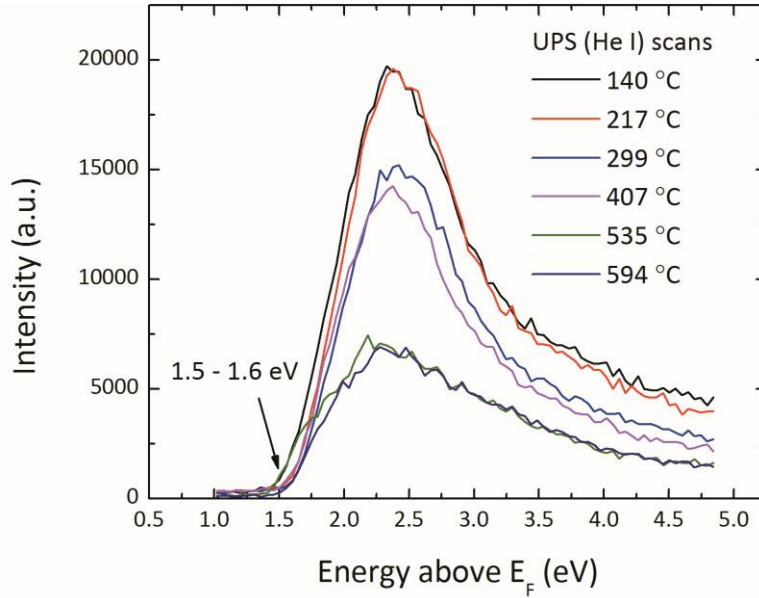


Fig. 5.4 UV (21.2 eV) photoemission spectra of a nitrogen doped diamond film on *p*-type Si substrate. An effective work function of ~ 1.5 eV was observed and kept relatively independent of temperature.

Fig. 5.5 includes photo-induced emission spectra collected while the samples were illuminated by photons of the selected wavelength. Samples with both *p*-type (boron doped) and *n*-type (phosphorus doped) Si substrates were examined. When measured at elevated temperatures, the samples also exhibited thermionic emission without photon illumination. The thermionic emission spectra ("light-off") were subtracted from the combined emission ("light-on") to obtain the photo-induced component. In contrast to the UV (21.2 eV) photo-emission results, the visible light photo-induced emission spectra exhibited a higher threshold energy which decreased at elevated temperatures. At \sim

600 °C where thermionic emission started to be detected, this threshold was found to be approximately the same as the surface work function (1.5 eV). This effect is possibly due to electrons tunneling through the interface barrier at elevated temperatures. The measured photo-current was typically in the range of 0.5 to 5 nA depending on the photon energy, which corresponded to an effective quantum efficiency of $\sim 10^{-5}$ to 10^{-4} .

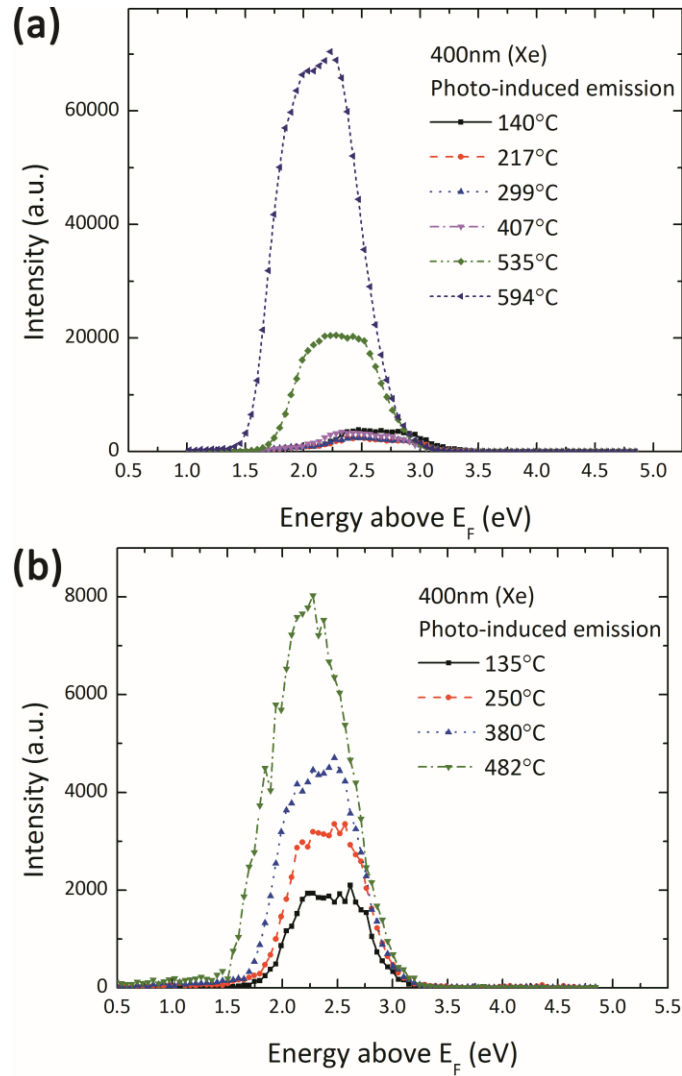


Fig. 5.5 Photo-induced emission spectra from nitrogen-doped diamond films on Si. The Si substrates are of (a) *p*-type doping and (b) *n*-type doping.

Moreover, the intensity of the visible light photo-induced emission significantly increases with temperature. Fig. 5.6 (a) shows the integrated spectral intensities with various illuminating wavelengths. The results exhibited an intensity increase by a factor of 6 to 30 for the different excitation energies, while the sample temperature was increased by ~ 500 °C. In contrast, this strong temperature dependence was not observed from diamond films deposited on metal substrates. These diamond-metal samples have shown relatively constant photo-induced emission intensity [7, 8], as described in the conventional Fowler-DuBridge model [11, 19] which involves only direct photoemission. These results are consistent with the model discussed here, since PETE is not expected from a metal substrate.

Comparison between experimental data and modeling results from a nitrogen-doped diamond film deposited on *p*-type Si are shown in Fig. 5.6 (b). The experimental points include data from both the integrated spectral intensity and the photo-current as collected during measurements. In this experiment, the sample was illuminated under 400 nm (3.1 eV) photons with a flux of 10^{15} cm⁻²s⁻¹. The thermionic emission contribution was subtracted from the combined emission spectrum. The numerical calculations were based on the same temperature, wavelength and photon flux used for the measurements, also showing only contributions from photon illumination. A photo-emission barrier of 2.2 eV was observed at ambient temperature and decreased to 1.9 eV (668 K). This change of photo-emission barrier, similar to that in Fig. 5.5, was represented in the models as a linear function of temperature. To reference the results obtained from the different methods, the values were normalized to the intensity (photo-current) at 668 K. In the numerical simulation, both models indicate an enhancement with increased

temperature, yet the experimental data showed somewhat intermediate characteristics: a combination of $\sim 50\%$ of relative intensities from each model provided a better fit with the experimental data.

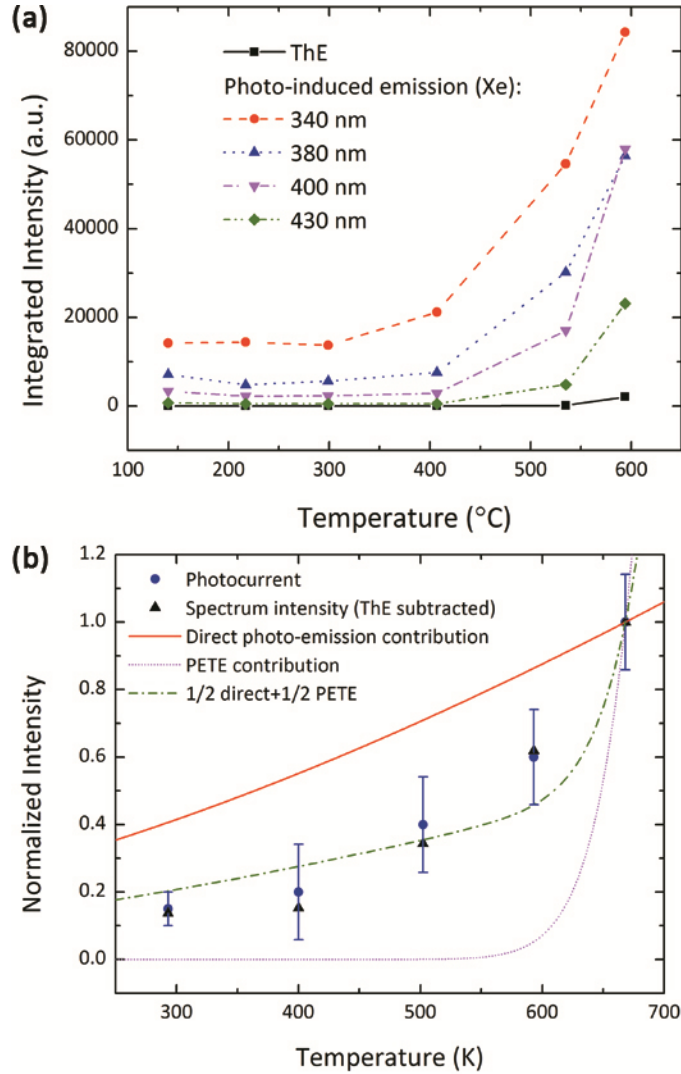


Fig. 5.6 (a) Temperature dependence of integrated photo-induced emission intensity and thermionic emission intensity, obtained from a nitrogen-doped diamond film on a *p*-type Si substrate, showing results with different excitation energies; (b) Comparison between simulated (direct photo-emission and PETE models) and experimental results (spectral intensity and photo-current). A combined curve of 50% direct photo-emission and 50%

PETE is shown with the dashed line, indicating a contribution from the two generation processes.

After testing samples prepared under different conditions, we note that properties of the diamond-Si interface could affect the emission characteristics. The samples were found to show degradation after measurements at high temperature, and the photon-enhancement reduced in repeated experiments. This could be possibly related to hydrogen evolution at the diamond surface or inside the film.

5.6 Discussion

The key question of this study is whether photon-enhanced thermionic emission (PETE) is observed. The results appear to support that the PETE mechanism is at least partially responsible for the emission. Most significantly, the obtained spectral intensity shows a temperature dependence that was not observed on diamond samples with metal substrates. It could be argued that this effect is partly due to the decrease of the emission threshold, as this threshold limits the electron emission in both PETE and direct-generation models. For instance, according to results shown in Fig. 5.5 (a), the diamond sample exhibited a threshold for photo-induced emission at ~ 2.0 eV at 140 °C. This threshold decreases to 1.5 eV at ~ 600 °C. Applying the direct-generation model with the corresponding values leads to an emission enhancement by a factor of 3.6 with 400 nm photon illumination. This however is not sufficient to support that the experimental spectral intensity increased by a factor of approximately 7.9 . This comparison indicates that the PETE mechanism is likely represented in the experiment.

Interestingly, as shown in Fig. 5.5, comparison between the samples with p -type and n -type Si substrates indicates that this enhancement appears to be more significant on a p -type substrate than an n -type one. In both cases a strong temperature dependence of the photo-induced emission intensity was observed. The diamond film on p -type Si exhibits an apparently greater increment ratio, as the emission intensity increases by approximately one order of magnitude at ~ 600 °C.

Meanwhile, there is also evidence that suggests the significance of emission mechanisms other than PETE. At lower temperatures (below 200 °C) photo-induced emission can be observed, although the PETE model predicts negligible emission under such conditions. Also, while showing significant temperature dependence, the photo-induced spectra of the diamond-Si samples still show many similarities to the results collected from diamond films deposited on metal substrates. For instance, in the spectra the maximum kinetic energy of the electrons above E_F approximately corresponds to the energy of the illuminating photons. Previously it was concluded from this that these high energy electrons are from directly excitation of states near E_F [8]. This supports the direct generation model as E_F in a heavily doped p -type Si wafer is close to the VBM. In the PETE mechanism, however, the emission spectra are expected to be almost independent of photon energy [12], since the photo-electrons are thermally stabilized into a Maxwell-Boltzmann distribution regardless of the excitation energy.

Therefore, direct generation of photo-electrons cannot be neglected in the observed photo-induced electron emission. In a recent study of N-doped diamond (see Chapter 4), it was concluded that the photo-electrons can be generated in the substrate or in the nucleation layer which has a higher density of sp^2 bonds in the grain boundaries.

The latter is not yet included in the models discussed above, and the actual generation and transport of photo-electrons can be a more complex process. A more advanced model would be necessary to better assess the specific mechanisms of the more complex structure.

The relative significance of the PETE and direct-generation processes may be related to the properties of the absorbing substrate material. The material will more likely exhibit PETE if forming a quasi-equilibrium population of photo-excited electrons is more physically favorable than direct injection of these electrons across the barrier. Additionally, an optimal bandgap of the substrate is required to absorb a wide solar spectrum while the recombination can be effectively controlled. We have assumed that a semiconductor with an indirect bandgap (e.g. Si) will present strong PETE-type emission, due to reduced cross-gap recombination and a longer relaxation time. These properties, and the NEA of diamond surfaces, lead to the proposed structure in this work. Theoretically, the optimal bandgap for PETE materials has been predicted to be 1.4 eV [12, 15], and candidate substrates including InGaN and InP have been suggested. The properties of these materials related to electron generation and transport will need to be addressed in order to develop high efficiency PETE devices.

5.7 Conclusion

Significant increase of photo-induced electron emission with elevated temperature has been observed from nitrogen doped diamond films on silicon substrates. The results differ from previously reported features of diamond emitters on metal substrates, where a relatively constant photo-induced emission was observed. A possible photon-enhanced

thermionic emission (PETE) mechanism is suggested, which involves generation of an enhanced electron population and lowering of the emission barrier in the absorbing Si substrate. Computer-based modeling is employed to compare different physical mechanisms, and the results appear to indicate a complex generation process. As significant enhancement of electron emission is shown through combined excitation from heat and light, such diamond emitters could potentially be applied in concentrated solar collection systems for solar-thermionic energy conversion. Examination of different substrate candidates for optimized PETE configuration will be important in the future.

References

- [1] F.J. Himpsel, J.A. Knapp, J.A. VanVechten, D.E. Eastman, "Quantum Photoyield of Diamond (111) - A Stable Negative-Affinity Emitter", *Phys. Rev. B* 20 (1994): 624.
- [2] B.B. Pate, "The Diamond Surface: Atomic and Electronic Structure", *Surf. Sci.* 165 (1986): 83.
- [3] J. van der Weide, Z. Zhang, P.K. Baumann, M.G. Wensell, J. Bernholc, R.J. Nemanich, "Negative-Electron-Affinity Effects on Diamond (100) Surface", *Phys. Rev. B* 60 (1994): 8.
- [4] R.G. Farrer, "On the substitutional nitrogen donor in diamond", *Solid State Commun.* 7 (1969): 685-688.
- [5] K. Haenen, K. Meykens, M. Nesladek, G. Knuyt, L.M. Stals, T. Teraji, S. Koizumi, E. Gheeraert, "Phonon-Assisted Electronic Transitions in Phosphorus-Doped N-Type Chemical Vapor Deposition Diamond Films", *Diam. Relat. Mater.* 10 (2001): 439-443.
- [6] F.A.M. Koeck, R.J. Nemanich, "Low Temperature Onset for Thermionic Emitters Based on Nitrogen Incorporated UNCD Films", *Diam. Relat. Mater.* 18 (2009): 232-234.
- [7] F.A.M. Koeck, R.J. Nemanich, A. Lazea, K. Haenen. Thermionic electron emission from low work-function phosphorus doped diamond films. *Diam. Relat. Mater.* 18, 789-791 (2009).

- [8] T. Sun, F.A.M. Koeck, C. Zhu, R.J. Nemanich, "Combined Visible Light Photo-Emission and Low Temperature Thermionic Emission from Nitrogen Doped Diamond Films", *Appl. Phys. Lett.* 99 (2011): 202101.
- [9] N. Neugebohrn, T. Sun, F.A.M. Koeck, G.G. Hembree, R.J. Nemanich, T. Schmidt, J. Falta, "Spatial Correlation of Photo-Induced and Thermionic Electron Emission from Low Work Function Diamond Films", *Diam. Relat. Mater.* 40 (2013): 12-16.
- [10] M.V. Moghaddam, P. Yaghoobi, A. Nojeh, "Polarization-Dependent Light-Induced Thermionic Electron Emission from Carbon Nanotube Arrays Using a Wide Range of Wavelengths", *Appl. Phys. Lett.* 101 (2012): 253110.
- [11] P.T. McCarthy, S.J. Vander Laan, D.B. Janes, T.S. Fisher, "Photonicallly Excited Electron Emission from Modified Graphitic Nanopetal Arrays", *J. Appl. Phys.* 113 (2013): 193710.
- [12] J.W. Schwede, I. Bargatin, D.C. Riley, B.E. Hardin, S.J. Rosenthal, Y. Sun, F. Schmitt, P. Pianetta, R.T. Howe, Z.X. Shen, N.A. Melosh, "Photon-Enhanced Thermionic Emission for Solar Concentrator Systems", *Nat. Mater.* 9 (2010): 762-767.
- [13] A. Varpula, M. Prunnila, "Diffusion-Emission Theory of Photon Enhanced Thermionic Emission Solar Energy Harvesters", *J. Appl. Phys.* 112 (2012): 044506.
- [14] T. Ito, M.A. Cappelli, "Optically Pumped Cesium Plasma Neutralization of Space Charge in Photon-Enhanced Thermionic Energy Converters", *Appl. Phys. Lett.* 101 (2012): 213901.
- [15] G. Segev, A. Kribus, Y. Rosenwaks, "High Performance Isothermal Photo-Thermionic Solar Converters", *Sol. Energ. Mat. Sol. C.* 113 (2013): 114-123.
- [16] G. Segev, Y. Rosenwaks, A. Kribus, "Loss mechanisms and back surface field effect in photon enhanced thermionic emission converters", *J. Appl. Phys.* 114 (2013): 044505
- [17] N.B. Kindig, W.E. Spicer, "Band Structure of Cadmium Sulfide - Photoemission Studies", *Phys. Rev.* 138 (1965): A561-576.
- [18] R.J. Powell, "Interface barrier energy determination from voltage dependence of photoinjected currents", *J. Appl. Phys.* 41 (1970): 2424-2432.
- [19] R.H. Fowler, "The Analysis of Photoelectric Sensitivity Curves for Clean Metals at Various Temperatures", *Phys. Rev.* 38 (1931): 45.
- [20] G.E. Jellison, F.A. Modine, "Optical functions of silicon at elevated temperatures", *J. Appl. Phys.* 76 (1994): 3758.

CHAPTER 6

ELECTRON AFFINITY OF DOPED DIAMOND SURFACES WITH VANADIUM- OXIDE-TERMINATION

6.1 Abstract

This work presents an *in-situ* photoelectron spectroscopy study of the electronic structure of vanadium-oxide-terminated polycrystalline diamond. Thin layers of vanadium were deposited on oxygen-terminated, boron-doped and nitrogen-doped diamond samples by employing an electron beam deposition system. Vanadium oxide was formed immediately after deposition. After oxide formation and 650 °C thermal annealing, the effective work function was significantly decreased, which indicates a negative electron affinity on boron-doped diamond, while a 1.1 ± 0.2 eV positive electron affinity was found on nitrogen-doped diamond. We argue that this is likely resulted from the difference in the interface barrier at the diamond-oxide interface.

(In collaboration with Manpuneet Kaur, Muhammad Zamir Othman, Jialing Yang, Franz A.M. Koeck, Paul W. May, and Robert J. Nemanich)

6.2 Introduction

Diamond can exhibit a negative electron affinity (NEA) surface after hydrogen termination [1-3]. For a NEA material, the vacuum level lies below the conduction band minimum (CBM), and electrons present in or promoted into the conduction band can be emitted from the surface into vacuum without an energy barrier. Through *n*-type [4-5] and *p*-type [6] doping, diamond films prepared by chemical vapor deposition (CVD) methods have shown significantly increased electrical conductivity. These doped and H-

terminated diamond films exhibit strong electron emissivity, and have been considered as electron sources for application, including photo-electrochemistry substrates [7-8], photocathodes [9], thermionic and photo-thermionic energy conversion devices [4, 5, 10].

In addition to hydrogen termination, other surface termination techniques have also been established. Our group has reported that in-situ coating of the single crystal diamond surface with a thin metal layer could affect the surface electron affinity [11-13]. This was attributed to the Schottky barrier formed at the diamond-metal interface. Diamond surfaces with metal oxide termination have also been analyzed [14-15]. The metal oxide termination is argued to create a NEA surface as a result of the surface dipole formed through carbon-oxygen-metal bonds. The two models (interface barrier and oxide dipole) are illustrated in Fig. 6.1. One of the challenging aspects of previously studied metal oxide termination, such as CsO, is their limited ability to withstand high temperature operation, which is important in thermionic emission applications. These studies, however, have been mostly focused on intrinsic or boron-doped (*p*-type) diamond samples, while nitrogen-doped (*n*-type) diamond has not been studied as extensively. Conversely, NEA nitrogen doped diamond has shown thermionic emission and visible light photoemission [10].

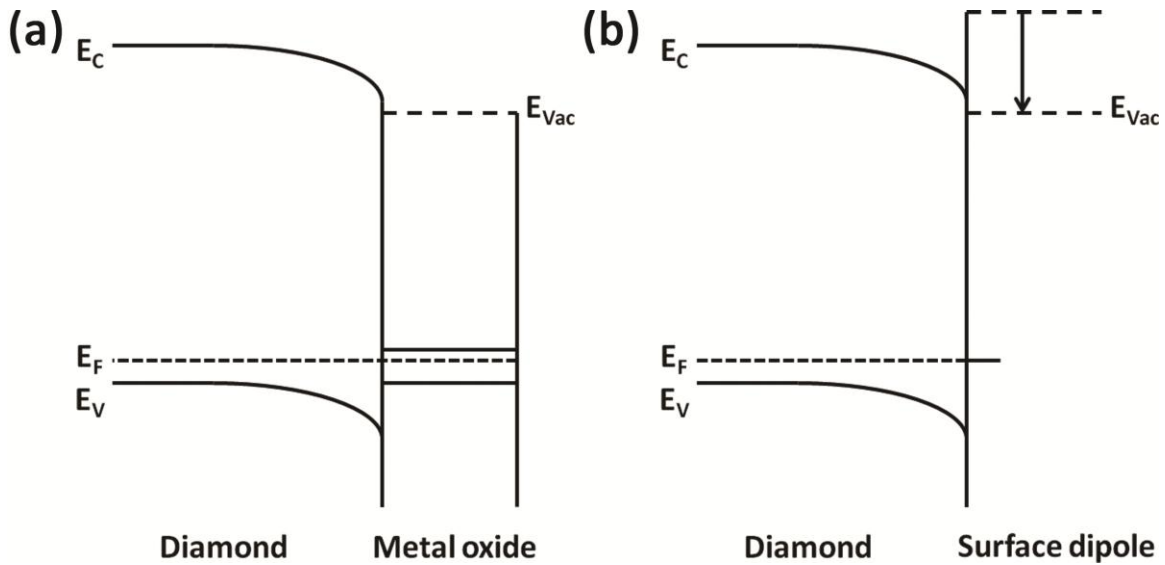


Fig. 6.1 Band schematics of the two models: (a) The barrier at the oxide-diamond interface effectively reduces the electron emission threshold, creating a NEA surface; (b) The metal-oxide dipole at the diamond surface changes the vacuum level, which is lower than the CBM, leading to a NEA.

Recently diamond-based materials have been suggested as promising candidates for high power and high frequency transistors [16, 17]. Electronic structures of some high- k dielectric metal oxides (Al_2O_3 , HfO_2) deposited on diamond substrates have been under investigation [18]. Vanadium oxides (V_2O_3 , VO_2 , V_2O_5) show insulator-to-metal transition (IMT) at critical temperatures (160 K, 340 K and 530 K respectively) [19, 20], and have been applied together with these high- k dielectric metal oxides in charge storage gate stack structures [21]. Additionally, vanadium oxide films on diamond substrates have also been studied for applications as catalysts [22]. These studies have motivated us to conduct a study of the electron affinity of vanadium-oxide-terminated diamond samples, in order to examine and compare the properties of both boron and nitrogen doped diamond.

6.3 Experiment

The experiments were accomplished in-situ by employing an integrated ultrahigh vacuum (UHV) system. This system has a linear UHV transfer line which connects different processing and characterization chambers. In this study, the following systems were used: remote oxygen plasma for sample cleaning and surface oxygen termination, reactive electron beam deposition system for vanadium deposition, x-ray photoelectron spectroscopy (XPS) for core level analysis, and ultraviolet photoelectron spectroscopy (UPS) for valence band analysis.

The substrates for vanadium deposition were (a) 1cm × 1cm square, boron-doped (*p*-type), electrochemistry grade, free-standing polycrystalline diamond with a boron concentration $> 10^{20} \text{ cm}^{-3}$, obtained from Element Six, Ltd.; and (b) nitrogen-doped (*n*-type) nanocrystalline diamond film, deposited on 25-mm-diameter molybdenum substrates by microwave plasma enhanced chemical vapor deposition (MPCVD), at Arizona State University. The deposition process of the N-doped diamond has been described elsewhere [4]. Before loading into the UHV chamber, the B-doped diamond substrates were cleaned in an ultrasonic bath of 95% sulfuric acid for 15 min, an ultrasonic bath of de-ionized water for another 15 min, and the surfaces were blown dry with ultra-high purity (UHP) nitrogen gas. The N-doped diamond substrates were H-terminated after deposition through exposure to a hydrogen plasma, and were cleaned with only the UHP nitrogen gas.

After transfer into the UHV system, the samples were further cleaned by a remote oxygen plasma, resulting in an oxygen terminated surface. The plasma exposure conditions were as follows: substrate at ambient temperature, 100 mTorr oxygen

pressure, gas flow of 30 standard cubic centimeters per minute (sccm), and RF power of 30 W to excite the remote plasma.

The vanadium films were deposited in the reactive electron beam deposition system which has a base pressure of 5×10^{-9} Torr. The electron beam crucibles were filled with vanadium metal of 99.8% purity. A film with a thickness of 0.1 nm was deposited onto the oxygen-terminated diamond sample at ambient temperature, with a vapor pressure of 1×10^{-7} Torr. A growth rate of ~ 0.01 nm/s was monitored and maintained with a quartz crystal microbalance (QCM).

The sample was characterized by in-situ XPS and UPS at each step. XPS characterization was performed using the 1253.6 eV Mg K α line of a VG XR3E2 dual anode source and a VG microtech Clam II analyzer operated at a resolution of 1.0 eV. The peak positions could be further resolved into ± 0.1 eV through curve fitting. The XPS was calibrated to align the Au 4f $_{7/2}$ peak to 84.0 eV by measuring a standard gold foil. UPS scans were obtained using the He I line at 21.2 eV from a He discharge lamp, and the spectra were recorded by a VSW HA50 hemispherical analyzer and VSW HAC300 controller operated at a resolution of 0.15 eV. A negative 8.0 V bias was applied to the substrate to overcome the work function of the analyzer. Spectra collected by the UPS system were calibrated against a standard gold foil, and referenced to the Fermi level (E_F) of the metallic sample holder. Samples were annealed in the UPS chamber with a tungsten irradiation heater coil beneath the sample holder. The temperature of the sample was controlled by a thermocouple positioned behind the center of the sample, and calibrated by a Mikron M90Q infrared pyrometer.

6.4 Results

6.4.1 O-termination through O-plasma treatment

The effect of oxygen termination was examined by comparing the photoemission spectra of an N-doped diamond (NDD) film before and after O-plasma treatment. XPS and UPS scans are shown in Fig. 6.2. As anticipated, after the O-plasma treatment the O 1s signal increased significantly. The C 1s peak shifted 0.6 eV towards lower binding energy after O-termination, indicating an increase of upward band bending. The binding energy difference between the C 1s core level and the valence band maximum (VBM) of diamond was approximately 283.2 ± 0.2 eV and 283.4 ± 0.2 eV for H- and O-termination respectively. These values approximately agree with results of an XPS investigation on epitaxial diamond [18], where a binding energy difference of 283.1 ± 0.2 eV was reported. An effective work function of 2.5 eV above the original E_F was found on the H-terminated surface. Assuming this low energy threshold corresponds to the CBM of the H-terminated diamond film, a band gap of 5.1 ± 0.2 eV was deduced using the measured valence band maximum relative to the E_F . After O-termination the work function increased to 5.2 eV after O-plasma treatment. By applying the same band gap, a positive electron affinity (PEA) of 1.9 ± 0.2 eV was deduced for the O-terminated N-doped diamond film.

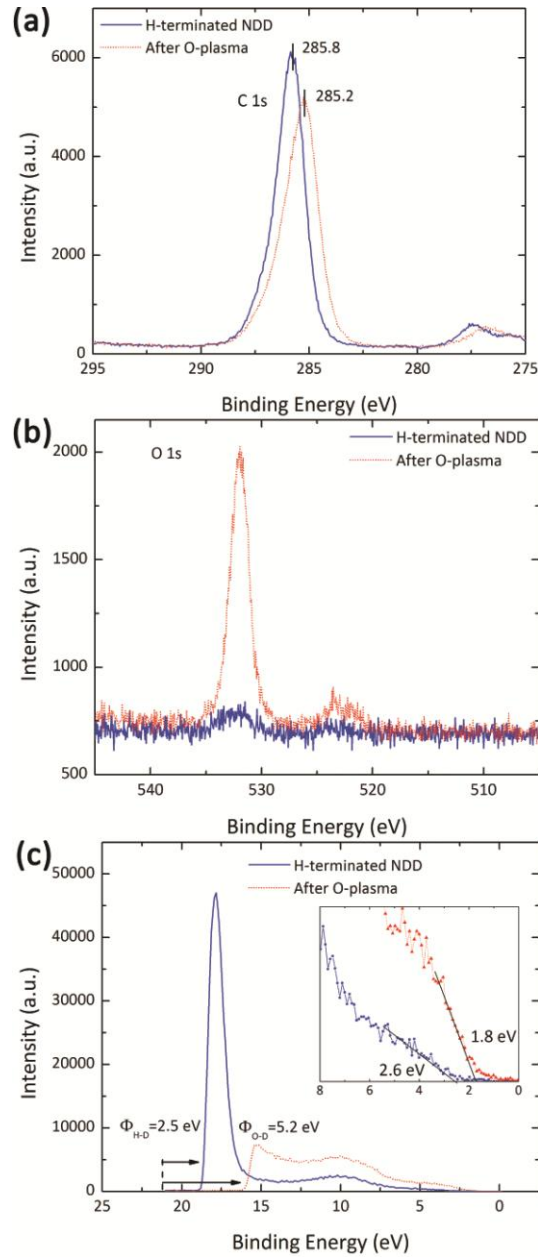


Fig. 6.2 (a) XPS scans of C 1s, (b) O 1s peaks, and (c) UPS scans of a nitrogen-doped diamond film, with H- and O-termination respectively. The results indicate a negative electron affinity on the H-terminated surface and a positive electron affinity on the O-terminated surface. In (c) the E_F relative to low energy cut-off occurs at a binding energy

of 21.2 eV corresponding to the photon energy. The effective work function is the energy from this point to the back cut-off.

6.4.2 Boron-doped diamond (BDD)

Fig. 6.3 (a) shows XPS scans of the vanadium and oxygen core levels, collected from the O-terminated BDD sample before and after vanadium deposition. The $2p_{3/2}$ core level of vanadium can be clearly observed after deposition at 516.2 eV. As the $2p_{3/2}$ peak of vanadium metal is typically positioned at 512-513.5 eV [23], this indicates that vanadium oxide was formed immediately after deposition. The oxygen peak intensity did not show an observable change after deposition, indicating that the oxygen component was unaffected by the deposition process. After thermal annealing at 650 °C for 30 min, the vanadium oxide was found to be thermally stable, as its signal intensity remained at approximately the same value. The oxygen peak intensity, however, was significantly reduced, as excess oxygen was apparently removed during annealing.

Spectra of the carbon 1s core level after each process are shown in Fig. 6.2 (b). A 0.3 eV shift of the C 1s peak towards higher binding energy was observed after vanadium deposition, and the 650 °C thermal annealing restored the peak position to 284.3 eV. Using the 283.1 eV value for the C 1s peak relative to the VBM, after 650 °C annealing the VBM of the BDD sample was deduced to be 1.2 eV below E_F . The measured work function of the BDD sample was approximately 3.8 eV, as indicated in Fig. 6.3 (c). Combined with the VBM position, the results indicate a NEA on the annealed BDD/vanadium-oxide sample, with an observed band gap of $\sim 5.0 \pm 0.2$ eV, which is close to the band gap of the NDD sample obtained in part 6.4.1. While this value is smaller

than the reported value of 5.47 eV for single crystal diamond, it is likely due to band gap reduction from the degenerate doping with an acceptor concentration $[B] > 10^{20} \text{ cm}^{-3}$ [24].

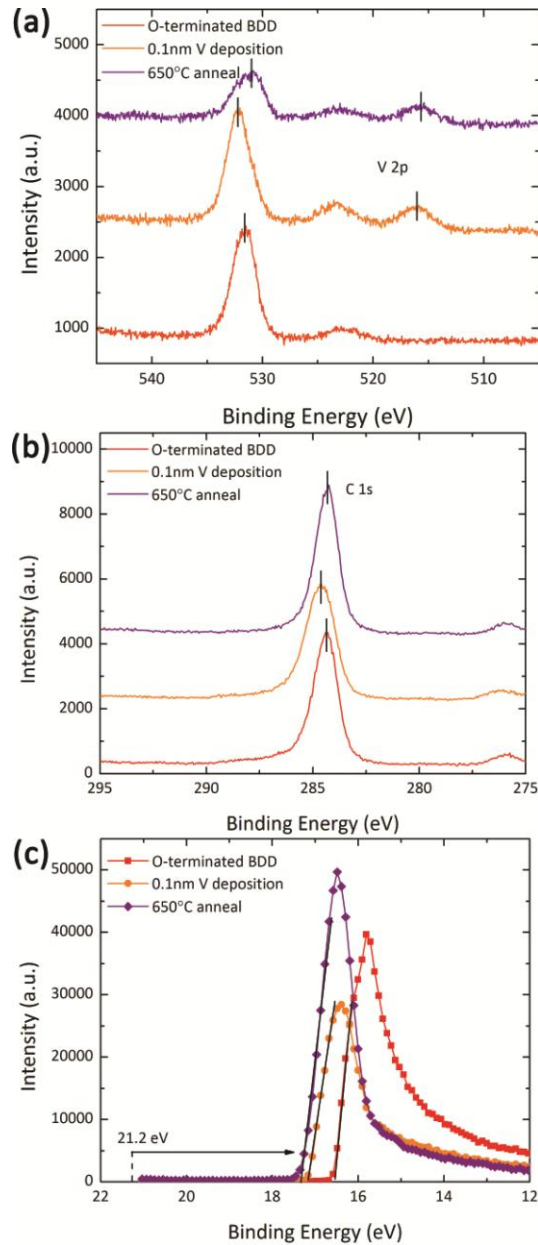


Fig. 6.3 XPS and UPS scans of a boron-doped diamond sample with 0.1 nm V, showing the (a) V 2p_{3/2} and O 1s peaks, (b) C 1s peak, and (c) effective work function after each process.

The measured binding energies of C 1s, O 1s, V 2p_{3/2} core levels and the work function of BDD samples are summarized in Table 6.1.

Table 6.1 C 1s, O 1s, V 2p_{3/2} core levels, effective work function (Φ_w) and electron affinity (EA) for vanadium-oxide-terminated BDD samples. The numbers are in the unit of eV.

| Process | C 1s | O 1s | V2p _{3/2} | Φ_w | EA |
|---------------------|-------|-------|--------------------|----------|-----|
| O-termination | 284.3 | 531.6 | -- | 4.7 | 0.9 |
| Vanadium deposition | 284.6 | 532.1 | 516.2 | 4.1 | 0.6 |
| 650 °C anneal | 284.3 | 531.3 | 515.9 | 3.8 | <0 |

6.4.3 Nitrogen-doped diamond

Spectroscopic results from vanadium-oxide-terminated NDD films are shown in Fig. 6.4, which followed the same procedure as the BDD samples. Several similar characteristics were identified. The vanadium oxide was thermally stable, while the excess oxygen was removed during annealing of the diamond sample. The C 1s core level also shifted in the same direction after the deposition and annealing processes. After 650 °C annealing, the C 1s peak was found at 285.4 eV binding energy. The work function was approximately 3.9 eV after vanadium deposition and annealing. Again, the binding energy difference of 283.1 eV and a band gap of 5.1 eV were used to calculate the electron affinity, which resulted in a PEA of 1.1 ±0.2 eV.

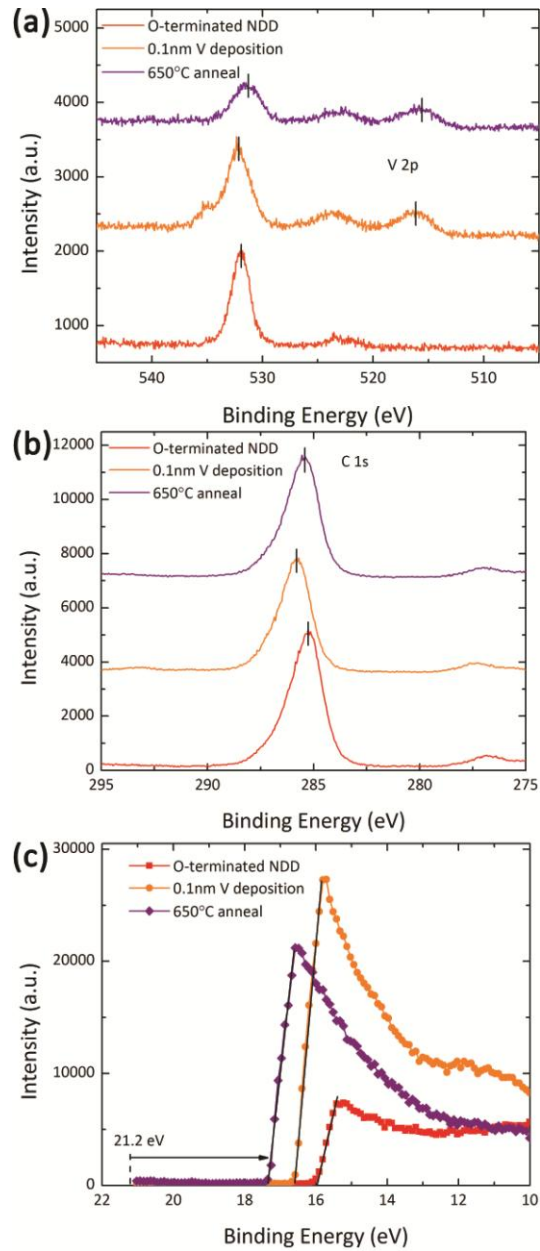


Fig. 6.4 XPS and UPS scans of a nitrogen-doped diamond sample with 0.1 nm V, showing the (a) V 2p_{3/2} and O 1s peaks, (b) C 1s peak, and (c) effective work function after each process.

The measured binding energies of C 1s, O 1s, V 2p_{3/2} core levels and the work function of NDD samples are summarized in Table 6.2.

Table 6.2 C 1s, O 1s, V 2p_{3/2} core levels, effective work function (Φ_w) and electron affinity (EA) for vanadium-oxide-terminated NDD samples. The numbers are in the unit of eV.

| Process | C 1s | O 1s | V 2p _{3/2} | Φ_w | EA |
|---------------------|-------|-------|---------------------|----------|-----|
| O-termination | 285.2 | 532.0 | -- | 5.2 | 1.9 |
| Vanadium deposition | 285.8 | 532.2 | 516.4 | 4.6 | 1.9 |
| 650 °C anneal | 285.4 | 531.4 | 516.0 | 3.9 | 0.8 |

6.5 Discussion

We first examine the properties of the vanadium oxide. Due to the small oxide thickness in this experiment, the weak signal from the V-O bond could not be separated from the main oxygen peak nearby, hence the surface stoichiometry was difficult to determine. The V 2p_{3/2} core level position after thermal annealing was ~ 516 eV, which has been suggested to indicate VO₂ formation [25]. However, the energy difference between the V 2p_{3/2} and O 1s core levels was approximately 15.4 eV, rather than the typical V-O binding energy difference in VO₂, which was found to be ~ 13.7 eV [21]. Fig. 6.5 shows the UPS spectra collected from a BDD sample, on which the vanadium was deposited with an increased thickness of 0.5 nm. A small front cut-off at ~ 0.6 eV below E_F was observed, which is again evidence of VO₂ formation [21], instead of at 0 eV for the metallic V₂O₃ which is metallic at room temperature [26]. Therefore, we argue that the final termination is possibly composed of both VO₂ and V₂O₃. The oxidation during vanadium deposition could arise from both the residual gas in the deposition chamber and the O-termination of the diamond surface.

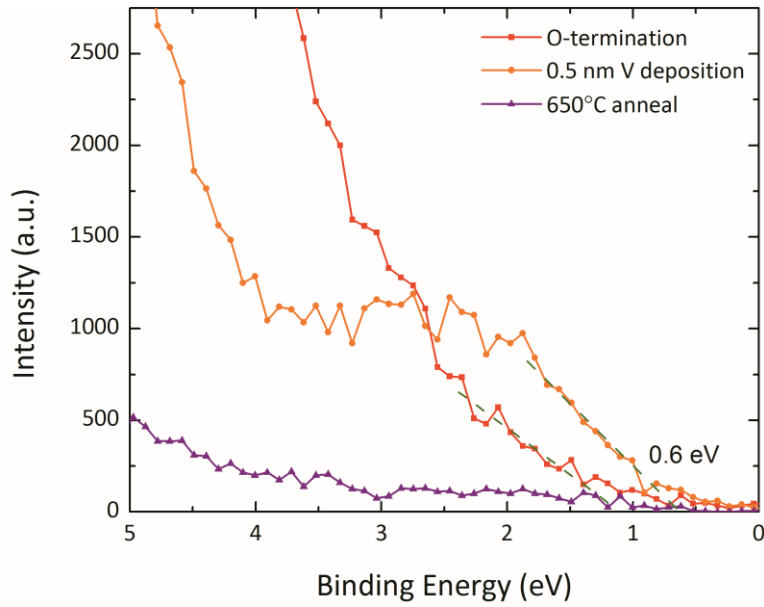


Fig. 6.5 UPS spectra of a BDD sample coated with 0.5 nm V deposition.

After vanadium deposition and oxide formation on both the O-terminated BDD and NDD samples, a 0.3-0.6 eV shift of the carbon 1s peak towards higher binding energy was observed. This could result from changes in band bending at the diamond-oxide interface. On the BDD sample, the bands initially bent downward, and this change indicates increased downward band bending. Conversely, on the NDD sample, this means the initial upward band bending was decreased. As the C 1s spectra shift in the same direction for both samples, it is possible that the formation of vanadium changed the density of defect states at the diamond-oxide interface. Removal of the excess oxygen after thermal annealing appeared to shift the spectra backwards to lower binding energy.

Comparison between the results from BDD and NDD samples indicates an apparent difference: while the vanadium-oxide-termination and thermal annealing decreased the work function for both types of diamond samples, an NEA was only achieved on the BDD sample, while the NDD sample showed a PEA. We argue that this

is possibly due to the interface barrier formed between diamond and vanadium oxide, similar to the results found from previous metal thin films deposited on diamond [11-13]. The band diagrams of vanadium-oxide-termination on both substrates are shown in Fig. 6.6. The bulk Fermi levels in both BDD and NDD samples are assumed to be at the positions of corresponding dopants, i.e. 0.4 eV above VBM for BDD and 1.7 eV below CBM for NDD. Since the bulk Fermi level in the boron-doped (*p*-type) diamond is close to its VBM, the vacuum level of the vanadium oxide is aligned inside the wide bandgap of diamond. Electrons in the diamond conduction band can be emitted through the oxide layer into vacuum directly, and the effective photoemission threshold is decreased. In contrast, for the nitrogen-doped (*n*-type) diamond film, the vacuum level of the vanadium oxide layer is significantly greater than the diamond CBM after aligning the Fermi level. As a result, the barrier formed at the diamond/oxide interface creates a higher photoemission threshold.

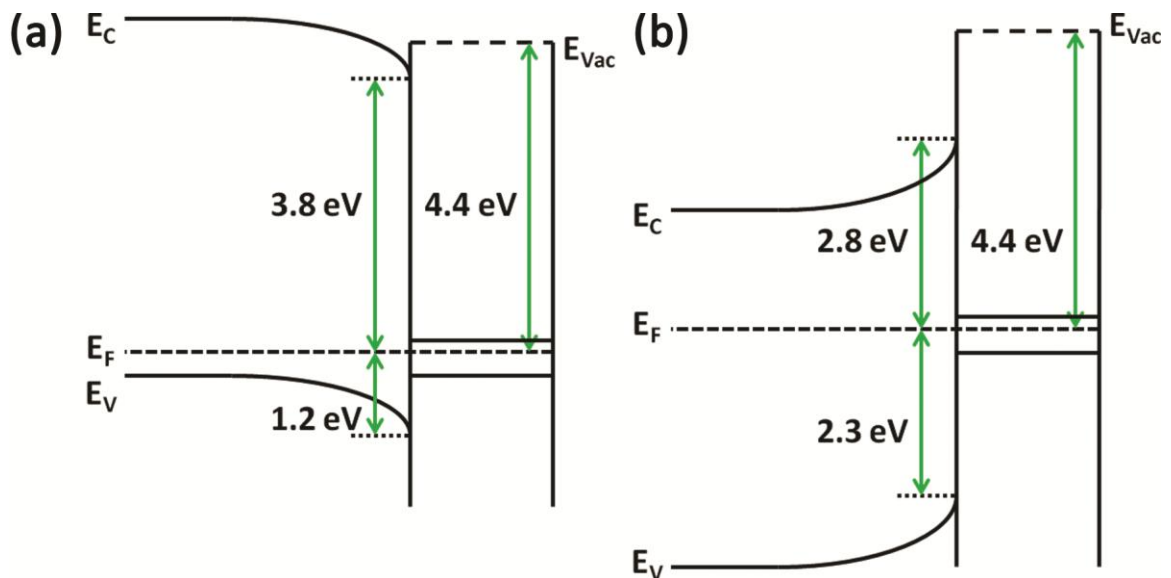


Fig. 6.6 Band schematics of vanadium-oxide-termination on (a) BDD and (b) NDD substrates, assuming a 4.4 eV work function for the vanadium oxide film. On the BDD

sample the vacuum level lies close to the diamond CBM, and leads to a low PEA of 0.6 eV; On the NDD sample, the vacuum level is significantly higher than the diamond CBM, leading to a PEA of 1.6 eV.

It has been reported that the clean surface of sputtered V_2O_3 has a work function of 4.4 eV at ambient temperature [26]. Combined with the measured values of the diamond band positions, a 0.6 eV PEA on the BDD sample and a 1.6 eV PEA on the NDD sample would be expected, as shown in Fig. 6.6. These values however are higher than the experimental results by at least 0.5 eV. The small thickness of vanadium oxide could affect its work function [15].

It should be noted that the valence band offset (VBO) for vanadium oxide on BDD and NDD samples are apparently different in Fig. 6.6., which is possibly due to the effect of band bending on shifting the XPS spectra. As the depletion layer width in a semiconductor is given as:

$$w = \sqrt{\frac{2\varepsilon\varepsilon_0\phi_s}{qN}}, \quad (6.1)$$

where ε is the relative permittivity, ϕ_s the surface potential, and N the dopant concentration. Using $\varepsilon = 5.7$ for the diamond, $N = 10^{20} \text{ cm}^{-3}$, and $\phi_s = 0.8$ and 1.1 eV for BDD and NDD samples respectively, w is deduced to be 2-3 nm, which is smaller than the typically sampling depth of XPS of ~ 5 -10 nm. Therefore the XPS peaks can be shifted due to signals from different depths, and will need to be modified for a more complete analysis.

6.6 Conclusion

Thin layers of vanadium were deposited onto oxygen-terminated, boron-doped and nitrogen-doped diamond samples, and their resulting electronic structures were examined with in-situ XPS and UPS. The vanadium-oxide-termination and thermal annealing decreased the surface work function. A negative electron affinity was observed on the BDD sample, while the NDD sample showed a positive electron affinity. This is possibly due to the difference of the barrier height at the diamond-oxide interface. The results indicate that a thermally stable NEA surface on BDD can be achieved through vanadium-oxide-termination, which leads to possible applications in diamond electron sources for high-temperature devices. For NDD, on the other hand, a lower work function oxide would be required in order to obtain an NEA. Nevertheless, these results show that the work function and electron affinity of a diamond surface can be modified in a controlled way by careful choice of metal oxide termination. To date, only a limited number of metal oxides have been investigated, and our results suggest that studies of the other metal oxides would be worthwhile.

References

- [1] F.J. Himpsel, J.A. Knapp, J.A. VanVechten, D.E. Eastman, "Quantum Photoyield of Diamond (111) - A Stable Negative-Affinity Emitter", *Phys. Rev. B* 20 (1994): 624.
- [2] B.B. Pate, "The Diamond Surface: Atomic and Electronic Structure", *Surf. Sci.* 165 (1986): 83.
- [3] J. van der Weide, Z. Zhang, P.K. Baumann, M.G. Wensell, J. Bernholc, R.J. Nemanich, "Negative-Electron-Affinity Effects on Diamond (100) Surface", *Phys. Rev. B* 60 (1994): 8.
- [4] F.A.M. Koeck, R.J. Nemanich, "Low Temperature Onset for Thermionic Emitters Based on Nitrogen Incorporated UNCD Films", *Diam. Relat. Mater.* 18 (2009): 232-234.

- [5] F.A.M. Koeck, R.J. Nemanich, A. Lazea, K. Haenen, "Thermionic Electron Emission from Low Work-Function Phosphorus Doped Diamond Films", *Diam. Relat. Mater.* 18 (2009): 789-791.
- [6] G.M. Swain, R. Ramesham, "The Electrochemical Activity of Boron-Doped Polycrystalline Diamond Thin Film Electrodes", *Anal. Chem.* 65 (1993): 345-351.
- [7] D. Zhu, L. Zhang, R.E. Ruther, R.J. Hamers, "Photo-Illuminated Diamond as a Solid-State Source of Solvated Electrons in Water for Nitrogen Reduction", *Nat. Mater.* 12 (2013): 836-841.
- [8] A.B. Couto, L.C.D. Santos, J.T. Matsushima, M.R. Baldan, N.G. Ferreira, "Hydrogen and Oxygen Plasma Enhancement in the Cu Electrodeposition and Consolidation Processes on BDD Electrode Applied to Nitrate Reduction", *Appl. Surf. Sci.* 257 (2011): 10141- 10146.
- [9] J.D. Rameau, J. Smedley, E.M. Muller, T.E. Kidd, P.D. Johnson, "Properties of Hydrogen Terminated Diamond as a Photocathode", *Phys. Rev. Lett.* 106 (2011): 137602.
- [10] T. Sun, F.A.M. Koeck, C. Zhu, R.J. Nemanich, "Combined Visible Light Photo-Emission and Low Temperature Thermionic Emission from Nitrogen Doped Diamond Films", *Appl. Phys. Lett.* 99 (2011): 202101.
- [11] J. van der Weide, R. J. Nemanich, "Schottky Barrier Height and Negative Electron Affinity of Titanium on (111) Diamond", *J. Vac. Sci. Technol. B* 10 (1992): 1940.
- [12] P.K. Baumann, S.P. Bozeman, B.L. Ward, R.J. Nemanich, "Characterization of Metal-Diamond Interfaces: Electron Affinity and Schottky Barrier Height", *Diam. Relat. Mater.* 6 (1997): 398-402.
- [13] P.K. Baumann, R.J. Nemanich, "Electron Affinity and Schottky Barrier Height of Metal-Diamond (100), (111), and (110) Interfaces", *J. Appl. Phys.* 83 (1998): 2072.
- [14] K.P. Loh, X.N. Xie, S.W. Yang, J.S. Pan, P. Wu, "A Spectroscopic Study of the Negative Electron Affinity of Cesium Oxide-Coated Diamond (111) and Theoretical Calculation of the Surface Density-Of-States on Oxygenated Diamond (111)", *Diam. Relat. Mater.* 11 (2002): 1379-1384.
- [15] K.M. O'Donnell, T.L. Martin, N.A. Fox, D. Cherns, "Ab Initio Investigation of Lithium on the Diamond C(100) Surface", *Phys. Rev. B* 82 (2010): 115303.
- [16] S. Kono, T. Nohara, S. Abe, H. Kodama, K. Suzuki, S. Koizumi, T. Abukawa, A. Sawabe, "Electron Spectroscopic Determination of Electronic Structures of Phosphorus-Doped N-Type Heteroepitaxial Diamond (001) Surface and Junction", *Jpn. J. Appl. Phys.* 51 (2012): 090109.

- [17] H. Kato, T. Makino, M. Ogura, D. Takeuchi, S. Yamasaki, "Fabrication of Bipolar Junction Transistor on (001)-Oriented Diamond by Utilizing Phosphorus-Doped N-Type Diamond Base", *Diam. Relat. Mater.* 34 (2013): 41-44.
- [18] J.W. Liu, M.Y. Liao, M. Imura, Y. Koide, "Band Offsets of Al₂O₃ and HfO₂ Oxides Deposited by Atomic Layer Deposition Technique on Hydrogenated Diamond", *Appl. Phys. Lett.* 101 (2012): 252108.
- [19] F.J. Morin, "Oxides Which Show a Metal-To-Insulator Transition at the Neel Temperature", *Phys. Rev. Lett.* 3 (1959): 34-36.
- [20] K. Kosuge, "The Phase Diagram and Phase Transition of the V₂O₃-V₂O₅ System", *J. Phys. Chem. Solids.* 28 (1967): 1613-1621.
- [21] C. Zhu, M. Kaur, F. Tang, X. Liu, D.J. Smith, R.J. Nemanich, "Band Alignment of Vanadium Oxide as an Interlayer in a Hafnium Oxide-Silicon Gate Stack Structure", *J. Appl. Phys.* 112 (2012): 084105.
- [22] K. Nakagawa, C. Kajita, N. Ikenaga, M. Nishitani-Gamo, T. Ando, T. Suzuki, "Dehydrogenation of Light Alkanes over Oxidized Diamond-Supported Catalysts in the Presence of Carbon Dioxide", *Catal. Today.* 84 (2003): 149-157.
- [23] J.F. Moulder, W.F. Stickle, P.E. Sobol, K.D. Bomben, *Handbook of X-ray photoelectron spectroscopy* (Waltham: Perkin-Elmer Corporation, 1992).
- [24] A. Deneuville, C. Baron, S. Ghodbane, C. Agnès, "Highly and Heavily Boron Doped Diamond Films", *Diam. Relat. Mater.* 16 (2007): 915-920.
- [25] S. Surnev, M.G. Ramsey, F.P. Netzer, "Vanadium Oxide Surface Studies", *Prog. Surf. Sci.* 73 (2003): 117-165.
- [26] K.E. Smith, V.E. Henrich, "Photoemission Investigation of the Interaction of SO₂ with V₂O₃ Surfaces", *Surf. Sci.* 225 (1990): 47-57.

CHAPTER 7

SUMMARY & FUTURE WORK

7.1 Summary

The research described in this thesis has been focused mostly on the photo-induced and thermionic electron emission from low work function diamond films. The emission characteristics of nitrogen-doped and hydrogen-terminated diamond films have been analyzed through low energy electron spectroscopy, the results of which can be separated into three categories:

Combined photo-induced and thermionic electron emission from nitrogen-doped diamond films on molybdenum substrates has been established, with visible light excitation due to the low work function of these films. The emission mechanism is described in a simplified model of spatially separated generation, which in addition has included the effects of phonon scattering on the energy distribution of emitted electrons. For the first time, low energy photo- and thermal excitation are combined in this emission process on *n*-type doped diamond, and has been the basis for a series of following works.

This combined photo-induced and thermionic emission has been further investigated by comparison between diamond sample sets with different interface and interlayer configurations between the metal substrate and the top N-doped diamond film. The samples have been studied by employing spectroscopy, photoelectron microscopy and optical measurements. Multiple photo-induced emission thresholds have been observed with sub-bandgap photon illumination, which indicates that the quality of the interface can affect the photo-induced electron generation, transition and emission.

Based on the above results associated with principles of photon-enhanced thermionic emission, nitrogen-doped diamond films deposited on silicon substrates have been proposed and studied with electron spectroscopy and transmission electron microscopy. A significant increase of photo-induced electron emission with elevated temperature has been observed and the spectral characteristics differ from those of diamond emitters on metal substrates.

In addition to these three reports, the electronic structure of vanadium-oxide-terminated diamond has been studied using *in-situ* photoelectron spectroscopy. The vanadium-oxide-termination and thermal annealing decreased the surface work function. The difference in the barrier at the diamond-oxide interface has led to different results on diamond sample of different doping types, showing that the electron affinity of a diamond surface can be controlled by careful choice of metal-oxide-termination.

In general, results discussed in this thesis have involved the physical models and the material-related properties of combined photo-induced and thermionic electron emission from low work function diamond films. The results demonstrate the potential applications of diamond-based, integrated devices for combined high efficiency solar and thermal energy conversion, e.g. the concentrated solar cell systems.

7.2 Future work

7.2.1 Photo-emission from phosphorus-doped diamond films

With *n*-type doping and hydrogen termination, diamond can attain a low effective work function. While photo-induced electron emission from nitrogen-doped diamond films has been studied in this work, the phosphorus-doped diamond films remain mostly

unstudied. Being a shallower donor than nitrogen, phosphorus-doping of diamond has been reported to provide the lowest known work function of any non-cesiated material [1]. This proposed project will be focused on the combined photo-induced and thermionic emission from phosphorus-doped diamond grown by microwave plasma enhanced chemical vapor deposition (MPCVD) on different substrate materials (silicon or molybdenum), using phosphine or trimethylphosphine (TMP) as an *in-situ* dopant gas. Following a procedure similar to the study of emission from nitrogen-doped diamond films [2], this project will provide essential information on the emission characteristics, and explore the potential of applying phosphorus-doped diamond in photo-cathode and energy conversion devices.

7.2.2 Diamond-based isothermal PETE converter

Based on the principles recently studied in Ref. [3], this project proposes a multi-layer emitter and collector structure for an isothermal photo-enhanced thermionic energy converter. The emitter structure includes a *p*-type Si substrate and an *n*-type negative electron affinity diamond film to enable electron emission across the vacuum gap. This structure takes advantage of photon-enhanced thermionic emission: the above-bandgap photons are absorbed in the Si substrate and establish an enhanced electron population for emission through the low work function surface of diamond, while sub-bandgap light will be absorbed in the collector for transfer to a heat engine. Additionally, having the emitter and collector at the same temperature can effectively simplify device fabrication and help device optimization.

Modeling the performance of such a device requires combining the physical process with the specific device configuration. Due to the non-negligible reverse emission, an optimized operation regime of the device will be mapped to obtain the maximum conversion efficiency. Further development of this algorithm will also include more precise description of the generation process, and electron transport through the absorber-emitter interface, etc. [4]. Moreover, a detailed model of the recombination process inside the absorbing substrate semiconductor will be required in order to optimize the substrate engineering [5-7]. Including these principles into a single model will provide an effective approach for evaluating the device performance.

7.2.3 Electronic structure of adsorbed molecules on diamond

In a recent study, the performance of a diamond-based thermionic energy converter was shown to be significantly increased by introducing ionized methane molecules into the emitter-collector gap [8]. It was argued that a molecular charge transfer process contributed to the increased current. With the presence of molecules, the thermionic electrons from the emitter can tunnel to the molecular orbitals, and are released at the collector surface, forming an enhanced emission current. The enhancement of thermionic energy conversion using hydrogen molecules is also under investigation, and it appears the formation of atomic H through a hot filament is essential.

Identifying suitable gaseous species for the molecular charge transport process is crucial for understanding the underlying physics and optimizing its effect. UPS systems have been frequently employed to study the surface adsorption of many different materials [9-11]. In this proposed research, we will study the change of surface electronic

states of NEA diamond during molecular adsorption, through dosing the diamond surface with different gas molecules and measure the corresponding photoelectron spectra.

7.2.4 Space-charge limitation of diamond photo-cathodes

Space-charge limited current is considered one of the main challenges in devices employing electron emission, where the emitted electrons between the emitter and collector screen each other and reduce the emitter efficiency. As strong emissivity of NEA diamond has been observed under visible light illumination, it has the potential to be applied as a photo-cathode. Several simulation methods have been used for analyzing the space-charge region of metallic photo-cathodes, mostly aimed at modeling the electron dynamics from a laser pulse [12-14]. However, modifications to semiconductor materials with NEA surfaces have not been considered at this time.

In recent years a model based on the Langmuir theory has been suggested for NEA diamond thermionic emitters in an energy conversion device [15]. This motivates us to propose a study, first on developing a quasi computer-based model for estimating the output characteristics of a diamond-based photo-cathode, on a quasi-equilibrium basis. As photo-electrons generated from a photo-cathode can possibly form a complex energy distribution away from such basis, a more complete approach is to employ the particle-in-a-cell (PIC) simulation [16] to analyze the strong non-equilibrium and kinetic behavior in the space charge region.

Experimentally, the diamond-based photo-cathodes can be tested through different methods, e.g. the shadow projection imaging technique [14]. The quantum efficiency of photoemission from the diamond films will need to be determined through

precise measurements. Comparison between modeling experimental results will help identifying the characteristics of space-charge region and help understanding its effects.

7.2.5 Photoelectrochemistry with *n*-type diamond electrodes

Photoelectron generation from NEA diamond has been applied in electrochemistry applications [17-19] due to its chemical inertness, high compatibility to bond with organic molecules, and strong electron emissivity. The wide bandgap of diamond, however, has limited the photon energy required for excitation. These reactions have been executed typically under UV light illumination, the optical absorption of which in the solution can be significant, adding limitations on suitable reaction species.

With significant results concerning thermionic and photoelectron emission of nitrogen-doped diamond films in ultra-high vacuum being achieved in this thesis, it is possible to exploit these low work function diamond films and enhance the electrochemical reaction in the presence of visible light photons, aiming at higher efficiency and broader applications.

The work proposed here will investigate electrochemical properties of these films, and at the same time further explore their photoemission properties in a liquid environment. The experimental step will examine Ag and Cu deposition onto the diamond surface through an applied bias voltage and light exposure to utilize the photoelectrons in nitrate or sulfate reduction reactions. Microscopic imaging (SEM, AFM, etc.) can also be employed to document the spatial distribution of the deposition.

References

- [1] F.A.M. Koeck, R.J. Nemanich, A. Lazea, K. Haenen, "Thermionic Electron Emission from Low Work-Function Phosphorus Doped Diamond Films", *Diam. Relat. Mater.* 18 (2009): 789-791.
- [2] T. Sun, F.A.M. Koeck, C. Zhu, R.J. Nemanich, "Combined Visible Light Photo-Emission and Low Temperature Thermionic Emission from Nitrogen Doped Diamond Films", *Appl. Phys. Lett.* 99 (2011): 202101.
- [3] G. Segev, A. Kribus, Y. Rosenwaks, "High Performance Isothermal Photo-Thermionic Solar Converters", *Sol. Energ. Mat. Sol. C.* 113 (2013): 114-123.
- [4] J.W. Schwede, T. Sarmiento, V.K. Narasimhan, S.J. Rosenthal, D.C. Riley, F. Schmitt, I. Bargatin, K. Sahasrabudhe, R.T. Howe, J.S. Harris, N.A. Melosh, Z.-X. Shen, "Photon-Enhanced Thermionic Emission from Heterostructures with Low Interface Recombination", *Nat. Commun.* 4 (2013): 1576.
- [5] A. Varpula, M. Prunnila, "Diffusion-Emission Theory of Photon Enhanced Thermionic Emission Solar Energy Harvesters", *J. Appl. Phys.* 112 (2012): 044506.
- [6] K. Sahasrabudhe, J.W. Schwede, I. Bargatin, J. Jean, R.T. Howe, Z.-X. Shen, N.A. Melosh, "A Model for Emission Yield from Planar Photocathodes Based on Photon-Enhanced Thermionic Emission or Negative-Electron-Affinity Photoemission", *J. Appl. Phys.* 112 (2012): 094907.
- [7] G. Segev, Y. Rosenwaks, A. Kribus, "Loss Mechanisms and Back Surface Field Effect in Photon Enhanced Thermionic Emission Converters", *J. Appl. Phys.* 114 (2013): 044505.
- [8] F.A.M. Koeck, R.J. Nemanich, Y. Balasubramaniam, K. Haenen, J. Sharp, "Enhanced Thermionic Energy Conversion and Thermionic Emission from Doped Diamond Films Through Methane Exposure", *Diam. Relat. Mater.* 20 (2011): 1229-1233.
- [9] J. Günster, G. Liu, V. Kempter, D.W. Goodman, "Adsorption of Benzene on Mo(100) and MgO(100)/Mo(100) Studied by Ultraviolet Photoelectron and Metastable Impact Electron Spectroscopies", *Surf. Sci.* 415 (1998): 303-311.
- [10] J.P. Chamberlain, J.L. Clemons, A.J. Pounds, H.P. Gillis, "Adsorption of CO on Si (100)-(2×1) at Room Temperature", *Surf. Sci.* 301 (1994): 105-117.
- [11] Y.K. Kim, M.H. Lee, H.W. Yeom, "Coverage-Dependent Adsorption Behavior of Benzene on Si(100): A High-Resolution Photoemission Study", *Phys. Rev. B* 71 (2005): 115311.
- [12] L. Martina, V. Nassisi, A. Pedone, P. P. Pompa, G. Raganato, "Studies of Electron Beams Propagation in Space-Charge Regime", *Rev. Sci. Instrum.* 73 (2002): 2552.

- [13] W. Wendelen, B. Y. Mueller, D. Auriq, B. Rethfeld, A. Bogaerts, "Space Charge Corrected Electron Emission from an Aluminum Surface Under Non-Equilibrium Conditions", *J. Appl. Phys.* 111 (2012): 113110.
- [14] Z. Tao, H. Zhang, P.M. Duxbury, M. Berz, C.-Y. Ruan, "Space Charge Effects in Ultrafast Electron Diffraction and Imaging", *J. Appl. Phys.* 111 (2012): 044316.
- [15] J.R. Smith, G.L. Bilbro, R.J. Nemanich, "Theory of Space Charge Limited Regime of Thermionic Energy Converter with Negative Electron Affinity Emitter", *J. Vac. Sci. Technol. B* 27 (2009): 1132-1141.
- [16] C. K. Birdsall, "Particle-In-Cell Charged Particle Simulations, plus Monte Carlo Collisions with Neutral Atoms", *IEEE Trans. Plasma Sciences*, 19 (1991): 65.
- [17] A.Y. Sakharava, Y.V. Pleska, F. Di Quarto, S. Piazza, C. Sunseri, I.G. Teremetskaya, V.P. Varnin, "Synthetic Diamond Electrodes: Photoelectrochemical Investigation of Undoped and Boron-Doped Polycrystalline Thin Films", *J. Electrochem. Soc.* 142 (1995): 2704.
- [18] D. Zhu, L. Zhang, R.E. Ruther, R.J. Hamers, "Photo-Illuminated Diamond as a Solid-State Source of Solvated Electrons in Water for Nitrogen Reduction", *Nat. Mater.* 12 (2013): 836-841.
- [19] A.B. Couto, L.C.D. Santos, J.T. Matsushima, M.R. Baldan, N.G. Ferreira, "Hydrogen and Oxygen Plasma Enhancement in the Cu Electrodeposition and Consolidation Processes on BDD Electrode Applied to Nitrate Reduction", *Appl. Surf. Sci.* 257 (2011): 10141-10146.

REFERENCES

- F.J. Himpsel, et. al., *Phys. Rev. B* 20 (1994): 624.
- J. van der Weide, et. al., *Phys. Rev. B* 60 (1994): 8.
- B.B. Pate, et. al., *J. Vac. Sci. Technol.* 21 (1982): 364.
- B.B. Pate, *Surf. Sci.* 165 (1986): 83.
- J.B. Cui, et. al., *Phys. Rev. Lett.* 81 (1998): 429-432.
- D. Takeuchi, et. al., *Appl. Phys. Lett.* 86 (2005): 152103.
- F. Maier, et. al., *Phys. Rev. B* 64 (2001): 165411.
- T. Haensel, et. al., *Phys. Status Solidi A* 206 (2009): 2022-2027.
- R.E. Thomas, et. al., *J. Vac. Sci. Technol. A* 10 (1992): 2451.
- J. van der Weide, et. al., *J. Vac. Sci. Technol. B* 10 (1992): 1940.
- P.K. Baumann, et. al., *Diam. Relat. Mater.* 6 (1997): 398-402.
- P.K. Baumann, et. al., *J. Appl. Phys.* 83 (1998): 2072.
- K.P. Loh, et. al., *Diam. Relat. Mater.* 11 (2002): 1379-1384.
- K.M. O'Donnell, et. al., *Phys. Rev. B* 82 (2010): 115303.
- K. Thonke, *Semicond. Sci. Technol.* 18 (2003): S20-S26.
- R.G. Farrer, *Solid State Commun.* 7 (1969): 685-688.
- S. Koizumi, et. al., *Appl. Phys. Lett.* 71 (1997): 1065.
- K. Haenen, et. al., *Diam. Relat. Mater.* 10 (2001): 439-443.
- A.T. Collins, *J. Phys.: Condens. Matter.* 14 (2002): 3743.
- L. Diederich, et. al., *Surf. Sci.* 418 (1998): 219-239.
- O.A. Williams, *Diam. Relat. Mater.* 20 (2011): 621-640
- S. Bhattacharyya, *Phys. Rev. B* 70 (2004): 125412.
- F.A.M. Koeck, et. al., *Diam. Relat. Mater.* 18 (2009): 232-234.

- F.A.M. Koeck, et. al., *Diam. Relat. Mater.* 18: (2009): 789-791.
- O.W. Richardson, *Phys. Rev.* 23 (1924): 153.
- S. Dushman, *Rev. Mod. Phys.* 2 (1930): 381.
- V.S. Fomenko, *Handbook of Thermionic Properties: Electronic Work Functions and Richardson Constants of Elements and Compounds* (New York: Springer, 1966).
- N.S. Rasor, *J. Appl. Phys.* 31 (1960): 163.
- H.F. Webster, *J. Appl. Phys.* 30 (1959): 488.
- I.P. Bogush, et. al., *Sov. At. Energy* 70 (1991): 263-266.
- Committee on Thermionic Research and Technology, Aeronautics and Space Engineering Board, National Research Council. *Thermionics Quo Vadis? An Assessment of the DTRA's Advanced Thermionics Research and Development Program* (Washington, D.C.: National Academies Press, 2001).
- W.M. Haynes, *CRC Handbook of Chemistry and Physics, 94th edition* (Boca Raton: CRC Press, 2013-2014).
- J.L. Coggins, et. al., *Surf. Sci.* 11 (1968): 355-369.
- M. Suzuki, et. al., *Diam. Relat. Mater.* 18 (2009): 1274-1277.
- Y.M. Wong, et. al., *Diam. Relat. Mater.* 18 (2009): 563-566.
- K. Uppireddi, et. al., *J. Appl. Phys.* 106 (2009): 043716.
- M. Kataoka, et. al., *Diam. Relat. Mater.* 19 (2010): 110-113.
- F.A.M. Koeck, et. al., *J. Appl. Phys.* 112 (2012): 113707.
- F.A.M. Koeck, et. al., *Diam. Relat. Mater.* 20 (2011) 1229-1233.
- T.D. Musho, et. al., *J. Vac. Sci. Technol. B* 31 (2013): 021401.
- W.F. Paxton, et. al., *J. Vac. Sci. Technol. B* 30 (2012): 021202.
- G. Hatsopoulos, et. al., *Thermionic Energy Conversion* (Cambridge: MIT Press, 1973).
- J.R. Smith, et. al., *Diam. Relat. Mater.* 15 (2006): 2082-2085.
- J.R. Smith, et. al., *Phys. Rev. B* 76 (2007): 245327.
- J.R. Smith, et. al., *J. Vac. Sci. Technol. B* 27 (2009): 1132-1141.

J.R. Smith, *J. Appl. Phys.* 114 (2013)" 164514.

J.-H. Lee, et. al., *Appl. Phys. Lett.* 100 (2012): 173904.

K.A. Littau, et. al., *Phys. Chem. Chem. Phys.* 15 (2013): 14442.

W.E. Spicer, *Phys. Rev.* 112 (1958): 114-122.

R.H. Fowler, *Phys. Rev.* 38 (1931): 45.

L.A. DuBridg, *Phys. Rev.* 43 (1933): 727-741.

K.L. Jensen, et. al., *Appl. Phys. Lett.* 89 (2006): 224103.

N.B. Kindig, et. al., *Phys. Rev.* 138 (1965): A561-576.

R.J. Powell, *J. Appl. Phys.* 41 (1970): 2424-2432.

V.G. Tkachenko, et. al., *Appl. Phys. B* 98 (2010): 839-849.

C. Bandis, et. al., *Surf. Sci.* 350 (1996): 315-321.

J.B. Cui, et. al., *Phys. Rev. B.* 60 (1999): 16135-16142.

R.J. Nemanich, et. al., *Appl. Surf. Sci.* 146 (1999): 287-294.

F.A.M. Koeck, et. al., *Diam. Relat. Mater.* 12 (2003): 474-480.

S. Kono, et. al., *Surf. Sci.* 604 (2010): 1148-1165.

J.B. Cui, et. al., *Diam. Relat. Mater.* 9 (2000): 1143-1147.

D. Takeuchi, et. al. *Phys. Stat. Sol. (a)* 203 (2006): 3100-3106.

A.Y. Sakharava, et. al., *J. Electrochem. Soc.* 142 (1995): 2704.

B.M. Nichols, et. al., *J. Phys. Chem. B* 109 (2005): 20938-20947.

D. Zhu, et. al., *Nat. Mater.* 12 (2013): 836-841.

A.B. Couto, et. al., *Appl. Surf. Sci.* 257 (2011): 10141-10146.

J.D. Rameau, et. al., *Phys. Rev. Lett.* 106 (2011): 137602

M. Niigaki, et. al., US patent 7045957, filed Aug 20, 2002, and issued May 16, 2006.

T.L. Westover, et. al., *J. Vac. Sci. Technol. B* 28 (2010): 423-434.

P. Yaghoobi, et. al., *Solid State Commun.* 151 (2011): 1105-1108.

M.V. Moghaddam, et. al., *Appl. Phys. Lett.* 101 (2012): 253110.

P. Yaghoobi, et. al., *AIP Adv.* 2 (2012): 042139.

P.T. McCarthy, et. al., *J. Appl. Phys.* 113 (2013): 193710.

G.P. Smestad, *Sol. Energ. Mat..Sol. C.* 82 (2004): 227-240.

J.W. Schwede, et. al., *Nat. Mater.* 9 (2010): 762-767.

S. Su, et. al., *Sol. Energ. Mat. Sol. C.* 117 (2013): 219-224.

A. Asgari, et. al., *Sol. Energ. Mat. Sol. C.* 95 (2011): 3124-3129.

A. Varpula, et. al., *J. Appl. Phys.* 112 (2012): 044506.

G. Segev, et. al., *J. Appl. Phys.* 114 (2013): 044505.

K. Sahasrabudde, et. al., *J. Appl. Phys.* 112 (2012): 094907.

Y. Yang, et. al., *Appl. Phys. Lett.* 103 (2013): 083902.

T. Ito, et. al., *Appl. Phys. Lett.* 101 (2012): 213901.

G. Segev, et. al., *Sol. Energ. Mat. Sol. C.* 113 (2013): 114-123.

J.W. Schwede, et. al., *Nat. Commun.* 4 (2013): 1576.

S. Hüfner, et. al., *Nucl. Instrum. Meth. A* 547 (2005): 8-23.

D. Briggs, *Handbook of X-ray and ultraviolet photoelectron spectroscopy* (Heyden, 1977).

J.F. Moulder, et. al., *Handbook of X-ray photoelectron spectroscopy* (Waltham: Perkin-Elmer Corporation, 1992).

C. J. Humphreys, et. al., *J. Opt. Soc. Am.* 60 (1970): 1302.

Y.M. Wong, et. al., *Diam. Relat. Mater.* 18 (2009): 563-566.

K. Uppireddi, et. al., *J. Appl. Phys.* 106 (2009): 043716.

O. Groning, et. al., *Solid State Electron.* 45 (2001): 929-944.

J.E. Yater, et. al., *J. Appl. Phys.* 87 (2000): 8103-8112.

J.W. Gadzuk, et. al., *Rev. Mod. Phys.* 45 (1973): 487-548.

P. Wurz, et. al., *Surf. Sci.* 373 (1997): 56-66.

T. Sun, et. al., *Appl. Phys. Lett.* 99 (2011): 202101.

N. Neugebohrn, et. al., *Diam. Relat. Mater.* 40 (2013): 12-16.

G.E. Jellison, et. al., *J. Appl. Phys.* 76 (1994): 3758.

G.M. Swain, et. al., *Anal. Chem.* 65 (1993): 345-351.

F.J. Morin, *Phys. Rev. Lett.* 3 (1959): 34-36.

K. Kosuge, *J. Phys. Chem. Solids.* 28 (1967): 1613-1621.

C. Zhu, et. al., *J. Appl. Phys.* 112 (2012): 084105.

K. Nakagawa, et. al., *Catal. Today.* 84 (2003): 149-157.

A. Deneuve, et. al., *Diam. Relat. Mater.* 16 (2007): 915-920.

S. Surnev, et.al., "*Prog. Surf. Sci.* 73 (2003): 117-165.

K.E. Smith, et. al., *Surf. Sci.* 225 (1990): 47-57.

J. Günster, et. al., *Surf. Sci.* 415 (1998): 303-311.

J.P. Chamberlain, et. al., *Surf. Sci.* 301 (1994): 105-117.

Y.K. Kim, et. al., *Phys. Rev. B* 71 (2005): 115311.

L. Martina, et. al., *Rev. Sci. Instrum.* 73 (2002): 2552.

W. Wendelen, et. al., *J. Appl. Phys.* 111 (2012): 113110.

Z. Tao, et. al., *J. Appl. Phys.* 111 (2012): 044316.

C. K. Birdsall, *IEEE Trans. Plasma Sciences*, 19 (1991): 65.

APPENDIX A

SPATIAL CORRELATION OF PHOTO-INDUCED AND THERMIONIC ELECTRON
EMISSION FROM LOW WORK FUNCTION DIAMOND FILMS

This appendix includes results of a study that was directly motivated by the contents of Chapter 3, which served as a partial fulfillment of the requirements for the Master's degree, earned by Nils Neugebohrn in 2012, of University of Bremen. The author of this thesis has participated in conducting the experiments, data analysis and writing of this article, and would like to include it as an appendix to incorporate with Chapter 3 and 4.

A.1 Abstract

Hydrogen terminated, nitrogen doped diamond thin films have been the focus of recent research for application in thermionic energy conversion devices and possibly in solar cells. Nitrogen doped diamond films can attain negative electron affinity (NEA) through treatment with hydrogen plasma, which also produces a very low work function surface. Photoemission and thermionic emission spectroscopy measurements confirm a work function of approximately 2 eV for such films. The research presented here includes results from imaging these thin films with photo-electron emission microscopy (PEEM) and thermionic electron emission microscopy (ThEEM), in addition to spectroscopic studies using ultraviolet photoelectron spectroscopy (UPS). From the images it can be concluded that the photo- and thermionic emission are spatially uniform and do not originate from different isolated emission sites. This observation holds true up to the highest resolution and for all temperatures investigated (300-800 K). While relatively uniform, the emission is found to be influenced by the surface morphology and film microstructure. The spatial intensity distributions of the PEEM and ThEEM images are very similar, as reflected by the structure present in both of these images. This

observation indicates that both emission processes are enabled by the low work function of the film.

A.2 Introduction

Thermionic electron emission from semiconductor materials (e.g. diamond films) has been under investigation for its application in energy conversion devices [1-3]. Among the outstanding attributes of diamond films are their high electric and thermal conductivity, stability, and the ability to attain a negative electron affinity (NEA) surface through hydrogen termination [4]. As low-temperature thermionic electron emission from doped diamond films has been achieved in recent years [5-7], these films are now of interest for thermionic energy conversion applications.

Photo-electron emission microscopy (PEEM), thermionic electron emission microscopy (ThEEM), and field electron emission microscopy (FEEM) have been employed broadly for imaging the spatial distribution of electron emission from diamond materials [8-14]. The *n*-type doping and NEA are critical for diamond materials to achieve a low work function. However, for nitrogen-doping of single crystal samples this condition has been difficult to attain due to significant upward band bending [15, 16], which shifts the relative position of the Fermi level in the band gap. Consequently the surfaces may exhibit an effective work function greater than 4.5 eV, and PEEM imaging typically requires a photon energy above the band gap of diamond (5.5 eV) for excitation.

Recently low-work-function *n*-type doped diamond films have been grown by incorporating sp^2 bonded grain boundaries, which can apparently provide sufficient electrons to compensate the empty surface states. Work functions of 1.3 eV with nitrogen

doping [3] and 0.9 eV with phosphorus doping [17] have been measured. Such work functions make imaging diamond films with long wavelength UV or visible light not only possible but also crucial for understanding the emission mechanism. This report is focused on the relative properties of photo-induced emission and thermionic emission from these low work function, nitrogen-doped diamond NEA films. In this paper results of PEEM / ThEEM imaging and low energy electron spectroscopy are presented in an effort to determine if the same low work function applies for both thermionic emission and photoemission, by investigating the spatial correlation of the two types of emission.

A.3 Experimental

The samples used for this study were produced by growing nitrogen doped diamond films on polished metal (molybdenum) substrates using plasma enhanced chemical vapor deposition (PECVD) at Arizona State University. Prior to growth the surface was sonicated in a nano-diamond slurry for 40 min, then rinsed with acetone and dried with nitrogen gas. This nucleation step was followed by the deposition of a nitrogen-incorporated ultra-nano crystalline diamond ((N)UNCD) layer and then N-doped diamond. The UNCD layer was deposited using 10 sccm argon, 100 sccm nitrogen and 20 sccm methane. The N-doped diamond layer deposition employed hydrogen at 400 sccm, methane at 2 sccm, and nitrogen at 40 sccm. An NEA surface was produced by cooling the sample in a hydrogen plasma. After producing multiple samples with different growth parameters, we were able to prepare a set of samples under similar conditions which met the requirements for both emission microscopy and photoemission spectroscopy. The thicknesses of the films were in the range of 440 ± 25 nm. The main

challenge was to reduce the surface roughness in order to avoid field emission in the electron microscope while maintaining a low effective work function similar to those achieved in previous studies [3].

PEEM and ThEEM images were acquired with an Elmitec LEEM III instrument [18]. During heating of the sample the temperature was monitored with a thermocouple, while the pressure did not exceed 10^{-9} Torr. In the experiment a strong field is applied to the sample to accelerate the emitted electrons into the imaging column of the instrument. At the standard acceleration voltage of 20 kV, considerable field emission was observed from our samples. Therefore, the microscope was operated at 10 kV for the experiments discussed here. The standard sample to anode distance was about 2.5 mm, corresponding to an electric field $\sim 4 \times 10^6$ V/m. The specific local field varies due to the morphology of the sample surface. At this reduced voltage the field emission intensity was kept below the random noise level. Prior to observation the samples were heated to 400 °C for 15 minutes inside the microscope vacuum chamber to remove surface contamination. A mercury arc lamp equipped with band pass filters was employed as the light source for photo-excitation. A microchannel plate electron multiplier coupled to a phosphor screen and a CCD-camera served as the detection system. The emission images with and without photo-excitation were recorded from ambient temperature up to 530 °C.

In order to investigate the surface structure of the diamond samples at higher resolution than was available from the PEEM, complementary scanning electron microscopy (SEM; done with a FEI Nova 200 NanoLab instrument) and atomic force microscopy (AFM; using an Autoprobe CP from Park Scientific Instruments) measurements were conducted at the University of Bremen.

Ultraviolet photoelectron spectroscopy (UPS) has been broadly applied to determine the effective work function of diamond [4,6,13]. In the present spectroscopy study, photo- and thermionic emission spectra of the diamond sample were recorded with a VSW HA50 hemispherical spectrometer with 0.15 eV resolution, operating in a 10^{-9} Torr vacuum. During the experiment, radiation heating was provided by a tungsten coil beneath the sample. The temperature was monitored with a thermocouple also located behind the center of the sample, which had been calibrated with a pyrometer. The UV sources included 21.2 eV light from a He I discharge and a focused Xe arc lamp used with bandpass filters to provide 2 to 4 eV photons. The photoemission spectra are referenced to the Fermi level (E_F) of the metallic sample holders, which is calibrated with a standard gold sample by extrapolating the kinetic energy cut-off to the baseline intensity.

A.4 Results and Discussion

The SEM images of the diamond surface shown in Fig. A.1 display parallel lines of varying size and contrast, possibly reflecting the morphology of the mechanically polished substrate. These parallel lines are apparently composed of small bumps. At higher magnification, as shown in the inset, the surface morphology is further resolved to consist of shard-like structures which reside on top of the larger structures. Due to the limited resolution of the AFM used here, these shard-like structures are not resolved in the image shown on the right-hand side of Fig. A.1. However, this AFM image reveals that the line-and-bump contrast observed with SEM indeed corresponds to the surface morphology. The bumps have been observed in a previous study [19] and are typical of

polycrystalline CVD diamond films [20] due to local variations in diamond nucleation. The anisotropy represented by the line structure can neither be attributed to the crystal structure nor to the CVD growth process. Most likely, it is due to scratches in the metal substrate generated by mechanical polishing, as presented on the image of a bare substrate.

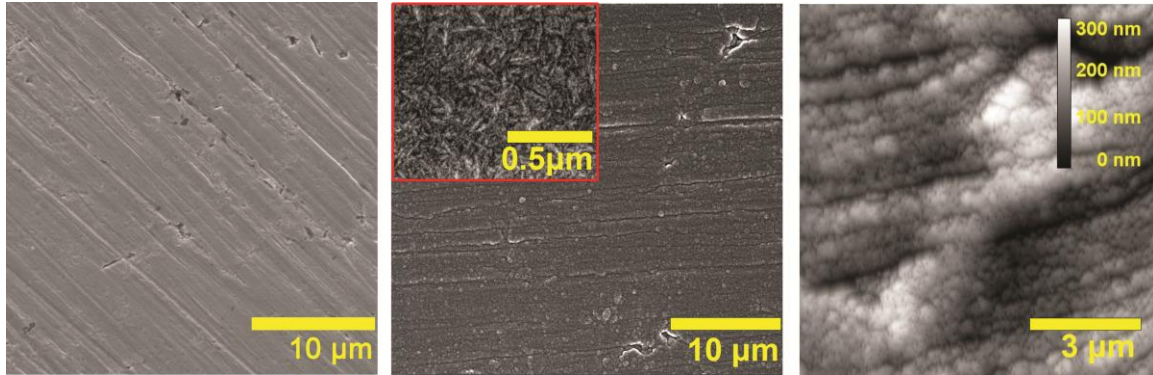


Fig. A.1 SEM images of the polished molybdenum substrate (left) and the N-doped diamond film surface (middle), and AFM (right) image of the diamond film. All images display similar line structures which are attributed to polishing induced scratches of the substrate.

The primary motivation of this study is based on a previous publication from our group, which reported visible light photoemission from diamond emitters of the same structure as studied here [21]. Based on these prior results, the conclusion was drawn that photo-excitation originates at or near the diamond-metal interface as a result of the transparency of the diamond film, while thermionic emission is induced near the sample surface due to thermal ionization of the donors. To characterize the emission properties of the samples used in this study, the photoemission and thermionic spectra were measured and are shown in Fig. A.2. Photoemission was excited with 400 nm light at a sample

temperature of 382 °C. The spectra were recorded with the light on (total emission) and light off (thermionic emission). Subtracting the second spectrum from the first gives the photo-induced emission at this temperature. The thermionic and photo-induced emission are of similar intensity in these experimental results, displayed in Fig. A.2 (a). Focusing on the photo-induced component, Fig. A.2 (b) shows photoemission spectra collected with different photon energies (2.7 to 21.2 eV) at ambient temperature (25 °C).

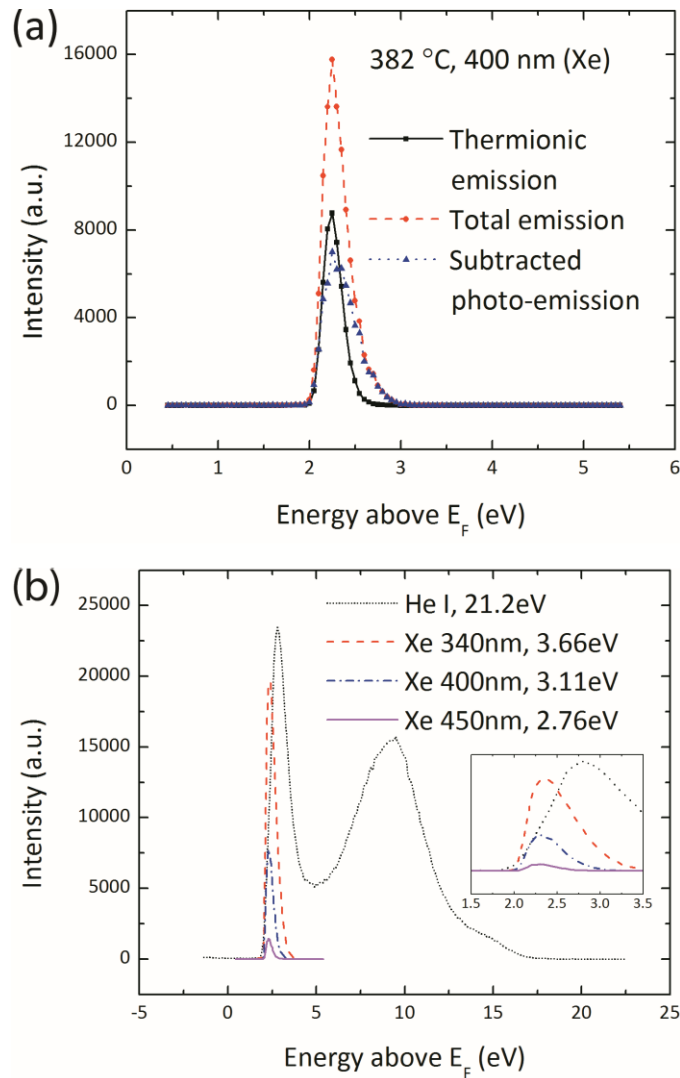


Fig. A.2 (a) Combined photoemission and thermionic emission spectra at 382 °C and 400 nm illumination. Subtracting the thermionic emission spectrum from the total emission

provides the photoemission component. (b) Emission spectra from different illuminating photon energies, measured at ambient temperature. The inset displays the variable excitation energy results near the emission threshold on an expanded energy scale.

All of these spectra (thermionic emission, 400 nm high-temperature photoemission, and UV/visible and 21.2 eV photoemission) share the same low energy cut-off at about 2 eV above the Fermi level, which represents the effective work function, Φ_{eff} , of the sample. Since we presume that the visible light photoemission from these diamond films takes place at the diamond-metal interface, the UPS results imply that neither this interface nor the diamond layers produce an additional barrier higher than Φ_{eff} , so that both photoemission and thermionic emission are limited by the surface energy barrier Φ_{eff} .

A series of PEEM and ThEEM images were recorded between room temperature and 530 °C in order to investigate and compare the spatial intensity distribution and average intensity of both emission types at varying temperatures. To acquire comparable data in each type of image, the sample was first heated to the desired temperature point and then both images were recorded immediately: one after another at the same magnification. This ensured that both images were made under the same conditions, e.g. the same temperature and at the same spot on the sample. At sufficiently elevated temperatures, the PEEM image includes both photo-induced emission and thermionic emission. The average intensity was obtained for each image by subtracting the background and taking a digital average over the largest square area that would fit within the field of view. This value was then normalized to intensity levels per second by dividing by the dwell time of the image. Since the digital levels produced by the CCD

camera are actually representing voltages measured from the charge accumulation capacitors on the chip, we cannot speak of counts per second as we would in a pulse counting system. The detector chain (microchannel plate electron multiplier, phosphor screen and CCD camera) behaved linearly during the relevant time frames. The pure photoemission intensity at each temperature was obtained by subtracting the average of the ThEEM image from the average of the PEEM image.

In Fig. A.3 the average intensity for both the photoemission (under 336 nm illumination) and thermionic emission is plotted on a logarithmic scale versus temperature. The photoemission intensity is essentially constant and does not show any temperature dependence within the temperature range investigated here. However, the thermionic emission was observed to increase exponentially and follow the temperature dependence described by the Richardson-Dushman equation. The thermionic data was fit by this equation using a work function of 2.0 eV, as suggested by the UPS results, and varying the amplitude for lowest residual. This varied amplitude is the product of the Richardson constant of the sample and the collection efficiency of the PEEM system (detector gain per ampere). The photoemission intensity was fit using the Fowler-DuBridge equation, again with a work function of 2.0 eV, and the amplitude was varied to fit the data. Here the amplitude is a function of the Richardson constant, the photoelectric absorption factor and the collection efficiency [2].

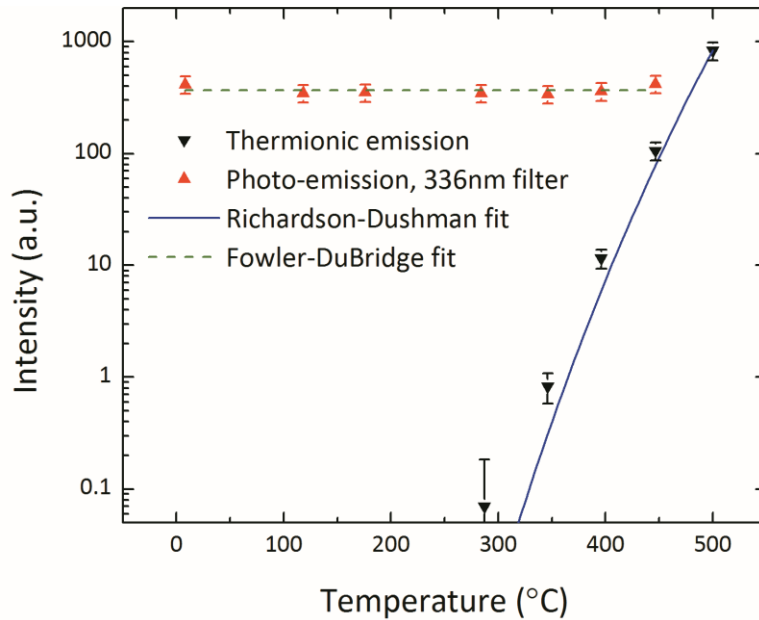


Fig. A.3 Photoemission and thermionic emission average image intensity versus temperature, collected for 50 μm FOV images. A 336 nm filter was employed for photoemission. Specimen bias voltage was 10 kV (rather than the typical 20 kV) to avoid field emission. The thermionic emission intensity was fit to the Richardson-Dushman equation using a work function of 2.0 eV (solid curve). The photo emission intensity was fit to the Fowler-DuBridge model at a constant work function of 2.0 eV and photon energy of 3.7 eV (dashed curve).

Fig. A.4 presents PEEM and ThEEM images of two magnifications at two different temperatures, which were collected from the same spot on one diamond film sample. At these temperatures the PEEM image intensity without band pass filters is much greater than that in the ThEEM image, and therefore subtracting the thermal emission component from the photoemission image does not change the spatial intensity distribution of the latter significantly. The intensity scales on each image provide the evidence used to draw this conclusion. From these scales we can see that the highest

intensity in the PEEM image is a factor of 26 and 6 larger at 450 °C and 530 °C respectively. However, the spatial distribution of intensity in the images from both emission modes share significant similarities. For instance, the same bright lines are found to be the dominant features in both PEEM and ThEEM, which are likely the same structures observed by SEM and AFM. Thus we conclude that the surface morphology has a significant influence on the spatial distribution of both photoemission and thermionic emission intensity. Nevertheless, apart from this line contrast, the images for both emission processes show uniform intensity within an order of magnitude over the whole surface, as opposed to being limited to a few bright regions as seen in typical field emission images of nanostructured diamond films [10].

As mentioned above, prior spectroscopic studies of photo-induced and thermionic emission from these multi-layer diamond films indicated sources for the two emission processes that are clearly separated in depth. However, the obvious similarities of the spatial intensity distributions in the PEEM and ThEEM micrographs indicate that the emission yields for both processes are determined by the same surface physical properties, i.e. surface roughness, film microstructure and surface work function. While field emission from the samples is insignificant under the experimental settings in this work, the effect of different acceleration fields on the thermionic emission is not studied, which calls for future efforts. Also, the spatial distribution of the surface work function still needs to be examined through spectro-microscopic methods.

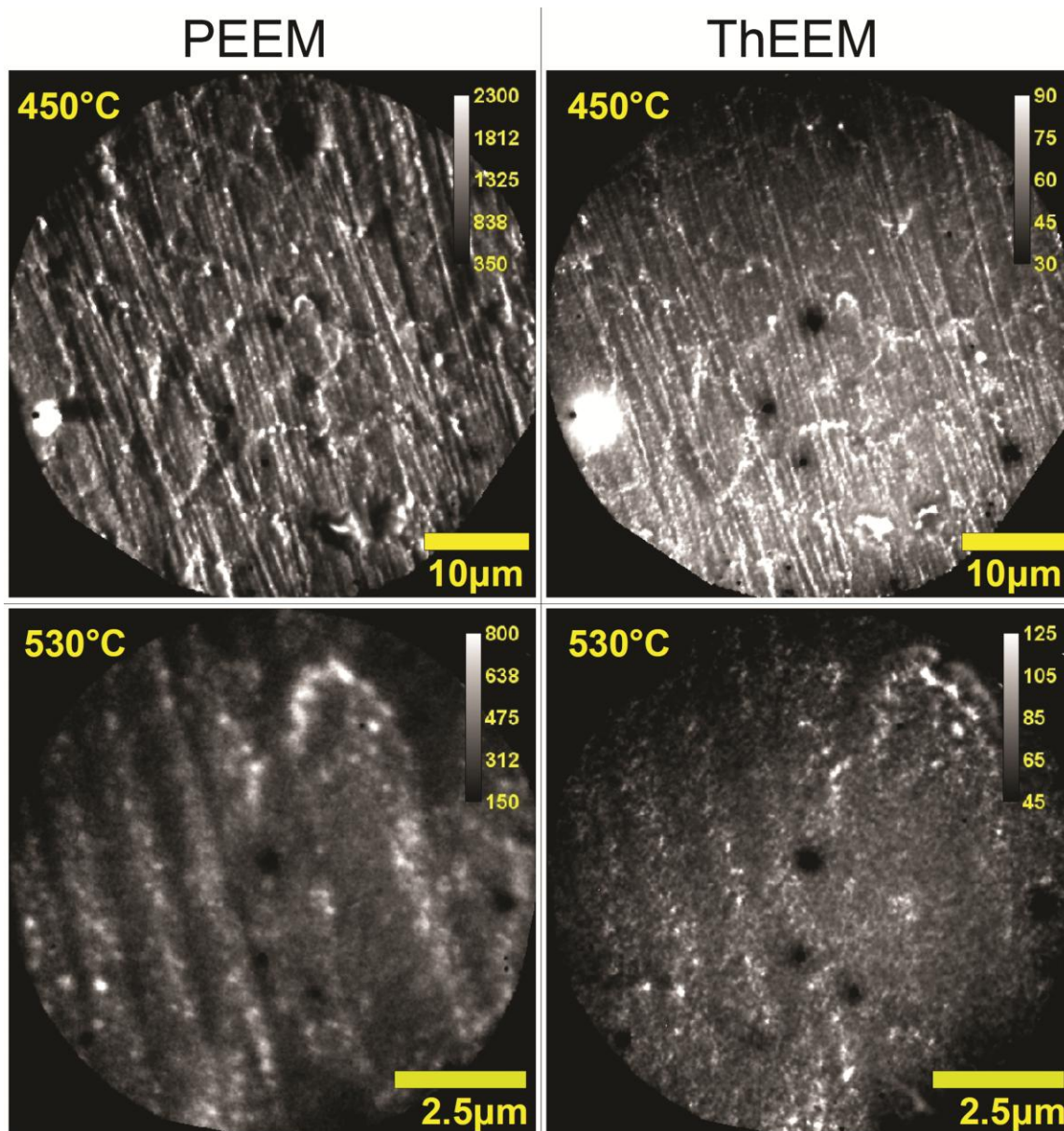


Fig. A.4 Comparison of PEEM and ThEEM images from the same regions. The white to dark intensity scale is shown in each image. The PEEM images were obtained with direct Xe lamp illumination without filters. Note that these PEEM images have significantly greater intensity than the ThEEM images at the same temperature. The same characteristic features such as bright lines and spots can be found in both PEEM and

ThEEM images. (The constant dark spots are damaged areas on the detector, which contribute little intensity to the average.)

A.5 Conclusions

The diamond films studied here display a temperature onset for measurable thermionic emission of about 250 °C and show a nearly exponential increase of emission intensity with temperature. Strong photoemission by excitation with visible light was also observed by both PEEM and photoelectron spectroscopy. Furthermore, relatively uniform electron emission from both photon and thermal excitation mechanisms is observed with electron emission microscopy. A comparison of PEEM and ThEEM images suggests that the same effective work function determines the photoemission and thermionic emission properties of these composite films. This work function was measured to be about 2 eV by electron spectroscopy. We conclude that the surface of the N-doped diamond layer determines the effective work function. Surface morphology and film microstructure is also evident in the PEEM and ThEEM images. In order to provide homogeneous emission over the whole surface, which would be desirable for applications in energy conversion devices, our results indicate that it is important to control not only the electronic properties but also the surface roughness and microstructure of the diamond films.

References

- [1] J.W. Schwede, I. Bargatin, D.C. Riley, B.E. Hardin, S.J. Rosenthal, Y. Sun, F. Schmitt, P. Pianetta, R.T. Howe, Z.X. Shen, N.A. Melosh, "Photon-Enhanced Thermionic Emission for Solar Concentrator Systems", *Nat. Mater.* 9 (2010): 762-767.

- [2] T.L. Westover, A.D. Franklin, B.A. Cola, T.S. Fisher, R.G. Reifenberger, "Photo- and Thermionic Emission from Potassium-Intercalated Carbon Nanotube Arrays", *J. Vac. Sci. Technol. B* 28 (2010) 423-434.
- [3] F.A.M. Koeck, R.J. Nemanich, "Emission Characterization from Nitrogen-Doped Diamond with Respect to Energy Conversion", *Diamond and Relat. Mater.* 15 (2006) 217-220.
- [4] J. Van der Weide, Z. Zhang, P.K. Baumann, M.G. Wensell, J. Bernholc, and R.J. Nemanich, "Negative-Electron-Affinity Effects on Diamond (100) Surface", *Phys. Rev. B* 60 (1994): 8.
- [5] F.A.M. Koeck, Robert J. Nemanich, "Low Temperature Onset for Thermionic Emitters Based on Nitrogen Incorporated UNCD Films", *Diam. Relat. Mater.* 18 (2009): 232-234.
- [6] M. Kataoka, C. Zhu, F.A.M. Koeck, R.J. Nemanich, "Thermionic Electron Emission from Nitrogen-Doped Homoepitaxial Diamond", *Diam. Relat. Mater.* 19 (2010): 110-113.
- [7] M. Suzuki, T. Ono, N. Sakuma, T. Sakai, "Low-Temperature Thermionic Emission from Nitrogen-Doped Nanocrystalline Diamond Films on N-Type Si Grown by MPCVD", *Diam. Relat. Mater.* 18 (2009) 1274-1277.
- [8] R.J. Nemanich, S.L. English, J.D. Hartman, A.T. Sowers, B.L. Ward, H. Ade, R.F. Davis, "Imaging Electron Emission from Diamond and III-V Nitride Surfaces with Photo-Electron Emission Microscopy", *Appl. Surf. Sci.* 146 (1999) 287-294.
- [9] F.A.M. Koeck, J.M. Garguilo, R.J. Nemanich, "Imaging Electron Emission from Diamond Film Surfaces: N-Doped Diamond vs. Nanostructured Diamond", *Diam. Relat. Mater.* 10 (2001): 1714-1718.
- [10] F.A.M. Koeck, J.M. Garguilo, B. Brown, R.J. Nemanich, "Enhanced Low-Temperature Thermionic Field Emission from Surface-Treated N-Doped Diamond Films", *Diam. Relat. Mater.* 11 (2002): 774-779.
- [11] F.A.M. Koeck, J.M. Garguilo, R.J. Nemanich, S. Gupta, B.R. Weiner, G. Morell, "Spatial Distribution of Electron Emission Sites for Sulfur Doped and Intrinsic Nanocrystalline Diamond Films", *Diam. Relat. Mater.* 12 (2003): 474-480.
- [12] J.M. Garguilo, F.A.M. Koeck, R.J. Nemanich, X.C. Xiao, J.A. Carlisle, O. Auciello, "Thermionic Field Emission from Nanocrystalline Diamond Coated Silicon Tip Arrays", *Phys. Rev. B* 72 (2005): 165404.
- [13] S. Kono, T. Saito, S.H. Kang, W.Y. Jung, B.Y. Kim, H. Kawata, T. Goto, Y. Kakefuda, H.W. Yeom, "Band Diagram for Chemical Vapor Deposition Diamond

Surface Conductive Layer: Presence of Downward Band Bending Due to Shallow Acceptors", *Surf. Sci.* 604 (2010): 1148-1165.

[14] J.B. Cui, J. Ristein, M. Stammler, K. Janischowsky, G. Kleber, L. Ley, "Hydrogen Termination and Electron Emission from CVD Diamond Surfaces: A Combined Secondary Electron Emission, Photoelectron Emission Microscopy, Photoelectron Yield, and Field Emission Study", *Diam. Relat. Mater.* 9 (2000): 1143-1147.

[15] D. Takeuchi, H. Kato, G.S. Ri, T. Yamada, P.R. Vinod, D. Hwang, C.E. Nebel, H. Okushi, S. Yamasaki, "Direct Observation of Negative Electron Affinity in Hydrogen-Terminated Diamond Surfaces", *Appl. Phys. Lett.* 86 (2005): 152103.

[16] L. Diederich, O.M. Kuettel, P. Aebi, L. Schlapbach, "Electron Affinity and Work Function of Differently Oriented and Doped Diamond Surfaces Determined by Photoelectron Spectroscopy", *Surf. Sci.* 418 (1998): 219-239.

[17] F.A.M. Koeck, R.J. Nemanich, A. Lazea, K. Haenen, "Thermionic Electron Emission from Low Work-Function Phosphorus Doped Diamond Films", *Diam. Relat. Mater.* 18 (2009): 789-791.

[18] E. Bauer, M. Mundschau, W. Swiech, W. Telieps, "Surface Studies by Low-Energy Electron Microscopy (LEEM) and Conventional UV Photoemission Electron Microscopy (PEEM)", *Ultramicroscopy* 31 (1989): 49-57.

[19] F.A.M. Koeck, J.M. Garguilo, R.J. Nemanich, "Direct Correlation of Surface Morphology with Electron Emission Sites for Intrinsic Nanocrystalline Diamond Films", *Diam. Relat. Mater.* 13 (2004): 1022-1025.

[20] I. Jeon, C. Park, D. Kim, N. M. Hwang, "Effect of Methane Concentration on Size of Charged Clusters in the Hot Filament Diamond CVD Process", *J. Cryst. Growth* 223 (2001): 6-14.

[21] T. Sun, F.A.M. Koeck, C. Zhu, R.J. Nemanich, "Combined Visible Light Photo-Emission and Low Temperature Thermionic Emission from Nitrogen Doped Diamond Films", *Appl. Phys. Lett.* 99 (2011): 202101.

APPENDIX B
COPYRIGHT STATEMENTS

This thesis includes two published journal articles: T. Sun, et. al., *Appl. Phys. Lett.* 99 (2011): 202101 as a part of Chapter 3, and N. Neugebohrn, et. al., *Diam. Relat. Mater.* 40 (2013): 12-16 as the appendix A. Additionally, the contents of Chapter 4 have been submitted to *Diam. Relat. Mater.* All co-authors have granted their permissions to include these contents.

The following figures: Fig. 1.3, 1.4 and 2.3 are cited from separate journal articles, the copyright permissions of which are attached here.

| | |
|--|---|
| License Number | 3273210451044 |
| License date | Nov 20, 2013 |
| Licensed content publisher | Nature Publishing Group |
| Licensed content publication | Nature Materials |
| Licensed content title | Photon-enhanced thermionic emission for solar concentrator systems |
| Licensed content author | Jared W. Schwede, Igor Bargatin, Daniel C. Riley, Brian E. Hardin, Samuel J. Rosenthal, Yun Sun |
| Licensed content date | Aug 1, 2010 |
| Type of Use | reuse in a dissertation / thesis |
| Volume number | 9 |
| Issue number | 9 |
| Requestor type | academic/educational |
| Format | print and electronic |
| Portion | figures/tables/illustrations |
| Number of figures/tables/illustrations | 1 |
| High-res required | no |
| Figures | Figure 1 |
| Author of this NPG article | no |
| Your reference number | |
| Title of your thesis / dissertation | Combined Photo- and Thermionic Electron Emission from Low Work Function Diamond Films |
| Expected completion date | Nov 2013 |
| Estimated size (number of pages) | 154 |
| Total | 0.00 USD |

| | |
|--|---|
| License Number | 3273210933495 |
| License date | Nov 20, 2013 |
| Licensed content publisher | Elsevier |
| Licensed content publication | Solar Energy Materials and Solar Cells |
| Licensed content title | High performance isothermal photo-thermionic solar converters |
| Licensed content author | Gideon Segev, Abraham Kribus, Yossi Rosenwaks |
| Licensed content date | June 2013 |
| Licensed content volume number | 113 |
| Number of pages | 10 |
| Type of Use | reuse in a thesis/dissertation |
| Portion | figures/tables/illustrations |
| Number of figures/tables/illustrations | 1 |
| Format | both print and electronic |
| Are you the author of this Elsevier article? | No |
| Will you be translating? | No |
| Title of your thesis/dissertation | Combined Photo- and Thermionic Electron Emission from Low Work Function Diamond Films |
| Expected completion date | Nov 2013 |
| Estimated size (number of pages) | 154 |
| Elsevier VAT number | GB 494 6272 12 |
| Permissions price | 0.00 USD |
| VAT/Local Sales Tax | 0.00 USD / 0.00 GBP |
| Total | 0.00 USD |

| | |
|--|--|
| License Number | 3273211081604 |
| License date | Nov 20, 2013 |
| Licensed content publisher | Elsevier |
| Licensed content publication | Nuclear Instruments and Methods in Physics Research Section A: Accelerators, Spectrometers, Detectors and Associated Equipment |
| Licensed content title | Photoelectron spectroscopy—An overview |
| Licensed content author | Stefan Hüfner, Stefan Schmidt, Friedrich Reinert |
| Licensed content date | 21 July 2005 |
| Licensed content volume number | 547 |
| Licensed content issue number | 1 |
| Number of pages | 16 |
| Type of Use | reuse in a thesis/dissertation |
| Portion | figures/tables/illustrations |
| Number of figures/tables/illustrations | 1 |
| Format | both print and electronic |
| Are you the author of this Elsevier article? | No |
| Will you be translating? | No |
| Title of your thesis/dissertation | Combined Photo- and Thermionic Electron Emission from Low Work Function Diamond Films |
| Expected completion date | Nov 2013 |
| Estimated size (number of pages) | 154 |
| Elsevier VAT number | GB 494 6272 12 |
| Permissions price | 0.00 USD |
| VAT/Local Sales Tax | 0.00 USD / 0.00 GBP |
| Total | 0.00 USD |